Title

Insights into Carbon Dioxide Capture: Exploring Redox-Active Molecules and N-Heterocyclic Carbenes

Author

Li, Clarabella

Publication Date

2024

Peer reviewed|Thesis/dissertation

UNIVERSITY OF CALIFORNIA,
IRVINE

Insights into Carbon Dioxide Capture: Exploring Redox-Active Molecules and *N*-Heterocyclic Carbenes

DISSERTATION

submitted in partial satisfaction of the requirements
for the degree of

DOCTOR OF PHILOSOPHY

in Chemistry

by

Clarabella J. Li

Dissertation Committee:
Professor Jenny Y. Yang, Chair
Professor Andy S. Borovik
Professor Joseph P. Patterson

2024

DEDICATION

To my family, fellow scientists.

TABLE OF CONTENTS

LIST OF FIGURES……. v

LIST OF SCHEMES…… ix

LIST OF TABLES……..……... x

ACKNOWLEDGMENTS……... xi

VITA……..……. xii

ABSTRACT OF DISSERTATION…..…… xvi

Chapter 0: Background and Motivation…….……..…….. 1
0.1: Introduction……...…….. 1
0.2: pH Swings…….…….. 2
0.3: Transition Metals……. 4
0.4: Direct Air Capture……...…… 6
0.5: Conclusions……. 8
0.6: References……... 9

Chapter 1: Aqueous Electrochemical and pH Studies of Redox-Active Guanidino Functionalized Aromatics for CO_2 Capture…….…….. 16
1.1: Introduction……. 17
1.2: Results and Discussion…….……... 18
1.2.1: Synthesis of GFAs……..…… 18
1.2.2: pK_a and Electrochemical Properties in Acetonitrile……..……..…. 20
1.2.3: Reactivity with CO_2…….……..…. 22
1.2.4: pK_a and Electrochemical Properties in Protic Solvents…..……..… 25
1.2.5: Controlled Potential Electrolysis and Supporting Experiments…….…..… 29
1.3: Conclusions...…….. 34
1.4: Experimental……... 35
1.5: Crystallographic Information……..…… 40
1.6: References……... 45

Chapter 2: Carbon Dioxide Capture *via* Ruthenium PNP Pincer Complex……... 49
2.1: Introduction……. 50
2.2: Results……..……... 51
2.2.1: Computational Studies…...…… 51
2.2.2: Experimental Evaluation of the Electrochemical Capture of CO_2 by Ru-PNP…… 52
2.3: Discussion……... 58
2.4: Conclusions...……..... 60
2.5: Experimental……... 61
2.6: References……... 63

Chapter 3: Heterocyclic Carbenes for CO_2 Capture: Experimental Data for *N*-Heterocyclic Carbenes in Support of a Computational Study……. 68

3.1: Introduction…….…… 69
3.2: Results and Discussion…….……... 71
3.2.1: Computational Examination of Carbenes in Water…… 71
3.2.2: Computational Examination of Carbenes in Non-Aqueous Solvents……. 74
3.2.3: Experimental Examination of NHCs in Non-Aqueous Solvents…… 76
3.3: Conclusions...…….. 86
3.4: Experimental……... 88
3.5: References……..... 97

LIST OF FIGURES

Figure 0.1: General representation of a pH-mediated eCCC cycle (EPS). 2

Figure 0.2: Redox carriers previously studied in pH swing systems. These include (A) the quinone – tiron (disodium 4,5-dihydroxy-1,3-benzenedisulfonate, (B) aminopyridium nitrate, and (C) a sulfonated phenazine derivative (DHPZ). 3

Figure 0.3: The different classes of transition metal complexes assayed by DuBois and co-workers. 5

Figure 0.4: Carbonate adduct, $[Cu_2(tpmc)(\mu\text{-}CO_3)]^{2+}$ formed from $[Cu_2(tpmc)(\mu\text{-}OH)]^{3+}$. 6

Figure 0.5: Addition of CO_2 to a carbene (NHC) to the zwitterionic imidazolium carboxylate. 7

Figure 1.1: ORTEP structure of 1,4 btmgb$H_2[PF_6]_2$. Thermal ellipsoids are shown at 80% probability. 19

Figure 1.2: ORTEP of monoprotonated 1,4-btmgbH$[PF_6]$. Thermal ellipsoids are shown at 80% probability. 20

Figure 1.3: 1,4-btmgb (1 mM) in MeCN with $TBAPF_6$ as the supporting electrolyte (100 mM) at varied scan rates. 20

Figure 1.4: Varied scan window of 1,4-btmgb$H_2[PF_6]_2$ (scan rate = 500 mV/s) in MeCN, with 100 mM $TBAPF_6$ as the supporting electrolyte and a glassy carbon counter electrode. 21

Figure 1.5: 1 mM 1,4-btmgbH$[PF_6]$ in MeCN with 100 $TMAPF_6$, varied scan rate. 21

Figure 1.6: X-ray crystal structure of 1,4-btmgb$H_2(HCO_3^-)_2$. Thermal ellipsoids are shown at 80% probability. 22

Figure 1.7: ORTEP of 1,4-btmgb$H_2(HCO_3^-)_2\cdot(H_2O)_2$, ellipsoids are shown at 80% probability 22

Figure 1.8: ^1H NMR of 1,4-btmgb in D_2O, 600 Hz, 293 K, under 1 atm N_2 (top) and under 1 atm of CO_2 (bottom). 23

Figure 1.9: $^{13}C\{^1H\}$ NMR of 1,4-btmgb in D_2O, 151 Hz, 293 K, under 1 atm N_2 (top) and under 1 atm CO_2 (bottom). 24

Figure 1.10: NMR spectra of 1,4-btmgb$H_2[PF_6]_2$ in D_2O ^1H NMR 600 Hz, 293 K (top), and $^{13}C\{^1H\}$ at 151 Hz, 293 K (bottom). 24

Figure 1.11: Cyclic voltammetry of 1,4-btmgb in 100 mM KCl in H_2O at various pH values. 25

Figure 1.12: Cyclic voltammetry of 1 mM 1,4-btmgb vs SCE in water with 100 mM KCl at varied alkaline conditions by the additions of concentrated NaOH, scan rate = 400 mV/s. 25

Figure 1.13: Cyclic voltammetry of 1 mM 1,4-btmgb in water with 100 mM KCl, scan rate of 100 mV/s. Varied solution pH with additions of 1 M HCl 26

Figure 1.14: Cyclic voltammetry of 1 mM 1,4-btmgb (protonated to 1,4-btmgbH_2^{2+} by solution pH) in water with 100 mM KCl, scan rate 400 mV/s. Varied solution pH with additions of 1 M HCl. 26

Figure 1.15: pH vs $E_{1/2}$ (V *vs* SCE) from points collected from titrating 1M acetic acid and 1M NaOH into 1,4-btmgb in aq. KCl (conc.) solution. 27

Figure 1.16: pH measurements *vs.* E_{pa} values from pH 13.79 to 2.52, taken from an initial solution of 1 mM btmgb dissolved in water with 100 mM KCl and titrated with 1 M NaOH and 1 M HCl or 1 M acetic acid. Collective data from varied scan rates of 200 mV, 400 mV, and 700 mV. 27

Figure 1.17: pH measurements *vs.* E_{pc} (from a pairing CV with DPV experiments) from pH 14.12 to 9.49, taken from an initial solution of 2 mM btmgb dissolved in water with 200 mM KCl and titrated with 0.1 M, 1 M, or conc. NaOH and 0.1 M or 1 M HCl. CV's were taken with a scan rate of 500 mV/s. 28

Figure 1.18: pH measurements *vs.* E_p, differential-pulse voltammetry (DPV) data from pH 14.12 to 9.49, taken from an initial solution of 2 mM btmgb dissolved in water with 200 mM KCl and titrated with 0.1 M, 1 M, or conc. NaOH and 0.1 M or 1 M HCl. 28

Figure 1.19: Cyclic voltammetry of 1 mM 1,4-btmgb in MeOH with 100 mM NaBr referenced *vs* Ag/Ag^+. 28

Figure 1.20: Cyclic voltammetry of 1mM 1,4-btmgb in EtOH with 100 mM $NaClO_4$ referenced *vs* Ag/Ag^+. 28

Figure 1.21: 2 mM 1,4-btmgb in 200 mM KCl and water, preoxidation scan rates 500 mV/s and postoxidation scan rate 250 mV/s. 29

Figure 1.22: ^1H NMR (500 Hz, 293 K) spectra of 1,4-btmgb$[BF_4]_2$ in CD_3CN before (A) and after (B & C) water addition, aromatic region. 30

Figure 1.23: ^1H NMR (500 Hz, 293 K) spectra of the oxidized species 1,4-btmgb$[BF_4]_2$ in CD_3CN before (A) and after (B & C) water addition, methyl region. The high amounts of water added to this solution result in the residual water peak that is typically at 2.13 ppm (in CD_3CN) with respect to the solvent residual peak to shift downfield to 3.22 ppm due to H-bonding. 31

Figure 1.24: Cyclic voltammetry investigating the reduction events at 0 and -0.18 V vs. SCE of 1,4-btmgbH^+ in water by scanning reductively first before scanning again after the main redox peak at 0.2 V vs SCE (1,4-btmgb/btmgb^{2+}). 1 mM 1,4-btmgb in water with 100 mM KCl at 250 mV/s, at pH 11.72. 32

Figure 1.25: EPR spectrum of 2 mM 1,4 btmgb oxidized for 10 mins, measured at 77K, microwave frequency = 9.43 GHz. 33

Figure 1.26: UV–visible SEC data of 0.1 mM 1,4-btmgb. Oxidation at 500 mV *vs* Ag^+/Ag electrode in unbuffered water with KCl (100 mM) was performed at pH 11.91. Under these conditions, it is expected to protonate once to give 1,4-btmgbH^+. Purple trace is initial 1,4-btmgbH^+ and pink trace is oxidized 1,4-btmgb^{2+} at 250 mV vs SCE. 33

Figure 1.27: UV-Vis spectra before and after controlled oxidative electrolysis of 1 mM 1,4 btmgbH^+ in water with 100 mM KCl. Oxidation held at 0.5 V vs. SCE. Sample diluted for UV-Vis measurements. 34

Figure 1.28 ^1H NMR of 1,4 btmgb$H_2[PF_6]_2$ in CD_3CN, 600 Hz, 293 K. 38

Figure 1.29 $^{13}C\{^1H\}$ NMR of 1,4 btmgb$H_2[PF_6]_2$ in CD_3CN, 600 Hz, 293 K. 38

Figure 1.30 ^1H (500 Hz) and $^{13}C\{^1H\}$ (151 Hz) NMR of 1,4 btmgbH$[BF_4]$ in CD_3CN, 293 K. 40

Figure 2.1: Energy level diagram of computed energies between the Ru(II) affinity to CO_2 compared to Ru(III). 51
Figure 2.2: The various substitution positions tested around complex 2. 52
Figure 2.3: The energy relationships of the pincer complex at various sites of substitution. 52
Figure 2.4: The energy relationships of different transition metal centers in the pincer complex. 52
Figure 2.5: CVs of deprotonated Ru-PNP (3/2) in THF with 0.1 M $TBAPF_6$ at varied scan rates. See Table 2.1 for respective i_a/i_c *vs* scan rates. 53
Figure 2.6: CVs of CO_2 bound Ru-PNP (3'/2') in THF with 0.1 M $TBAPF_6$ at varied scan rates. See Table 2.2 for respective i_a/i_c *vs* scan rates. 53
Figure 2.7: Ru-PNP 3 scanned at 1000 mV/s in concentrations of 1 mM in THF with 100 mM $TBAPF_6$, variable window. This illustrates how the anodic window effects the reduction peak. 54
Figure 2.8: Ru-PNP 2 and 3 both at 500 mV/s in conc. of 1 mM in THF with 100 mM $TBAPF_6$. Depending on the anodic window, they lose the return reduction peak. Yellow star is of 2/2' and green star is of 3/3' – additional peaks past 500 mV have been assigned as ligand peaks. 54
Figure 2.9: CVs of CO_2 bound Ru-PNP (3/3') before and after controlled oxidation. 55
Figure 2.10: Ru-PNP 3 scanned without heating and after heating up to 60 C. 500 mV/s in THF with 100 mM $TBAPF_6$. 55
Figure 2.11: SEC UV-Vis experiment of deprotonated Ru^{II} being oxidized to Ru^{III}. 55
Figure 2.12: UV-Vis spectra of compounds 2 and 2' before and after controlled oxidation. 56
Figure 2.13: FT-IR absorbance spectra of 2 and 2'. 56
Figure 2.14: FT-IR absorptions in the carboxylate region before and after oxidative electrolysis of 2'. 57
Figure 2.15: FT-IR absorptions in the carbonyl region before and after oxidative electrolysis of 2'. Observed loss of CO ligand. 57
Figure 3.1: Library of carbenes and R-groups computationally tested. 70
Figure 3.2: Addition of CO_2 to a carbene (NHC) to give a carboxylate. 72
Figure 3.3: Primary σ-bonding orbital involved in CO_2 binding to a carbene. 72
Figure 3.4: Potential energy scan (PES) of NHC 1W, showing the preferred CO_2 binding of 0°. 72
Figure 3.5: Graph of pK_a vs. CO_2 binding energy for all molecules tested in water. 73
Figure 3.6: QTAIM displaying the hydrogen bonding interactions of molecules; (A) 1O, (B) 1D2, (C) 6D2. 73
Figure 3.7: R-groups for 5-DACs (Type 6) found to have a pK_a lower than that of water, whilst maintaining CO_2 binding affinity. 74
Figure 3.8: A: Graph of pK_a vs. CO_2 binding energy for all carbenes tested in MeCN; B: Graph of pK_a vs. CO_2 binding energy for all carbenes tested in DMSO 75

Figure 3.9: ^{1}H NMR spectra showing the progression of carboxylate formation after additions of CO_2 titrated into a NMR tube containing a 10 mM solution of 1C in DMSO-d_6. 77
Figure 3.10: ^{1}H NMR spectra in DMSO-d_6 of 10 mM 1C, taken at 5-minute intervals after sparging 0.1 % CO_2 in N_2 into the solution Complete conversion was observed after 20 minutes. 78
Figure 3.11: ^{1}H NMR spectra in DMSO-d_6 of 10 mM 1C with increasing percentages of CO_2 after 5 minutes from addition. Arrows highlight the beginning of carboxylate formation. 78
Figure 3.12: 1 mM of 1C sparged with N_2, 0.15% CO_2 then N_2 again demonstrating irreversible binding of CO_2 in the observed increase absorbance of features between 230-280 nm. 79
Figure 3.13: 1 mM solution of 1C in the 250-280 nm region demonstrating that binding occurs at CO_2 concentrations as low as 0.01%. 79
Figure 3.14: Sites of NMR data collection, the carboxylate carbon (red) and the imidazolium backbone protons (pink). 80
Figure 3.15: ^{13}C NMR chemical shift of the carboxylate carbon vs. CO_2 binding energies. A: DMSO; B: MeCN. 81
Figure 3.16: ^{1}H NMR chemical shift values of the imidazolium backbone protons vs. CO_2 binding energies. A: DMSO; B: MeCN. 81
Figure 3.17: ^{1}H NMR spectra for 1Q in DMSO-d_6; the synthesized pre-1Q (top) and the product post basic carboxylation (bottom). 85
Figure 3.18: ORTEP structure of 2,4,6,8-tetrakis(pentafluorophenyl)-2,4,6,8-tetraazabicyclo-[3.3.0]octane, isolated *in lieu* of Type 1E. 86
Figure 3.19: ^{1}H NMR of 2,4,6,8-tetrakis(pentafluorophenyl)-2,4,6,8-tetraazabicyclo-[3.3.0]octane in DMSO-d_6, 600 MHz, 293 K. 96

LIST OF SCHEMES

Scheme 1.1: Two Modes of CO_2 Capture by a Redox-Active Molecule (R) via Direct Capture or pH Swing Methods. 17

Scheme 1.2: Two Modes of CO_2 Capture by Guanidines. 18

Scheme 1.3: Synthesis of 1,4-btmgb, 1,4-btmgb^{2+}, and 1,4-btmgbH_2^{2+}. 19

Scheme 1.4: Alkaline hydrolysis of a TMG group on oxidized 1,4 btmgb. 30

Scheme 1.5: Various Proposed Comproportionation Pathways for [1,4-btmgb]$^{2+}$ (A) Unprotonated and (B) between a Reduced Monoprotonated Species [1,4-btmgbH]$^{+}$. 32

Scheme 2.1: The proposed eCCC cycle for Ru(II)-PNP complex 2, after deprotonation from 1. 50

Scheme 3.1: Naming convention used and general synthesis between the imidazolium (pre-Type 1), NHC (Type 1), and imidazolium carboxylate (Type 1-CO_2). See section 3.4 Experimental for details. 75

LIST OF TABLES

Table 1.1: pH Values Observed before and after Electrolysis of 2 mM Solutions of 1,4-btmgb and 1,4-btmgbH_2^{2+a}. 29

Table 1.2: Compiled Crystallographic Data. 44

Table 2.1: i_a/i_c vs Scan rates for 3/2. 53

Table 2.2: i_a/i_c vs Scan rates for 3'/2'. 53

Table 3.1: Table of hydrogen bond strengths between CO_2 and R-groups in (a) 1D2 and (b) 1O. 75

Table 3.2: Summary of Data for Type 1 compounds experimentally studied. 82

ACKNOWLEDGEMENTS

The American Chemical Society for permission to include copyrighted materials, specifically in Chapter 0, published in *Chemical Reviews*, and Chapters 0 and 1, published in *ACS Organic & Inorganic Au*.
I am grateful for funding support from the Alfred P. Sloan Foundation and Research Corporation Scialog for Negative Emissions.

Thank you, Jenny, for the opportunity to learn and grow these last five years in the supportive lab space and team you have built over the last decade. I am grateful to have been a part of it all. The time spent in your lab will have a lasting impact on my life.

To my candidacy and thesis committee, Professors Borovik, Green, Heyduk, and Patterson, I appreciate the time, support, and advice you have given me.

To our collaborators with Sloan, colleagues working with Prof. Brushett at MIT and Prof. Alexandrova at UCLA, collaborators of Scialog, colleagues with Prof. Green at ASU, and Prof. Hornbostel at Univ. Pittsburg – I am grateful for our discussions and joint scientific efforts.

I have been inspired and motivated by all the Yang lab members I have met, past and present, no matter how brief our meeting, a greeting you in the vague order of encountering-
Post doctorates- Nadia, Ryan, Kelsey, Ana, Ab, and Magy. Graduate students- Zach, Bianca, Jeffrey, Tyler K., Alissa, Ian, Allie, Amanda K., Rakia, Andrew, Jared, Colleen, Ute, Faith, Ciara, Claire and Feven. And to the undergraduates I had the privilege of working with- Zaira, Jesus, Jaclyn, Brandon, Natalia, and Chris (Wenxuan); I really hope you guys go far.
A specific appreciation to Elise for making my graduate experience special, to say the least. Incredibly grateful to Sarah, who was a mentor and a general pillar of sanity through it all. And Teddy, thanks for coming along with the board games and words of support.

To my cohort at UC Irvine- Verto, Amanda A. (and honorable shout out to Michael), Khawla, Natalie, and Matt; I am grateful for the hangouts and the lots and lots of coffee.

Thank you to Melanie for giving me the invaluable opportunity to work in the chemistry stockroom. Working with you has been not only a developmental work experience but also a life experience. I am grateful for all the insight you have shared about the department and beyond.

Prof. Mark Kurth and Dr. Jackson Zhu, you both have helped me develop an appreciation for research. I am indebted to the first eye-opening opportunity to explore synthetic organic chemistry with you. I would have never gotten here without my experience with you.

My band of UC Davis buddies- Anna, Joyce, Kevin, Maria, Tyler L., Joy, and Max; I appreciate all the calls, candies, and adventures we had the chance to share.

To my family, who has had the misfortune of watching my development as a wondering and wandering mind since forever, thank you for encouraging and supporting my core curious perspective toward the world.

And all my love to Midna, my supportive little rock throughout this journey.

VITA

Clarabella J. Li

EDUCATION

University of California, Irvine ***2019-2024***
Ph.D. Candidate in Chemistry, Inorganic
University of California, Davis – Honors ***2013-2017***
B.Sc. in Chemistry with a Forensic Emphasis, Minor in Psychology

RESEARCH EXPERIENCE

Department of Chemistry, UC Irvine | Advisor: Prof. Jenny Y. Yang

Graduate Research Assistant ***January 2020 – July 2024***

Use of electrochemical techniques to explore redox-active chemical systems for carbon dioxide capture, which include:

- The synthesis of redox-active guanidine compounds. Probing the redox reactivity with cyclic voltammetry and controlled potential electrolysis. Using characterization techniques from NMR, LCMS, UV-Vis spectrometry, X-ray diffraction, GC and EPR.
- Collaboration with Prof. Matthew Green's lab at Arizona State Univ. and Prof. Katherine M. Hornbostel at the Univ. of Pittsburg towards the development of a desalination and decarbonization electrochemical cell membrane with the synthesis of phenazine-2,3-diol (DHPZ) and the incorporation of DHPZ onto commercial membranes (BW30 and DeltaMem).
- Synthesis and electrochemical reactivity studies on a Ru-PNP catalyst for carbon dioxide capture, working in computation collaboration with Prof. Anastassia Alexandrova at UCLA.
- The synthesis and characterization of *N*-heterocyclic-carbene carboxylates in experimental support to computational trends of CO_2 binding by carbenes observed by Alexandrova's group. Results observed support work being done in the 4C EFRC, Center for Closing the Carbon Cycle.

Mentored and supervised undergraduate students (two UCI students and two summer REU students)

Summer Research Assistant ***July 2019 – September 2019***

In collaboration with Prof. Vy M. Dong's research group at UCI, synthesized and investigated the reactivity of hydridic Ni and Pt catalysts for the selective reduction of esters.

Department of Chemistry, UC Davis | Advisor: Prof. Mark J. Kurth

Staff Research Associate II ***March 2018 – June 2019***

Synthesized CFTR potentiators (azaindoles), bithiazoles, and quinazolines in collaboration with Prof. Alan S. Verkman group at UCSF. Responsible for mentoring 2-3 undergraduate researchers.

Undergraduate Research Assistant ***October 2016 – March 2018***

Development of synthetic methodology with an emphasis on nitrogen-containing heterocycles: indazoles and indazolone derivatives. Operation of analytical instruments such as LCMS and NMR.

TEACHING & LEADERSHIP EXPERIENCE

Department of Chemistry, UC Irvine

Scientific Laboratory Management Fellowship ***Fall 2023 – Spring 2024***

Mentoring and managing a team of a dozen undergraduates in the upkeep and maintenance of the chemistry department teaching laboratory stockroom. Duties include, but are not limited to, updating and organizing inventory and beta testing lab procedures for the lab classes – all while upholding standard lab safety. Support teaching assistants with prepping teaching lab courses throughout the quarter – General Chemistry (*1LC-1LD*) and Inorganic Chemistry (*107L*). In addition to supporting the teaching labs, aided in hosting the OC Regional Science Olympiad at UCI. Participating in developing material for the UCI Chemistry Academy, a summer camp for grades 3-12.

Graduate Student Teaching Assistant ***Fall 2019 – Summer 2024***

Led classroom discussions of topics in general chemistry and organic chemistry. Provided office hours to answer questions pertaining to the course material. Prepared discussion worksheets and exam material in collaboration with other teaching assistants and the lecturing professor. Advised and provided feedback to students in the preparation of their senior thesis (Chem 180W/H181W).

Courses: Organic Chemistry (*Chem 51A – Fall 2019, Chem 51B – Winter 2020*), Senior Thesis Writing (*Chem H181W – Spring 2020, Chem 180W – Spring 2021*), General Chemistry (*Chem 1C – Spring 2022, Chem 1B – Winter 2023, Chem 1LD (lab) – Summer Session II 2023, Summer Session I 2024*)

Student Academic Success Center, Dutton Hall, UC Davis

Tutor ***October 2015 – June 2017***

Mentored first and second-year undergraduates in general chemistry, organic chemistry, and math.

Math Reader ***September 2016 – June 2017***

Graded and provided feedback on student performance for both students and the instructor.

Davis Senior High School, Davis CA

Teaching Assistant ***September 2016 – December 2016***

Led activities in high school chemistry classes. Shadowed high school chemistry teachers to observe classroom management. Assisted with homework grading and activity preparation.

Associated Students of the University of California Davis – The Pantry, UC Davis

Director of Internal Affairs ***September 2016 – August 2017***

The Pantry serves financially disadvantaged students at UC Davis by providing non-perishable foods, toiletries and resources. Fundraised $10,000 to support Pantry operations. Hired and managed roughly 200 volunteers quarterly to staff the Pantry. Coordinated events and maintained data for inventory.

Design Intern, Volunteer ***November 2014 – June 2016***

Worked on-site to provide service to students. In charge of the publicity and branding of the Pantry. Part of a team effort in the creative preparation and execution of promotional events for the Pantry.

PUBLICATIONS:

- **Li, C. J.**; Ziller, J. W.; Barlow, J. M.; Yang, J. Y.; "Aqueous Electrochemical and pH Studies of Redox-Active Guanidino Functionalized Aromatics for CO_2 Capture." *ACS Organic & Inorganic Au* **2024**, *4* (4) 387-394. – ***Virtual special edition "Electrochemical Explorations in Organic and Inorganic Chemistry"***
- Jones, R. J. R.; Lai Y.; Kan, K.; Guevarra, D.; Haber, J. A.; Ramirez, N. M.; Zito, A. M.; **Li, C. J.**; Yang, J. Y.; Appel, A. M.; Gregoire, J. M. "Accelerated screening of carbon dioxide capture by liquid sorbents." *RCS Digital Discovery* **2024.**
- Zito, A. M.; Clarke, L.; Barlow, J. M.; Bim, D.; Zhang, Z. Z.; Ripley, K.; **Li, C. J.**; Kummeth, A. L.; Leonard, M.; Alexandrova, A.; Brushett, F.; Yang, J. Y. "Electrochemical Carbon Dioxide Capture and Concentration." *Chemical Reviews* **2023**, *123* (13) 8069-8098.
- Kraemer, N.; **Li, C. J.**; Zhu J. S.; Larach, J. M.; Tsui, K. Y.; Tantillo D. J.; Haddadin, M. J.; Kurth, M. J. "Davis–Beirut Reaction: A Photochemical Bronsted Acid Catalyzed Route to *N*-Aryl 2*H*-Indazoles." *Organic Letters* **2019**, *21* (15), 6058-6062.
- Zhu, J. S.; **Li, C. J.**; Tsui, K. Y.; Kraemer, N.; Son, J.-H.; Haddadin, M. J.; Tantillo, D. J.; Kurth, M. J. "Accessing Multiple Classes of 2*H*-Indazoles: Mechanistic Implications for the Cadogan and Davis–Beirut Reactions" *Journal of the American Chemical Society* **2019**, *141* (15), 6247-6253.
- Zhu, J. S.; Kraemer, N.; **Li, C. J.**; Son, J.-H.; Haddadin, M. J.; Kurth, M. J. "Photochemical Preparation of 1,2-Dihydro-3*H*-indazol-3-one in Aqueous Solvent at Room Temperature." *Journal of Organic Chemistry* **2018**, *83* (24), 15493-15498.
- Zhu, J. S.; Kraemer, N.; Shatskikh, M. E.; **Li, C. J.**; Son, J.-H.; Haddadin, M. J.; Tantillo, D. J.; Kurth, M. J. "N–N Bond Formation between Primary Amines and Nitrosos: Direct Synthesis of 2-Substituted Indazolones with Mechanistic Insights." *Organic Letters* **2018**, *20* (16), 4736–4739. – ***Highlighted in Synfacts***
- Phuan, P.-W.; Son, J.-H.; Tan, J.-A.; **Li, C.**; Musante, I.; Zlock, L.; Nielson, D. W.; Finkbeiner, W. E.; Kurth, M. J.; Galietta, L. J.; Haggie, P. M.; Verkman, A. S. "Combination potentiator ('co-potentiator') therapy for CF caused by CFTR mutants, including N1303K, that are poorly responsive to single potentiators." *Journal of Cystic Fibrosis* **2018**, *17* (5), 595–606.

PATENT:

Hornbostel, K. M.; Lieber, A. R.; **Li. C.**; Yang, J.; Behbahani, H.; Green, M.; Membrane contactor for simultaneous desalination and CO_2 removal from seawater. U.S. Patent application, No. PCT/US2024/020399, March 18, **2024.**

ORAL & POSTER PRESENTATIONS:

- Southern California Inorganic Photochemistry (SCIP) ***April 2024***
  Oral: An electrochemical inspection of Ru-PNP for CO_2 capture and release
  Shared developments on the electrochemical release of CO_2 from Milstein's Ru-PNP catalyst.
- Southern California Organometallics ***June 2023***
  Poster: Investigating Redox-Active Guanidines for CO_2 Capture
- National American Chemical Society Meeting; 65th Anniversary of D.I.C ***March 2022***
  Poster: Investigating Redox-Active Guanidines for CO_2 Capture
  Presented the use of redox-active bases for electrochemically mediated capture of CO_2.
- Environmental Toxicology Department, UC Davis Picnic Day ***April 2017***
  Poster: Ban of Dungeness Crab Fishing Due to Domoic Acid
  Detailed the manifestation of the ban and history of the toxicology of domoic acid in the environment.
- 17th Annual R. Bryan Miller Symposium, UC Davis ***March 2017***
  Poster: Synthesis of Potentiators for CFTR (W1282X Mutation)
  Discussed details on the synthesis of 7-azaindole derivatives and activity trends on CFTR cells *in vitro*.

OUTREACH & AFFILIATIONS:

- **Competitive Edge Peer Mentorship Program** – Participated in a Mentoring Excellence Program (MEP), earned a certificate of mentorship and worked with an incoming graduate student participating in summer research, (*2023-2024*)
- **ReachOut TeachOut** (ROTO@UCI) – Participated in activities with high school students from neighboring school districts in campus laboratory tour visits and one-on-one mentorship, (*2023*)
- **ChemUNITY Peer Mentorship Program** – Supported an incoming graduate student with the process of adjusting to the graduate program, (*2022-2023*)
- **Association for Women in Science** (AWIS), Application Assistance Program – Aided in the graduate school application preparation for undergraduate students, (*2022*)
- **Chemistry Anti-Racist Coalition** (ChemARC) – Presentation: Becoming anti-Racist in The Physical Sciences, Younis, A.; Romero, M.; Flores Zuleta, H.; Campos Ayala, J.; Mustafa, K.; **Li. C.**, (*2020*)
- **UC Davis Chemistry Club** – Designed pamphlets and volunteered for hands-on demos during Picnic Day (*2015*). Participation in the Picnic Day Magic Show Event (*2016*)
- **WiSTEM** (UC Davis), **QTSTEM** (UC Irvine), **ACS** (Since *2019*)
- **The Bicycle Tree** – Aiding the local biking community with repairs and outreach, Volunteer, (*2023*)

HONORS, AWARDS, & SCHOLARSHIPS:

- Dissertation Fellowship, UC Irvine – *Spring 2024 (rewarded but returned due to accepting funding from the Scientific Laboratory Management Fellowship)*
- Minority Serving Institution Enhancement (MSIE), UC Irvine – *2019*
- Departmental Citation for Outstanding Graduating Seniors, UC Davis, Chemistry – *2017*
- Departmental Research Highest Honors, UC Davis, Chemistry – *2017*
- Dean's Honors List – Fall *2013*, Winter *2014*, Spring *2014*

ABSTRACT OF THE DISSERTATION

Insights into Carbon Dioxide Capture: Exploring Redox-Active Molecules and *N*-Heterocyclic Carbenes

by

Clarabella J. Li

Doctor of Philosophy in Chemistry

University of California, Irvine, 2024

Professor Jenny Y. Yang, Chair

With the increasing levels of anthropogenic carbon dioxide emissions, the need for climate change mitigation has never been more urgent. Existing methods for CO_2 removal are facilitated by thermally driven systems and thus suffer from being energy-intensive and inefficient. Joint efforts between computational and experimental chemistry fields can help steer research toward uncovering valuable insight into CO_2 reactivity with the ideal sorbent. This dissertation presents an investigation into various chemical systems studied, from which understanding the design principles and the limitations of the carbon capture systems came to be illuminated.

Chapter 1 details the study of 1,4-bis(tetramethylgaunidino)benzene (1,4-btmgb) as a redox-active sorbent and pH swing mediator. Spectroscopic and crystallographic studies demonstrate that 1,4-btmgb reacts with CO_2 in water to form the ion-paired bicarbonate adduct, [1,4-btmgbH_2](HCO_3^-)$_2$. The synthesis and characterization of the mono- and diprotonated forms

were performed, and their pK_a values were determined using differential pulse voltammetry (DPV) experiments. From electrochemical pH swing experiments, a degradation pathway was identified and proposed based on the observation of a radical species.

Chapter 2 describes experimental and computational work expanding on the promising CO_2 reactivity of a Ru-PNP pincer complex. Deprotonated Ru[(PNP)(Cl)(CO)(H)] was previously found to bind to CO_2 *via* metal-ligand cooperation. Computational values confirmed by experimental results demonstrate the redox behavior for Ru-PNP in the CO_2 bound and unbound forms. However, cycling CO_2 with this chemical system proved difficult due to the observed decomposition of the complex after attempts to oxidize to release CO_2.

Chapter 3 considers carbenes as a sorbent for the direct air capture of CO_2. A computational survey of a diverse library of carbenes presents a linear relationship between the calculated pK_a of the carbene and CO_2 binding energy in water and organic solvents. Experimental evaluation of a selection of *N*-heterocyclic carbenes demonstrated an affinity to bind CO_2 at low concentrations of 1% and below from gas streams. A trend between ^{13}C NMR spectroscopic signals of the varied substituted imidazolium carboxylate compounds and corresponding CO_2 binding energy finds that the less bulky electron-donating substituents correlate with a more negative (stronger) binding energy to CO_2.

Chapter 0: Background and Motivation

Portions of this introduction were adapted from *ACS Org. & Inorg. Au* **2024**, *4* (4) 387-394 (section 0.1) and *Chemical Reviews* **2023**, *123* (13) 8069-8098 (sections 0.2–0.4).

0.1: Introduction

The increasing levels of carbon dioxide (CO_2) in the atmosphere has offset the natural balance of the Earth's climate, contributing to a looming catastrophe. The atmospheric levels of CO_2 has almost doubled to approximately 400 ppm from preindustrial levels of 218 ppm.[1] Each year, about 40 gigatons of carbon dioxide (CO_2) is emitted from human activity, with roughly 30% of these emissions arising from fossil fuel power plants.[2,3] Flue gas from fossil fuel power plants typically contains 8−10% of CO_2.

Research to aid in the decarbonization of the atmosphere includes the development of methods for CO_2 capture from industrial flue gas streams (point source capture) and direct air capture (DAC). The captured CO_2 can then be stored, commonly referred to as carbon capture and storage (CCS), or chemically converted into an carbon containing commodities or fuels.[4] The current state-of-the-art method for capturing CO_2 from flue gas uses an aqueous alkanolamine solution to capture CO_2 at ambient temperature and pressure. The release of CO_2 is achieved by heating the sorbent (383 K for monoethanolamine).[5,6] However, these thermal-swing methods are constrained by the Carnot limit and can only achieve 5−40% of the maximum theoretical energy efficiency.[2,7]

Electrochemical methods are not constrained by the Carnot limit, allowing for theoretical efficiencies closer to the maximum thermodynamic limit.[8] A growing number of electrochemical CO_2 capture and concentration (eCCC) methods have been explored over the last several decades.[9]

A few avenues studying eCCC have been with redox-active small molecules such as quinones, pH swing systems, and transition metal complexes – the latter two of which will be discussed in this thesis.

0.2: pH Swing Systems

An electrochemical pH swing (EPS) adjusts the pH of an aqueous solution to capture CO_2 from dilute streams at a higher pH and release more concentrated CO_2 at a lower pH. As presented in **Figure 0.1**, a potential (E_{app1}) is applied to oxidize a basic solution with dissolved inorganic carbon, promoting a drop in pK_a of a redox-active species. This controlled acidification of the solution facilitates the release of CO_2. Regeneration of the basic solution is obtained with a reducing potential applied (E_{app2}). In contrast to direct CO_2 binding methods, which often compete with protonation due to the basic nature of the redox sorbent, EPS techniques utilize the different CO_2 species present at varying pH levels to capture and release CO_2 indirectly (**Equation 0.1**). A more basic solution promotes the solubility of CO_2 as bicarbonate (HCO^{3-}) or carbonate (CO_3^{2-}), while in acidic solutions, CO_2 will exist as carbonic acid with a much lower solubility in the solution.[10]

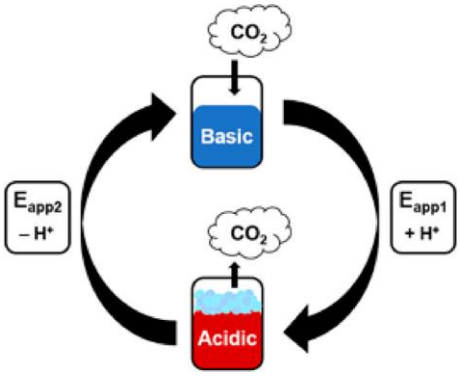

Figure 0.1: General representation of a pH-mediated eCCC cycle (EPS).[6]

Eq 0.1:
$$CO_{2(g)} + H_2O \overset{K_H}{\rightleftharpoons} H_2CO_3 \overset{K_1}{\rightleftharpoons} HCO_3^- + H^+ \overset{K_2}{\rightleftharpoons} CO_3^{2-} + 2H^+$$

Creating a dynamic pH gradient to capture and release CO_2 ultimately needs the construction of a flow system to cycle CO_2 successfully. In its simplest form, an EPS system is a controlled electrodialysis of water in a cell divided with membranes such as a bipolar or anion

exchange membrane.[10,11] The membranes prevent the unwanted mixing of different pH solution streams, and the construction of the cell specifically allows the flow and concentration of CO_2 through the system to be dissolved and released. This method has been popularly explored using seawater as a feedwater source with the idea of capturing CO_2 from the ocean. The saltwater (NaCl) serves as a natural electrolyte solution and helps form and separate sodium hydroxide and hydrochloric acid after the water molecules are split from the electrodialysis.[11,12]

Using a redox carrier to facilitate a pH swing can boost CO_2 capture efficiency and cycling, making identifying an ideal redox carrier for such a job a valuable research goal.[10] EPS systems with a redox carrier have the advantage of running at a lower voltage and using less energy than electrodialysis methods by being self-sufficient in proton generation for the acidification process. The redox carrier would perform a proton-coupled electron transfer (PCET) to induce a pH swing in an aqueous solution.[13–15]

A limited number of redox carriers described in the literature have been found to perform as aqueous pH mediators. While quinones have known PCET behavior, their limited solubility in aqueous solutions hinders their ability to participate as an efficient pH swing mediator (**Figure 0.2, A**).[16,17] Another compound with limited performance in an EPS system is a redox-active amine. Aminopyridium nitrate was found to reversibly produce 1-aminopyridinyl radical in a one-electron reduction in aqueous solutions. However, the efficiency of this compound was

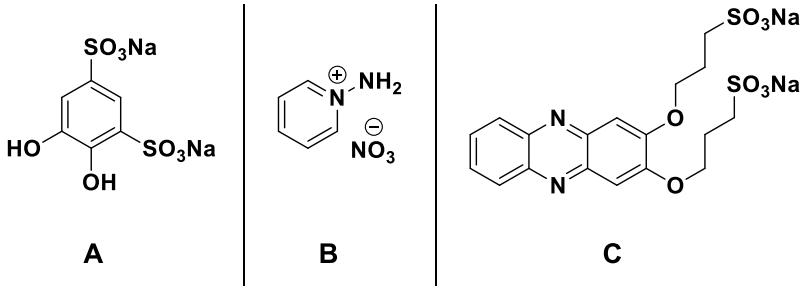

Figure 0.2: Redox carriers previously studied in pH swing systems. These include (**A**) the quinone – tiron (disodium 4,5-dihydroxy-1,3-benzenedisulfonate[16], (**B**) aminopyridium nitrate[18], and (**C**) a sulfonated phenazine derivative (DHPZ)[14].

limited due to self-reactivity via a radical-based pathway (**Figure 0.2, B**).[18] Finally, phenazines are a class of compounds found to show a greater promise in participating in redox-mediated pH swings.[13,14,19] One case is described by Aziz and co-workers, using a sulfonated phenazine derivative (DSPZ), produced a pH swing between 6 and 10, which captured CO_2 from gas streams of 10% CO_2, concentrating up to 100% CO_2 upon acidic release (**Figure 0.2, C**).[14]

With such methods, a few requirements must be met for the redox carrier to become an ideal pH swing mediator. Firstly, the redox carrier must have high solubility in an aqueous solution at a solubility greater than CO_2 (>1 M). Secondly, the complex must be sufficiently basic in its reduced form to allow a pH swing greater than pH 9, where dissolved CO_2 converts to bicarbonate or carbonate. The compound in its oxidized form must then be acidic enough to make a solution pH 6 or less to allow for outgassing.[14,20] Crucially, the pH swing mediator must be stable under oxygen and water in oxidized and reduced forms. The redox carrier must also maintain long-term stability to facilitate repeated cycling, though stability concerns can be mitigated by designing a reaction cell that sufficiently separates the two reactive species under different pH conditions.[10] For example, a continuous redox flow battery design has been popularly successful with the phenazine systems. Understanding how and why redox carriers for pH swing decompose would aid the design of new EPS systems.

0.3: Transition Metals

Redox-active transition metal (TM) centers paired with specific ligands can also serve as CO_2 capture agents in direct eCCC systems. DuBois and co-workers suggested that TM complexes with ligands that contain a CO_2 binding site (*i.e.*, a nucleophilic nitrogen or oxygen-based functional group) could enable CO_2 cycling.[8] The metal center as the active redox site would alter the electron density of the compound and thus the CO_2 binding affinity. Their study found that the

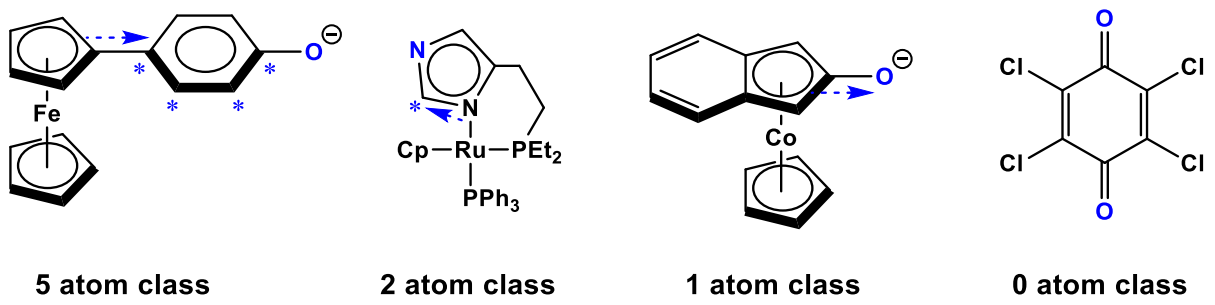

Figure 0.3: The different classes of transition metal complexes assayed by DuBois and co-workers.[7]

distance between the redox metal center to the CO_2 binding site significantly impacts the compound's ability to capture and release CO_2. The assayed compounds contained one, two, or five atoms separating the binding site to the redox active metal center of Co, Fe, or Ru and were also compared to a non-transition metal complex described as a zero-atom class (**Figure 0.3**). When the distance between the CO_2 binding site on the ligand and the metal was two bonds or greater, the oxidation state of the metal did not impact the release of the CO_2 from the ligand. CO_2 capture activity was only observed in the Co^{3+} cyclopentadienyl indenyl complex with a one-atom separation of the metal from the binding site. When CO_2 binds at a one-atom distance between the oxygen binding site on cyclopentadienyl indenyl from the transition metal Co(III), the reduction potentials shift anodically in cyclic voltammetry (CV) scans, indicating the electrochemical binding of CO_2. However, cycling CO_2 electrochemically *via* controlled potential electrolysis demonstrated that the Co(III) complex reduces CO_2 instead of being bound and released.

A few binuclear TM complexes explored in other works trap CO_2 dissolved in aqueous media as a bound carbonate ion.[21–24] In these complexes, bridging ligands orient two metals (Zn, Co, Ni, or Cu) to promote strong carbonate binding interactions. However, studies examining the electrochemical behavior of these compounds and their application to reversibly cycling CO_2 are limited.

DuBois and co-workers examined binuclear Ni and Cu complexes with varied bridging ligands for the reversible capture and release of bicarbonate and found that more flexible ligands resulted in enhanced binding.[24,25] Contrary to typical increased CO_2 binding affinity upon reduction, these systems bind carbonate upon *oxidation* of the TM^+ metal center to TM^{2+}, and *reduction* results in CO_2 release.

However, the reduction potentials of the nickel complexes were too negative for electrochemical cycling. Of the copper complexes surveyed, the $[Cu_2(tpmc)(\mu\text{-}OH)]^{3+}$ complex (tpmc = bridging *N*,*N*′,*N*″,*N*‴-tetrakis(2-pyridylmethyl)-1,4,8,11-tetraazacyclotetradecane ligand)[25], demonstrated a viable reduction potential for CO_2 pumping and successful electrochemical CO_2 capture, increasing the solution concentration CO_2 from 10% to 75% in buffered aqueous solution (**Figure 0.4**). Electrochemical cycling unfortunately resulted in partial precipitation of the Cu^+ complex, an outcome which could potentially be improved upon with variation of supporting electrolytes or ligand.

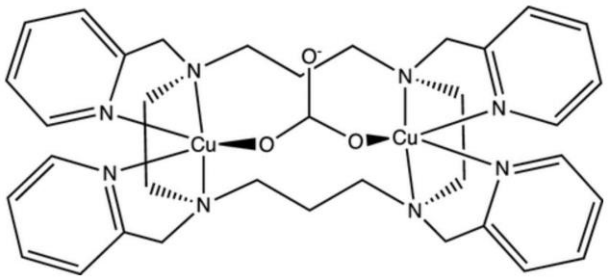

Figure 0.4: Carbonate adduct, $[Cu_2(tpmc)(\mu\text{-}CO_3)]^{2+}$ formed from $[Cu_2(tpmc)(\mu\text{-}OH)]^{3+}$.

0.4: Direct Air Capture and Carbenes

The transportation, buildings, and land-use/forestry sectors generate 40% of global CO_2 emissions. These are often referred to as "nonpoint sources" as they primarily consist of small, dispersed, and often mobile emissions.[26] While existing technologies are generally not equipped to effectively capture CO_2 from nonpoint source emitters, direct air capture (DAC) has been proposed as one viable approach to extracting CO_2 from the atmosphere. To meet the Paris Agreement, not only would all "point-source" processes need to approach net-zero carbon

emissions, but emissions from other distributed sources ("nonpoint sources") must also be significantly reduced or eliminated.[27] While there are currently fewer commercialized DAC processes, and those that exist are relatively small-scale, DAC is receiving increased attention and monetary support from public and private-sector organizations.[28]

After decades of research, most state-of-the-art amine capture systems still have high heating demands of ≥2.3 GJ/metric tonne CO_2 (≥100 kJ/mol CO_2). Therefore, current systems are limited to ≤22% of the Carnot efficiency, or <5% overall energetic efficiency, upon optimization at scale.[29–32] To put this efficiency into context, 20–30% of the entire power output of a typical coal-fired power plant is required to power a retrofitted CCC process alone.[33,34] CCC systems for DAC are underdeveloped, and the energy requirements are much higher due to the significantly lower CO_2 concentrations. It is estimated that existing thermochemical DAC systems require ≥4.3 GJ/ton CO_2 (or ≥190 kJ/mol CO_2), operating at ≤10% of the energetic efficiency, resulting in higher system costs.[35,36]

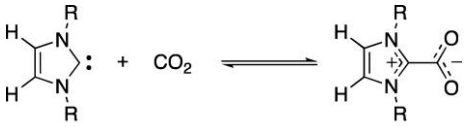

Figure 0.5: Addition of CO_2 to a carbene (NHC) to the zwitterionic imidazolium carboxylate.

Successful DAC requires a highly Lewis basic sorbent, with carbenes being a family of compounds that can easily capture CO_2 at low atmospheric concentrations. While they cannot directly participate in electrochemical cycling, there has been an interest in incorporating carbenes in carbon capture and utilization (CCU). CCU may greatly reduce the energy and money used to release and regenerate sorbents.[37] Once the sorbent captures CO_2, it can undergo further reactions to more valuable products.[38] Unlike amines, carbenes, specifically *N*-heterocyclic carbenes (NHCs), are prime candidates for the valorization of CO_2. Carbenes have been a class of compounds well-studied as transition metal ligands and organocatalysts, allowing them to have a compelling role in

heterogenous utilizations in capture and catalysis.[38,39] Upon reacting with CO_2, NHCs form an air-stable zwitterionic imidazolium carboxylate (**Figure 0.5**), which can hold and shuttle CO_2 into further reactions, such as the select carboxylation of other substrates.[40,41] The reactivity of carbenes and, thus, the binding strength to CO_2 can be tunable *via* electronic and steric modifications. Studies to further understand the trends of the carbene characteristics to their CO_2 binding affinity are crucial for improving the use of carbenes for CCU.

0.5: Outlook and Research Directions

This dissertation presents the investigative efforts into these developing branches of carbon capture research. The interest in the redox-active, basic guanidino functionalized aromatic 1,4-bis(tetramethylguanidino)benzene (1,4-btmgb) launched aqueous electrochemical studies on the potential for this complex to perform a pH swing. Results from the study with 1,4-btmgb shed light on the potential decomposition pathways that may hinder pH mediators.

The latter two studies in this dissertation highlight the results of dual computational and experimental efforts to understand a CO_2 capture system. A study with a Ru-PNP pincer complex, previously observed to bind to CO_2 *via* metal-ligand cooperation at a less than one-atom distance from the metal complex to the CO_2 binding site, inspired an experimental and computational exploration of the electrochemical behavior of the complex in organic solvents. Computational results further expand upon the Ru-PNP framework to survey different metal centers and substitution around the pincer ligand and the effects on the CO_2 affinity.

With the aid of computational efforts, a library of carbenes that participate in CO_2 capture at DAC levels was surveyed. From the observed correlation between the pK_a versus binding constant, it was key to identify the off-trend carbene variations and substituents that preferentially

bind to CO_2 instead of becoming protonated. Experimental studies corroborate the experimental values in how less bulky electron-donating substituents promoted better CO_2 affinity.

The outcomes of these studies underscore the wide range of possibilities that can be explored in carbon capture research. From these efforts, a perspective is offered towards a better understanding of the directions that carbon capture research can take.

0.6: References

(1) Hofmann, D. J.; Butler, J. H.; Tans, P. P. A New Look at Atmospheric Carbon Dioxide. *Atmos. Environ.* **2009**, *43* (12), 2084–2086. https://doi.org/10.1016/j.atmosenv.2008.12.028.

(2) Aaron, D.; Tsouris, C. Separation of CO2 from Flue Gas: A Review. *Sep. Sci. Technol.* **2005**, *40* (1–3), 321–348. https://doi.org/10.1081/SS-200042244.

(3) Friedlingstein, P.; O'Sullivan, M.; Jones, M. W.; Andrew, R. M.; Bakker, D. C. E.; Hauck, J.; Landschützer, P.; Le Quéré, C.; Luijkx, I. T.; Peters, G. P.; Peters, W.; Pongratz, J.; Schwingshackl, C.; Sitch, S.; Canadell, J. G.; Ciais, P.; Jackson, R. B.; Alin, S. R.; Anthoni, P.; Barbero, L.; Bates, N. R.; Becker, M.; Bellouin, N.; Decharme, B.; Bopp, L.; Brasika, I. B. M.; Cadule, P.; Chamberlain, M. A.; Chandra, N.; Chau, T.-T.-T.; Chevallier, F.; Chini, L. P.; Cronin, M.; Dou, X.; Enyo, K.; Evans, W.; Falk, S.; Feely, R. A.; Feng, L.; Ford, D. J.; Gasser, T.; Ghattas, J.; Gkritzalis, T.; Grassi, G.; Gregor, L.; Gruber, N.; Gürses, Ö.; Harris, I.; Hefner, M.; Heinke, J.; Houghton, R. A.; Hurtt, G. C.; Iida, Y.; Ilyina, T.; Jacobson, A. R.; Jain, A.; Jarníková, T.; Jersild, A.; Jiang, F.; Jin, Z.; Joos, F.; Kato, E.; Keeling, R. F.; Kennedy, D.; Klein Goldewijk, K.; Knauer, J.; Korsbakken, J. I.; Körtzinger, A.; Lan, X.; Lefèvre, N.; Li, H.; Liu, J.; Liu, Z.; Ma, L.; Marland, G.; Mayot, N.; McGuire, P. C.; McKinley, G. A.; Meyer, G.; Morgan, E. J.; Munro, D. R.; Nakaoka,

S.-I.; Niwa, Y.; O'Brien, K. M.; Olsen, A.; Omar, A. M.; Ono, T.; Paulsen, M.; Pierrot, D.; Pocock, K.; Poulter, B.; Powis, C. M.; Rehder, G.; Resplandy, L.; Robertson, E.; Rödenbeck, C.; Rosan, T. M.; Schwinger, J.; Séférian, R.; Smallman, T. L.; Smith, S. M.; Sospedra-Alfonso, R.; Sun, Q.; Sutton, A. J.; Sweeney, C.; Takao, S.; Tans, P. P.; Tian, H.; Tilbrook, B.; Tsujino, H.; Tubiello, F.; van der Werf, G. R.; van Ooijen, E.; Wanninkhof, R.; Watanabe, M.; Wimart-Rousseau, C.; Yang, D.; Yang, X.; Yuan, W.; Yue, X.; Zaehle, S.; Zeng, J.; Zheng, B. Global Carbon Budget 2023. *Earth Syst. Sci. Data* **2023**, *15* (12), 5301–5369. https://doi.org/10.5194/essd-15-5301-2023.

(4) De Luna, P.; Hahn, C.; Higgins, D.; Jaffer, S. A.; Jaramillo, T. F.; Sargent, E. H. What Would It Take for Renewably Powered Electrosynthesis to Displace Petrochemical Processes? *Science* **2019**, *364* (6438), eaav3506. https://doi.org/10.1126/science.aav3506.

(5) Davis, J.; Rochelle, G. Thermal Degradation of Monoethanolamine at Stripper Conditions. *Energy Procedia* **2009**, *1* (1), 327–333. https://doi.org/10.1016/j.egypro.2009.01.045.

(6) Zito, A. M.; Clarke, L. E.; Barlow, J. M.; Bím, D.; Zhang, Z.; Ripley, K. M.; Li, C. J.; Kummeth, A.; Leonard, M. E.; Alexandrova, A. N.; Brushett, F. R.; Yang, J. Y. Electrochemical Carbon Dioxide Capture and Concentration. *Chem. Rev.* **2023**, *123* (13), 8069–8098. https://doi.org/10.1021/acs.chemrev.2c00681.

(7) House, K. Z.; Harvey, C. F.; Aziz, M. J.; Schrag, D. P. The Energy Penalty of Post-Combustion CO2 Capture & Storage and Its Implications for Retrofitting the U.S. Installed Base. *Energy Environ. Sci.* **2009**, *2* (2), 193–205. https://doi.org/10.1039/B811608C.

(8) Dubois, D. L.; Miedaner, A.; Bell, W.; Smart, J. C. Electrochemical concentration of carbon dioxide. In *Electrochemical and Electrocatalytic Reactions of Carbon Dioxide*; Elsevier, 1993; pp 94–117. https://doi.org/10.1016/B978-0-444-88316-2.50008-5.

(9) Zito, A.; Clarke, L.; Barlow, J.; Bim, D.; Zhang, Z.; Ripley, K.; Li, C.; Kummeth, A.; Leonard, M.; Alexandrova, A.; Brushett, F.; Yang, J. Electrochemical Carbon Dioxide Capture and Concentration. *Chem Rev* **2022**.

(10) Cao, T. N.-D.; Snyder, S. W.; Lin, Y.-I.; Lin, Y. J.; Negi, S.; Pan, S.-Y. Unraveling the Potential of Electrochemical pH-Swing Processes for Carbon Dioxide Capture and Utilization. *Ind. Eng. Chem. Res.* **2023**, *62* (49), 20979–20995. https://doi.org/10.1021/acs.iecr.3c02183.

(11) Eisaman, M. D.; Alvarado, L.; Larner, D.; Wang, P.; Garg, B.; Littau, K. A. CO2 Separation Using Bipolar Membrane Electrodialysis. *Energy Environ. Sci.* **2011**, *4* (4), 1319–1328. https://doi.org/10.1039/C0EE00303D.

(12) Eisaman, M. D.; Parajuly, K.; Tuganov, A.; Eldershaw, C.; Chang, N.; Littau, K. A. CO2 Extraction from Seawater Using Bipolar Membrane Electrodialysis. *Energy Environ. Sci.* **2012**, *5* (6), 7346–7352. https://doi.org/10.1039/C2EE03393C.

(13) Xie, H.; Wu, Y.; Liu, T.; Wang, F.; Chen, B.; Liang, B. Low-Energy-Consumption Electrochemical CO2 Capture Driven by Biomimetic Phenazine Derivatives Redox Medium. *Appl. Energy* **2020**, *259*, 114119. https://doi.org/10.1016/j.apenergy.2019.114119.

(14) Jin, S.; Wu, M.; Gordon, R. G.; Aziz, M. J.; Kwabi, D. G. pH Swing Cycle for CO_2 Capture Electrochemically Driven through Proton-Coupled Electron Transfer. *Energy Environ. Sci.* **2020**, *13* (10), 3706–3722. https://doi.org/10.1039/D0EE01834A.

(15) Jin, S.; Wu, M.; Jing, Y.; Gordon, R. G.; Aziz, M. J. Low Energy Carbon Capture via Electrochemically Induced pH Swing with Electrochemical Rebalancing. *Nat. Commun.* **2022**, *13* (1), 2140. https://doi.org/10.1038/s41467-022-29791-7.

(16) Huang, C.; Liu, C.; Wu, K.; Yue, H.; Tang, S.; Lu, H.; Liang, B. CO2 Capture from Flue Gas Using an Electrochemically Reversible Hydroquinone/Quinone Solution. *Energy Fuels* **2019**, *33* (4), 3380–3389. https://doi.org/10.1021/acs.energyfuels.8b04419.

(17) Watkins, J. D.; Siefert, N. S.; Zhou, X.; Myers, C. R.; Kitchin, J. R.; Hopkinson, D. P.; Nulwala, H. B. Redox-Mediated Separation of Carbon Dioxide from Flue Gas. *Energy Fuels* **2015**, *29* (11), 7508–7515. https://doi.org/10.1021/acs.energyfuels.5b01807.

(18) Seo, H.; Rahimi, M.; Hatton, T. A. Electrochemical Carbon Dioxide Capture and Release with a Redox-Active Amine. *J. Am. Chem. Soc.* **2022**, *144* (5), 2164–2170. https://doi.org/10.1021/jacs.1c10656.

(19) Xie, H.; Jiang, W.; Liu, T.; Wu, Y.; Wang, Y.; Chen, B.; Niu, D.; Liang, B. Low-Energy Electrochemical Carbon Dioxide Capture Based on a Biological Redox Proton Carrier. *Cell Rep. Phys. Sci.* **2020**, *1* (5), 100046. https://doi.org/10.1016/j.xcrp.2020.100046.

(20) Zeebe, R. E.; Wolf-Gladrow. *CO2 in Seawater: Equilibrium, Kinetics, Isotopes*; 2001.

(21) Kajiwara, T.; Yamaguchi, T.; Kido, H.; Kawabata, S.; Kuroda, R.; Ito, T. A Dinucleating Bis(Dimethylcyclam) Ligand and Its Dinickel(II) and Dizinc(II) Complexes with the Face-to-Face Ring Arrangement. *Inorg. Chem.* **1993**, *32* (23), 4990–4991. https://doi.org/10.1021/ic00075a003.

(22) Murase, I.; Vuckovic, G.; Kodera, M.; Harada, H.; Matsumoto, N.; Kida, S. Synthesis and Characterization of Copper(II), Nickel(II), and Cobalt(II) Binuclear Complexes with a New Tricyclic Octadentate Ligand, 1,5,8,12,15,19,22,26-Octaazatricyclo[17.9.2.25,15]Dotriacontane (Tcoa): Trapping of Carbon Dioxide in a Neutral Aqueous Solution. *Inorg. Chem.* **1991**, *30* (4), 728–733. https://doi.org/10.1021/ic00004a024.

(23) Harada, H.; Kodera, M.; Vuckovic, G.; Matsumoto, N.; Kida, S. Preparation and Redox Chemistry of Novel Carbonato-Bridged Cobalt(II) Complexes with 1,4,8,11-Tetrakis(2-Aminoethyl)-1,4,8,11-Tetraazacyclotetradecane and 1,4,8,11-Tetrakis(Pyridylmethyl)-1,4,8,11-Tetraazacyclotetradecane. *Inorg. Chem.* **1991**, *30* (6), 1190–1194. https://doi.org/10.1021/ic00006a007.

(24) Newell, R.; Appel, A.; DuBois, D. L.; Rakowski DuBois, M. Studies of Bicarbonate Binding by Dinuclear and Mononuclear Ni(II) Complexes. *Inorg. Chem.* **2005**, *44* (2), 365–373. https://doi.org/10.1021/ic049202c.

(25) Appel, A. M.; Newell, R.; DuBois, D. L.; Rakowski DuBois, M. Concentration of Carbon Dioxide by Electrochemically Modulated Complexation with a Binuclear Copper Complex. *Inorg. Chem.* **2005**, *44* (9), 3046–3056. https://doi.org/10.1021/ic050023k.

(26) Ritchie, H.; Roser, M.; Rosado, P. CO_2 and Greenhouse Gas Emissions. *Our World Data* **2020**.

(27) Tavoni, M.; van der Zwaan, B. Nuclear Versus Coal plus CCS: A Comparison of Two Competitive Base-Load Climate Control Options. *Environ. Model. Assess.* **2011**, *16* (5), 431–440. https://doi.org/10.1007/s10666-011-9259-1.

(28) *Direct Air Capture 2022 – Analysis - IEA*. https://www.iea.org/reports/direct-air-capture-2022 (accessed 2024-09-12).

(29) Abu-Zahra, M. R. M.; Schneiders, L. H. J.; Niederer, J. P. M.; Feron, P. H. M.; Versteeg, G. F. CO2 Capture from Power Plants. *Int. J. Greenh. Gas Control* **2007**, *1* (1), 37–46. https://doi.org/10.1016/S1750-5836(06)00007-7.

(30) Goto, K.; Kodama, S.; Okabe, H.; Fujioka, Y. Energy Performance of New Amine-Based Solvents for CO2 Capture from Blast Furnace Gas. In *Recent Advances in Post-Combustion CO2 Capture Chemistry*; ACS Symposium Series; American Chemical Society, 2012; Vol. 1097, pp 317–331. https://doi.org/10.1021/bk-2012-1097.ch017.

(31) Singh, A.; Stéphenne, K. Shell Cansolv CO2 Capture Technology: Achievement from First Commercial Plant. *Energy Procedia* **2014**, *63*, 1678–1685. https://doi.org/10.1016/j.egypro.2014.11.177.

(32) Yulia, F.; Sofianita, R.; Prayogo, K.; Nasruddin, N. Optimization of Post Combustion CO2 Absorption System Monoethanolamine (MEA) Based for 320 MW Coal-Fired Power Plant Application – Exergy and Exergoenvironmental Analysis. *Case Stud. Therm. Eng.* **2021**, *26*, 101093. https://doi.org/10.1016/j.csite.2021.101093.

(33) Rochelle, G.; Chen, E.; Freeman, S.; Van Wagener, D.; Xu, Q.; Voice, A. Aqueous Piperazine as the New Standard for CO2 Capture Technology. *Chem. Eng. J.* **2011**, *171* (3), 725–733. https://doi.org/10.1016/j.cej.2011.02.011.

(34) Boot-Handford, M. E.; Abanades, J. C.; Anthony, E. J.; Blunt, M. J.; Brandani, S.; Dowell, N. M.; Fernández, J. R.; Ferrari, M.-C.; Gross, R.; Hallett, J. P.; Haszeldine, R. S.; Heptonstall, P.; Lyngfelt, A.; Makuch, Z.; Mangano, E.; Porter, R. T. J.; Pourkashanian, M.; Rochelle, G. T.; Shah, N.; Yao, J. G.; Fennell, P. S. Carbon Capture and Storage Update. *Energy Environ. Sci.* **2013**, *7* (1), 130–189. https://doi.org/10.1039/C3EE42350F.

(35) House, K. Z.; Baclig, A. C.; Ranjan, M.; van Nierop, E. A.; Wilcox, J.; Herzog, H. J. Economic and Energetic Analysis of Capturing CO2 from Ambient Air. *Proc. Natl. Acad. Sci.* **2011**, *108* (51), 20428–20433. https://doi.org/10.1073/pnas.1012253108.

(36) Fasihi, M.; Efimova, O.; Breyer, C. Techno-Economic Assessment of CO2 Direct Air Capture Plants. *J. Clean. Prod.* **2019**, *224*, 957–980. https://doi.org/10.1016/j.jclepro.2019.03.086.

(37) Stiernet, P.; Pang, B.; Taton, D.; Yuan, J. The Promise of *N*-Heterocyclic Carbenes to Capture and Valorize Carbon Dioxide. *Sustain. Chem. Clim. Action* **2023**, *2*, 100018. https://doi.org/10.1016/j.scca.2023.100018.

(38) Gulati, S.; Vijayan, S.; Mansi; Kumar, S.; Harikumar, B.; Trivedi, M.; Varma, R. S. Recent Advances in the Application of Metal-Organic Frameworks (MOFs)-Based Nanocatalysts for Direct Conversion of Carbon Dioxide (CO2) to Value-Added Chemicals. *Coord. Chem. Rev.* **2023**, *474*, 214853. https://doi.org/10.1016/j.ccr.2022.214853.

(39) Yang, Z.-Z.; He, L.-N.; Zhao, Y.-N.; Li, B.; Yu, B. CO2 Capture and Activation by Superbase/Polyethylene Glycol and Its Subsequent Conversion. *Energy Environ. Sci.* **2011**, *4* (10), 3971–3975. https://doi.org/10.1039/C1EE02156G.

(40) Fu, H.-C.; You, F.; Li, H.-R.; He, L.-N. CO2 Capture and in Situ Catalytic Transformation. *Front. Chem.* **2019**, *7*. https://doi.org/10.3389/fchem.2019.00525.

(41) Finger, L. H.; Guschlbauer, J.; Harms, K.; Sundermeyer, J. N-Heterocyclic Olefin–Carbon Dioxide and –Sulfur Dioxide Adducts: Structures and Interesting Reactivity Patterns. *Chem. – Eur. J.* **2016**, *22* (45), 16292–16303. https://doi.org/10.1002/chem.201602973.

Chapter 1: Aqueous Electrochemical and pH Studies of Redox-Active Guanidino Functionalized Aromatics for CO_2 Capture

Portions of this chapter have been published:

Li, C. J.; Ziller, J. W.; Barlow, J. M.; Yang, J. Y. *ACS Org. & Inorg. Au* **2024**, *4* (4) 387-394.

1.1 Introduction

One common motif for ambient electrochemical CO_2 capture and concentration uses redox active molecules that either (1) directly bind to and release CO_2 or (2) modify the pH of aqueous solutions (**Scheme 1.1**).[1] In the first approach, redox carriers bind CO_2 in their electron-rich reduced form (**Scheme 1.1**, red pathway). Subsequent electrochemical oxidation decreases the redox carrier's electron density, lowering its CO_2 binding affinity and releasing concentrated CO_2. The redox carrier can then be regenerated for CO_2 capture via electrochemical reduction.[2] Another approach uses redox chemistry to change the pH of an aqueous solution for CO_2 capture and release (**Scheme 1.1**, blue pathway). These pH swing cycles capitalize on pH-dependent CO_2 equilibria in aqueous solutions. At high pH values, hydroxide reacts with CO_2 to form bicarbonate and carbonate, enabling capture from dilute streams. At low pH values, the equilibrium is reversed, and CO_2 is released. Redox-active molecules whose proton affinity (pK_a) significantly varies depending on their oxidation state are used to induce these electrochemically driven pH swings.[3] Guanidines are a family of neutral organic Brønsted superbases (pK_a values of 12 or greater in water) with attractive CO_2 capture properties.[4] They bind CO_2 through two different mechanisms, depending on the solvent. These mechanisms parallel the two capture routes shown in **Scheme 1.1**.[2] In aprotic solvents, tetramethyl guanidine (TMG) binds directly to CO_2 to form a zwitterionic carbamate salt (**Scheme 1.2**, pathway A).[5] In protic solvents such as alcohols or water, sufficiently Brønsted basic guanidine deprotonates the alcohol

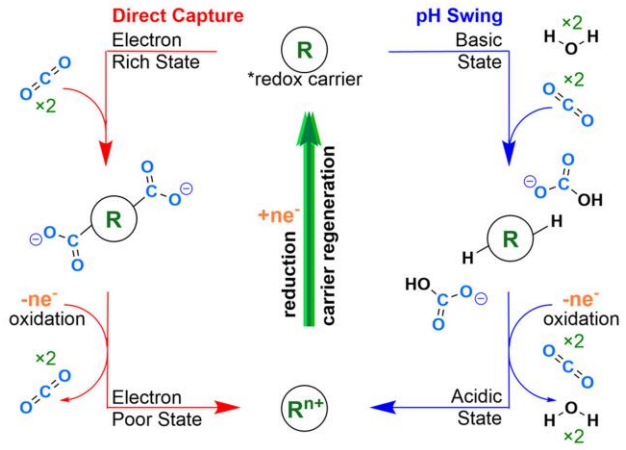

Scheme 1.1: Two Modes of CO_2 Capture by a Redox-Active Molecule (R) via Direct Capture or pH Swing Methods

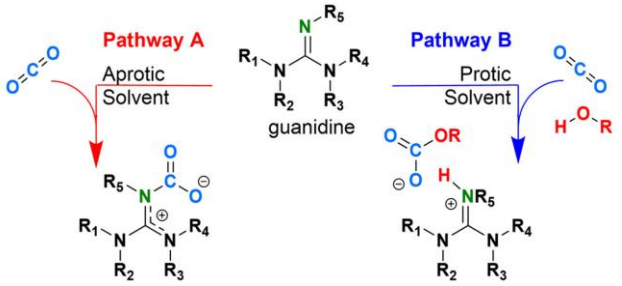

Scheme 1.2: Modes of CO_2 Capture by Guanidines

or water, which then binds CO_2 to form an alkyl carbonate or carbonate ion pair with the protonated TMG (**Scheme 1.2**, pathway B).[6] Because of their reactivity with CO_2, guanidine derivatives have been studied for their use in thermal capture and release cycles. Heldebrandt and co-workers developed a new class of CO_2-binding organic liquids composed of alcohol solvents and TMG derivatives.[6] Direct air capture (DAC) of CO_2 by a family of bis-iminoguanidine has been studied by Custelcean and co-workers.[7–9] The resulting bis-iminoguanidine carbamate salts can be heated to regenerate the sorbent (80−120 °C).[8,9] The lack of reversible redox properties in the previously studied guanidine compounds limited their use as sorbents in thermal regeneration cycles. However, Himmel and co-workers recently synthesized TMG-substituted functionalized aromatics, or guanidino functionalized aromatics (GFAs), with reversible redox properties.[10] These redox-active superbases have not been assessed for electrochemical CO_2 capture and release. A variety of GFAs can be obtained through straightforward synthetic routes. Among these, 1,4-bis-(tetramethylguanidino)benzene (1,4-btmgb) was selected for testing due to its mild redox potential and stability in air. In this study, we explored the use of 1,4-btmgb in organic and aqueous solutions to assess its viability as a redox carrier and pH swing mediator for electrochemical CO_2 capture.

1.2 Results and Discussion

1.2.1 Synthesis of GFAs

Compounds 1,4-btmgb and the doubly oxidized form, 1,4-btmgb$[BF_4]_2$, were synthesized as described by Himmel and co-workers (**Scheme 1.3**).[10] In addition, the previously unreported conjugate acids $[1,4\text{-btmgbH}_2]^{2+}$ with PF_6^- and Cl^- counteranions and the monoprotonated [1,4-

btmgbH]$^{+}$ with BF_4^- or PF_6^- counteranions were also synthesized. These protonated compounds were characterized via ^{1}H and $^{13}C\{^{1}H\}$ NMR spectroscopy and X-ray crystallography (**Figures 1.1−1.2**).

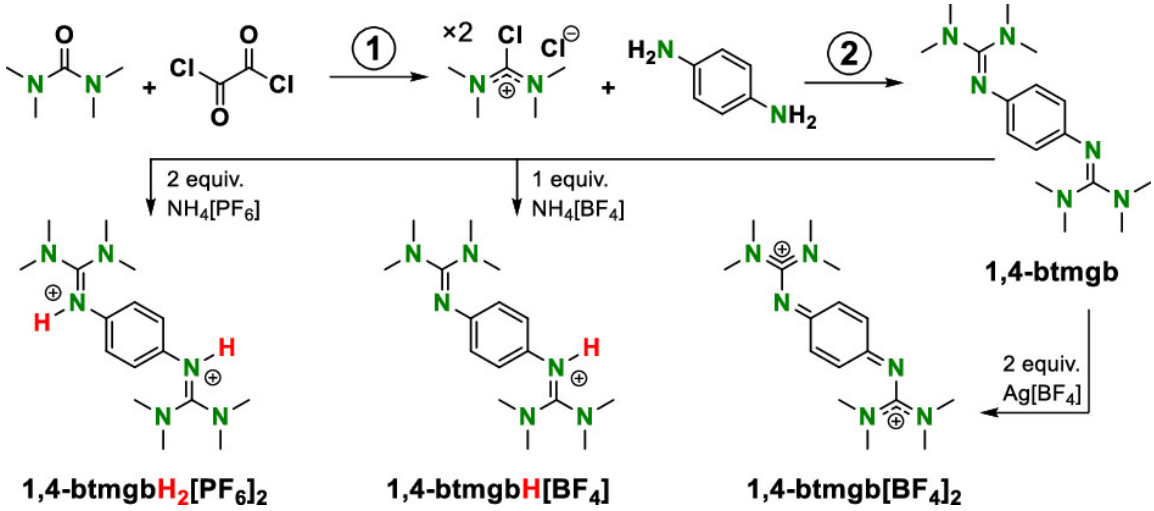

Scheme 1.3: Synthesis of 1,4-btmgb, 1,4-btmgb^{2+}, and 1,4-btmgbH$_2^{2+}$

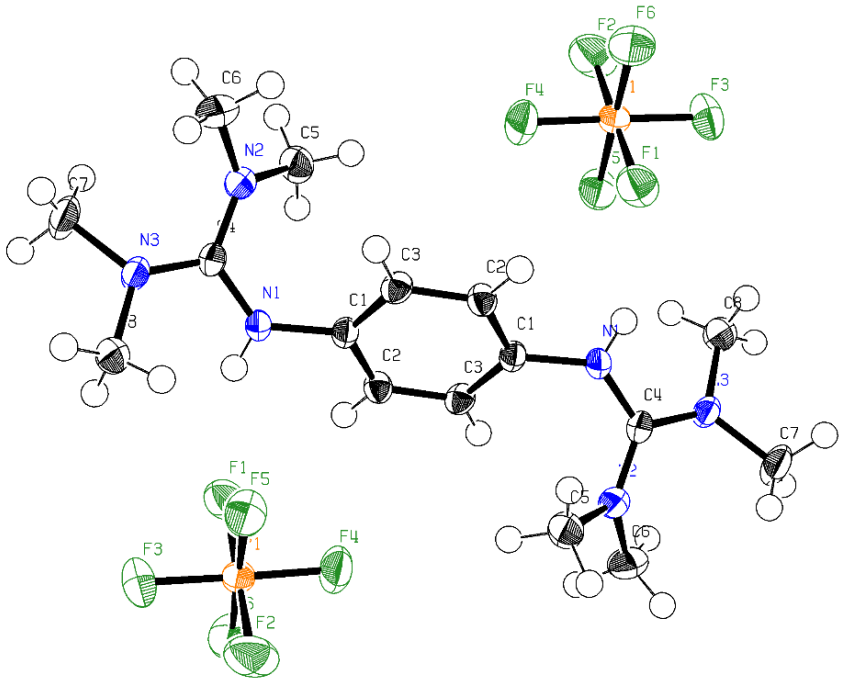

Figure 1.1: ORTEP structure of 1,4 btmgbH$_2$[PF$_6$]$_2$. Thermal ellipsoids are shown at 80% probability. See refinement data below in **Crystallographic Information 1.5.**

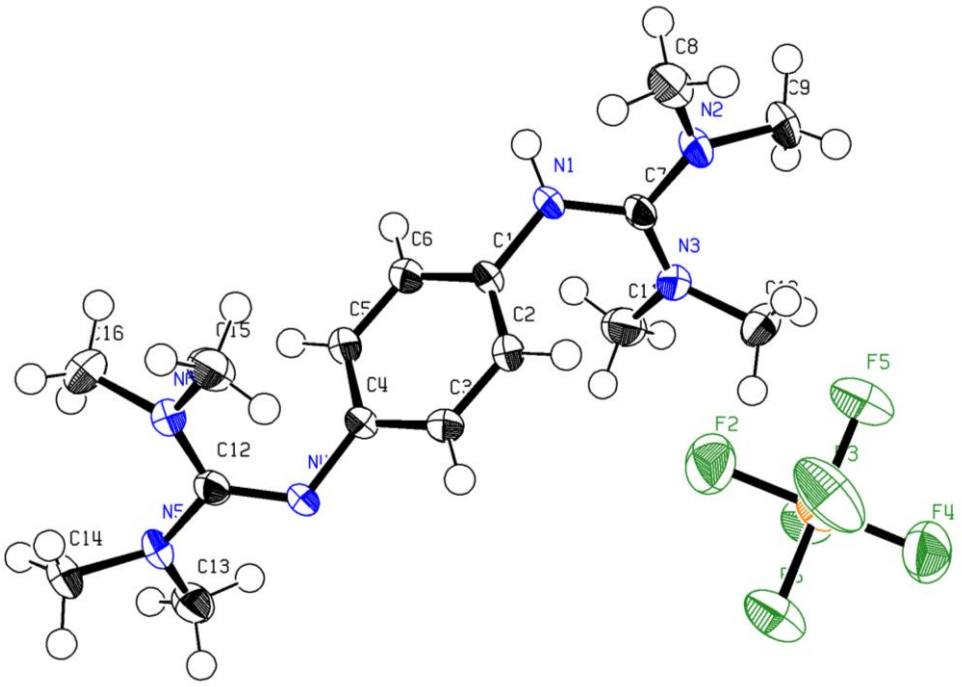

Figure 1.2: ORTEP of monoprotonated 1,4-btmgbH[PF_6]. Thermal ellipsoids are shown at 80% probability. See refinement data below in **Crystallographic Information 1.5**.

1.2.2 pK_a and Electrochemical Properties in Acetonitrile

The p*K*a values for $[1,4\text{-btmgbH}_2]^{2+}$ were previously reported in acetonitrile (MeCN) as 19.3 and 22.1, respectively.[11] In MeCN, the cyclic voltammogram (CV) of the fully deprotonated 1,4-btmgb has a reversible two-electron oxidation with an $E_{1/2}$ at −0.25 V *vs* ferrocenium/ferrocene ($Fe(C_5H_5)_2^{+/0}$) (ΔE = 0.030 V) (**Figure 1.3**).

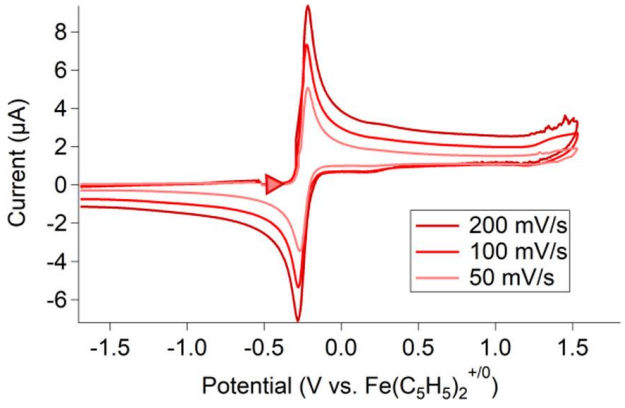

Figure 1.3: 1,4-btmgb (1 mM) in MeCN with $TBAPF_6$ as the supporting electrolyte (100 mM) at varied scan rates.

This redox behavior is consistent with the previous reports of 1,4-btmgb in other organic solvents referenced to ferrocene, which described a reversible two-electron reduction at −0.18 V in DCM and −0.26 V in THF.[10] The CV of the doubly protonated species, $[1,4\text{-btmgbH}_2]^{2+}$, is shown in

Figure 1.4. This species has irreversible oxidation events at the more anodic potentials of 1.12 and 1.39 V *vs* $Fe(C_5H_5)_2^{+/0}$. After oxidation, the subsequent reduction at −0.33 V is approximate to the potential for the reduction of $[1,4\text{-btmgb}]^{2+}$ seen in the CV of deprotonated $[1,4\text{-btmgb}]^{2+}$/1,4-btmgb (**Figure 1.3**). Oxidation of $[1,4\text{-btmgbH}_2]^{2+}$ by two electrons is expected to result in an increase in acidity. We believe that $[1,4\text{-btmgbH}_2]^{4+}$ (formed upon the oxidation of $[1,4\text{-btmgbH}_2]^{2+}$) is deprotonated, despite the lack of an added base, to form the more stable $1,4\text{-btmgb}^{2+}$. The CV trace for the monoprotonated species (**Figure 1.5**) maintains a one-electron redox couple centered at −0.24 V, a lone reduction event at 0.39 V, and oxidation peaks at 1.19 and 1.30 V *vs* $Fe(C_5H_5)_2^{+/0}$.

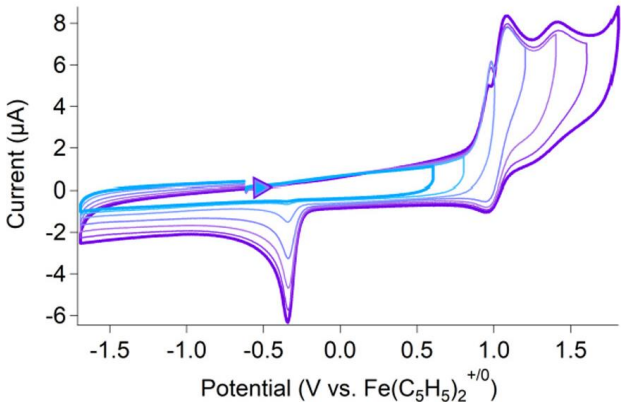

Figure 1.4: Varied scan window of 1,4-btmgbH$_2$[PF$_6$]$_2$ (scan rate = 500 mV/s) in MeCN, with 100 mM TBAPF$_6$ as the supporting electrolyte and a glassy carbon counter electrode.

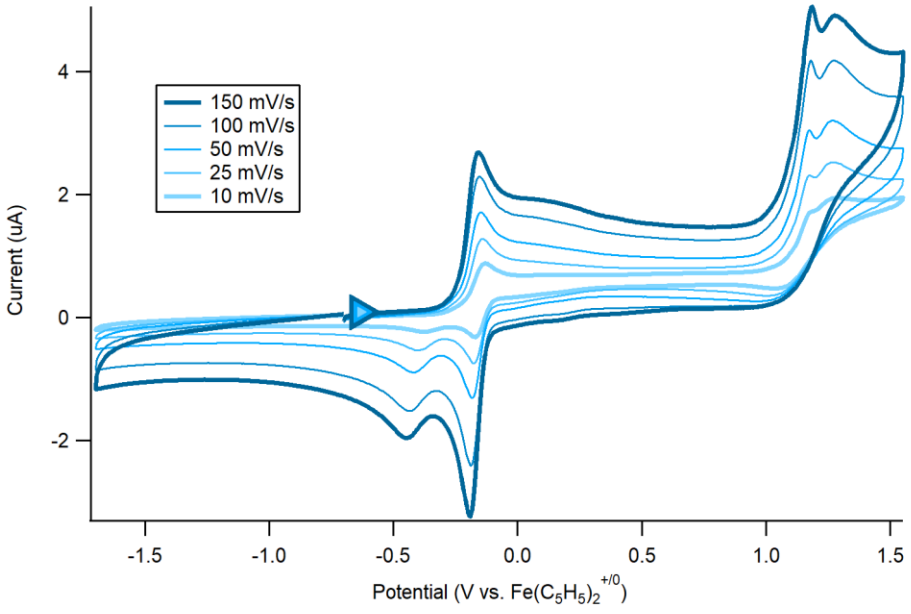

Figure 1.5: 1 mM 1,4-btmgbH[PF$_6$] in MeCN with 100 TMAPF$_6$, varied scan rate.

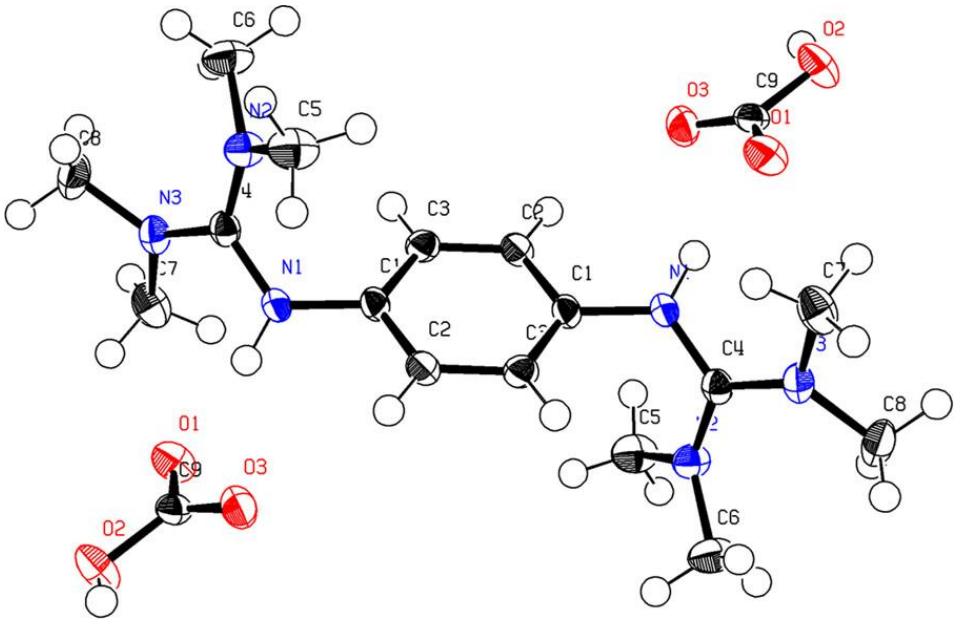

Figure 1.6: X-ray crystal structure of 1,4-btmgb$H_2(HCO_3^-)_2$. Thermal ellipsoids are shown at 80% probability. Refinement data can be found below in **Crystallographic Information 1.5 Table 1.2**.

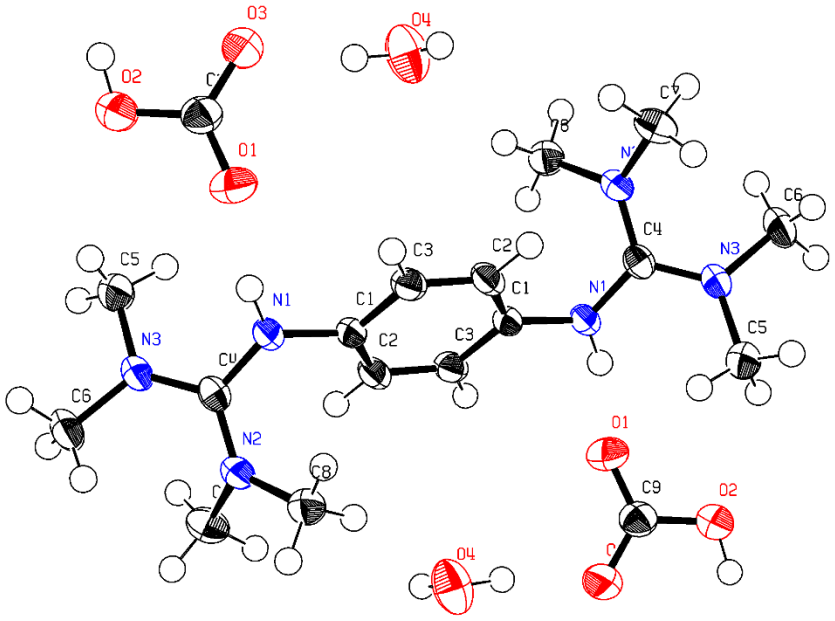

Figure 1.7: ORTEP of 1,4-btmgb$H_2(HCO_3^-)_2 \cdot (H_2O)_2$, ellipsoids are shown at 80% probability. See refinement data before in **Crystallographic Information 1.5**.

1.2.3 Reactivity with CO_2

The CO_2 capture capability of 1,4-btmgb was assessed in MeCN, with CO_2 being added to solutions of 1,4-btmgb under different conditions. Sparging CO_2 into a 1 mM solution of 1,4-

btmgb in MeCN with trace water resulted in the formation of a white precipitate. Single crystals of this product, suitable for analysis by X-ray crystallography, were grown from a solution of concentrated 1,4-btmgb dissolved in MeCN under a CO_2 headspace. The analysis reveals the formation of protonated 1,4-btmgb with bicarbonate anions (1,4-btmgb$H_2(HCO_3^-)_2$) (**Figure 1.6**). Other attempts to recrystallize 1,4-btmgb with CO_2 in MeCN resulted in a similar structure but with two water molecules to give 1,4 btmgb$H_2(HCO_3^-)_2 \cdot (H_2O)_2$ (**Figure 1.7**). The formation of a carbonate salt was also present in pure water, supported by ^{1}H NMR spectroscopic analysis. The ^{1}H NMR spectrum of 1,4-btmgb in D_2O have signals at δ 6.85 and 2.82 ppm, which shift to 7.11 and 2.97 ppm, respectively, after sparging with CO_2 for 5 min (**Figures 1.8** and **1.9**). After CO_2 exposure, these signals are identical to those found for doubly protonated 1,4-btmgb$H_2[PF_6]_2$ in D_2O (**Figure 1.10**). The $^{13}C\{^1H\}$ NMR of 1,4-btmgb in D_2O with added CO_2 is the same as that of 1,4-btmgb$H_2[PF_6]_2$ with two additional resonances observed at δ 124.8 and δ 160.3 ppm which correspond to dissolved free CO_2 in solution and bicarbonate (HCO_3^-), respectively.[12,13]

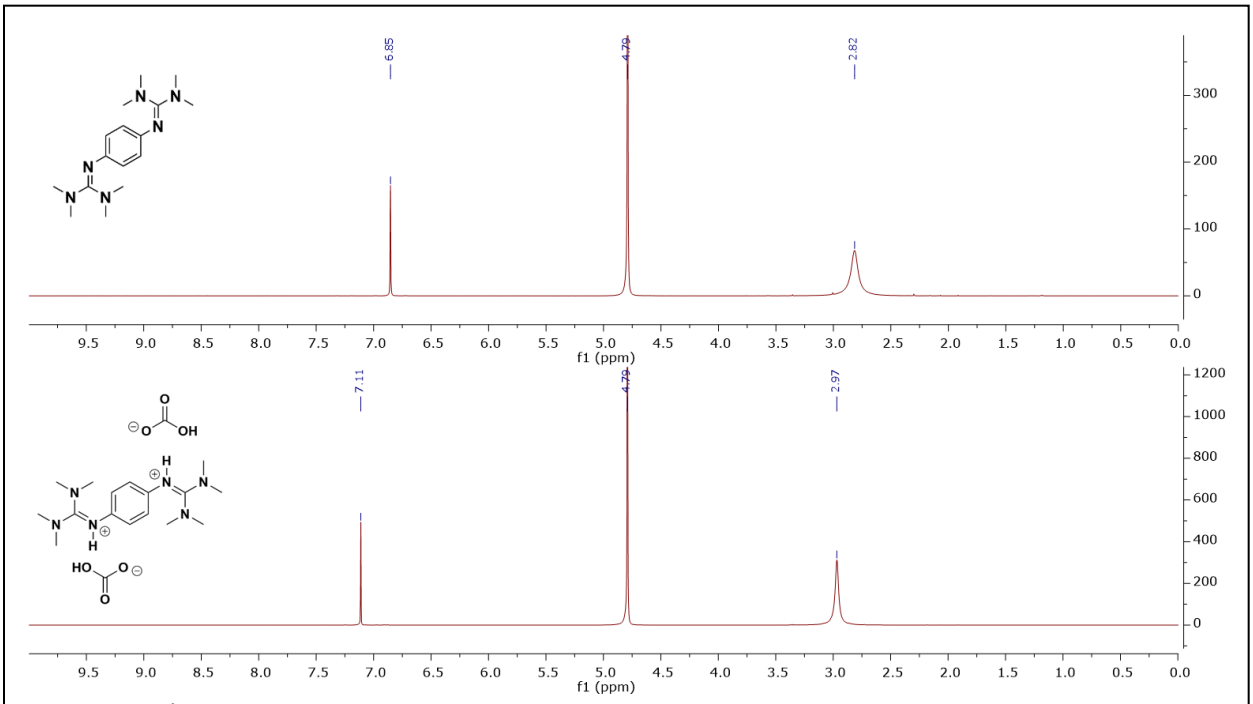

Figure 1.8: ^{1}H NMR of 1,4-btmgb in D_2O, 600 Hz, 293 K, under 1 atm N_2 (top) and under 1 atm of CO_2 (bottom).

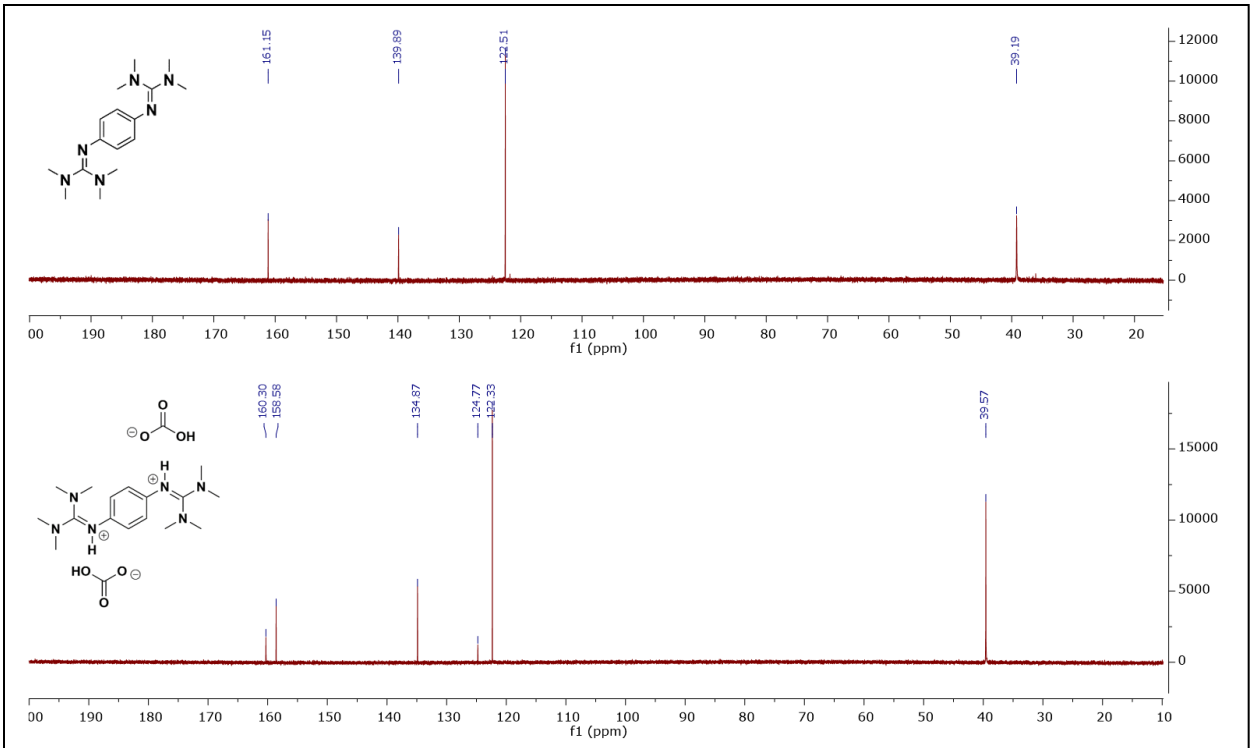

Figure 1.9: $^{13}C\{^{1}H\}$ NMR of 1,4-btmgb in D_2O, 151 Hz, 293 K, under 1 atm N_2 (top) and under 1 atm CO_2 (bottom).

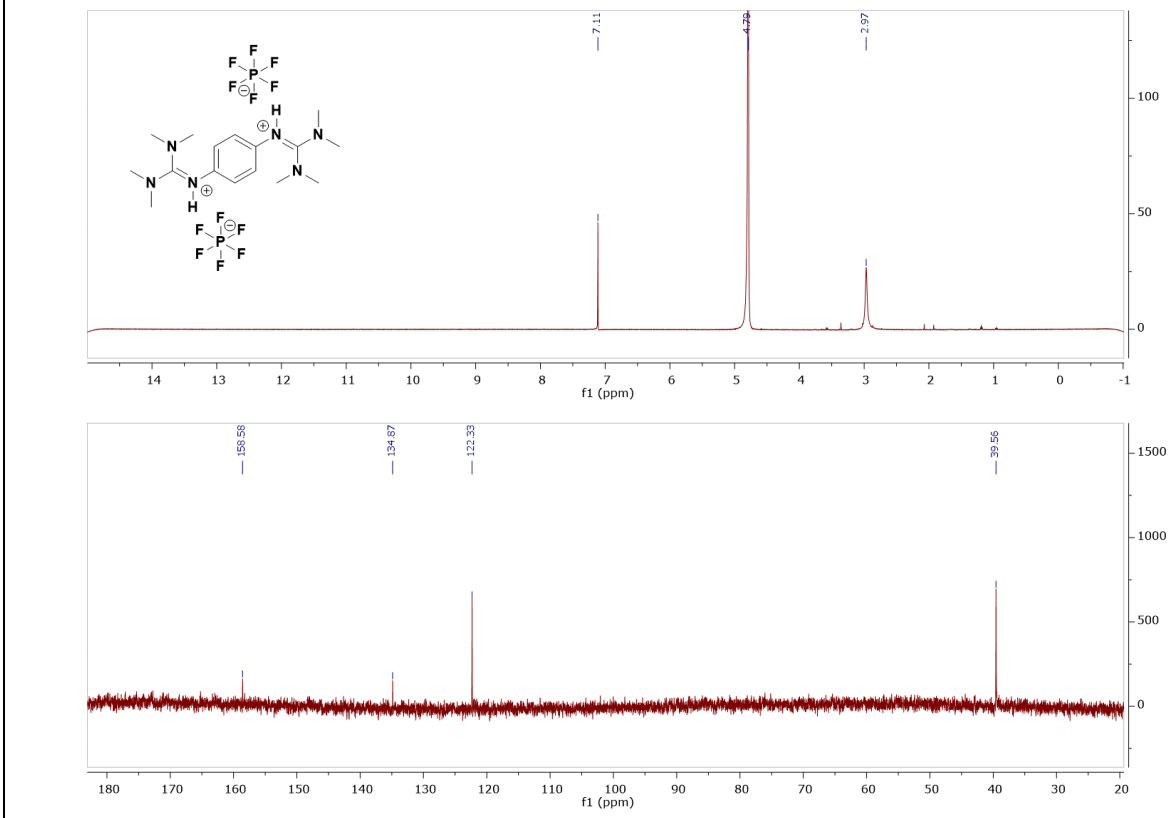

Figure 1.10: NMR spectra of **1,4-btmgbH$_2$[PF$_6$]$_2$** in D_2O ^{1}H NMR 600 Hz, 293 K (top), and $^{13}C\{^{1}H\}$ at 151 Hz, 293 K (bottom).

1.2.4 pK_a and Electrochemical Properties in Protic Solvents

Since even trace water in aprotic solvents results in the formation of the protonated base and bicarbonate, we postulate that 1,4-btmgb is a better candidate for an aqueous electrochemical pH swing cycle than direct capture. To assess the suitability of 1,4-btmgb for an aqueous electrochemical pH swing, we first sought to determine the pK_a values for $[1,4\text{-btmgbH}_2]^{2+}$ in water. Compared to the CVs obtained on 1,4-btmgb at various stages of protonation in MeCN (**Figures 1.3–1.5**), the CVs of 1,4-btmgb in water varied with pH (**Figures 1.11−1.14**), reflecting different protonation states. The relationship be-

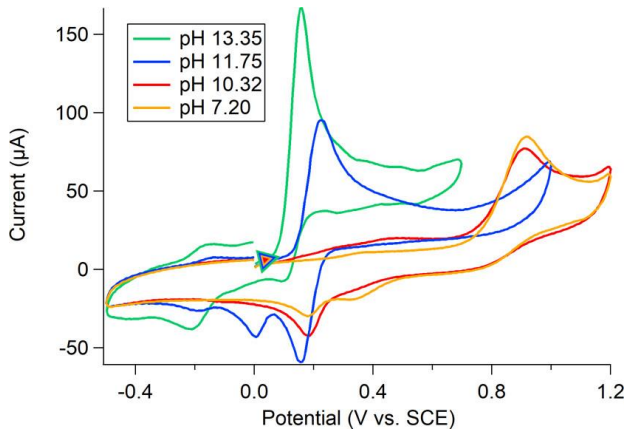

Figure 1.11: CVs of 1,4-btmgb in 100 mM KCl in H_2O at various pH values.

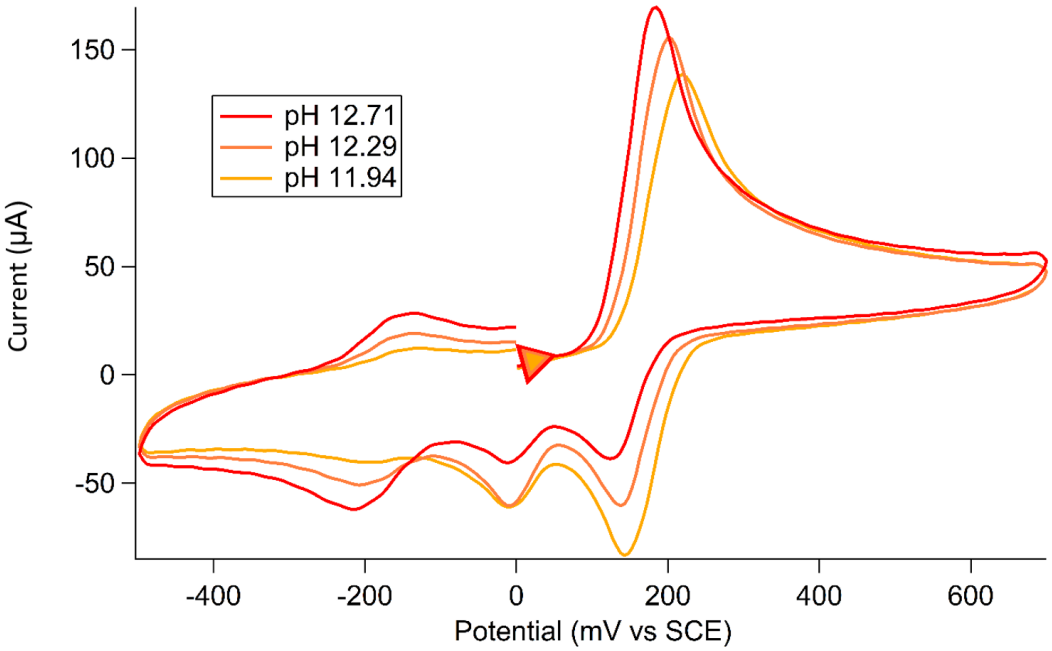

Figure 1.12: Cyclic voltammetry of 1 mM 1,4-btmgb vs SCE in water with 100 mM KCl at varied alkaline conditions by the additions of concentrated NaOH, scan rate = 400 mV/s.

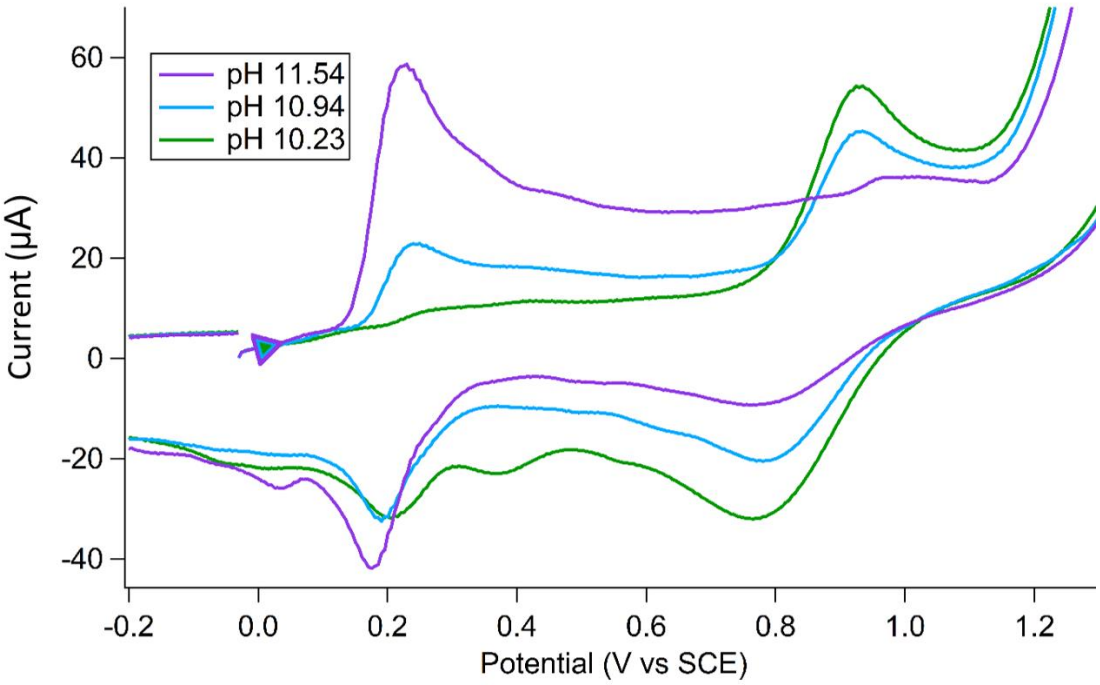

Figure 1.13: Cyclic voltammetry of 1 mM 1,4-btmgb in water with 100 mM KCl, scan rate of 100 mV/s. Varied solution pH with additions of 1 M HCl.

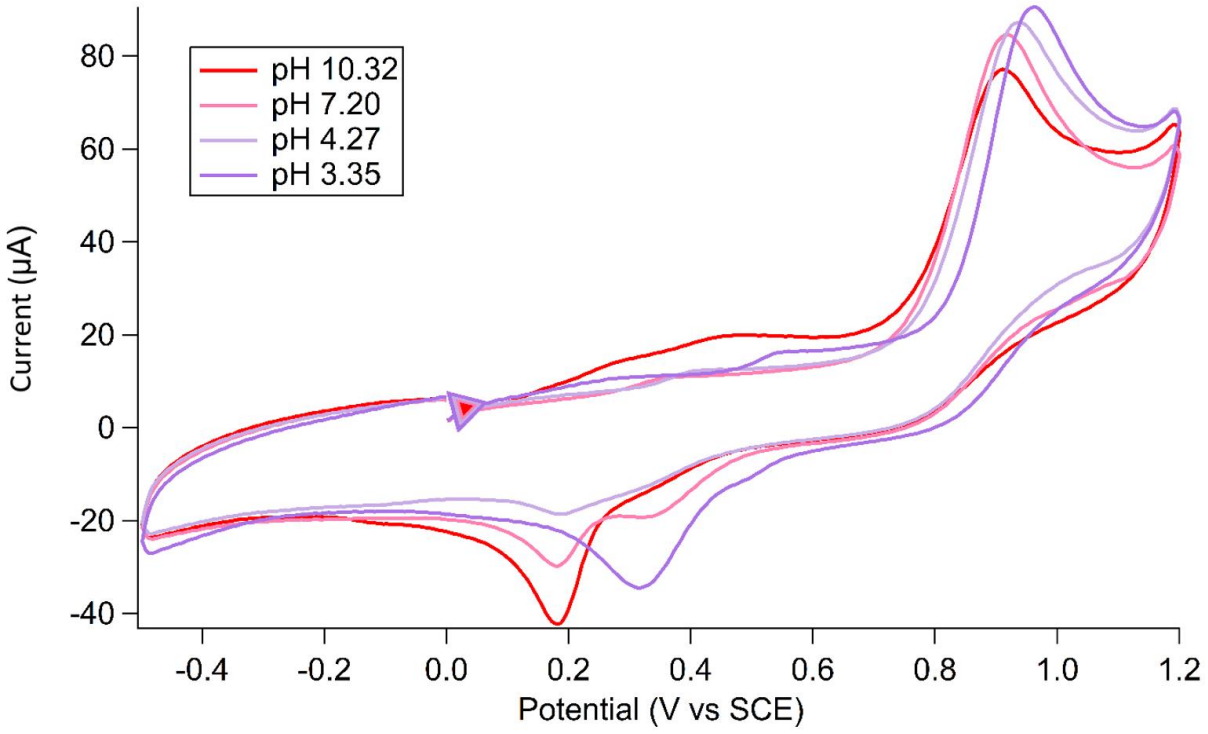

Figure 1.14: Cyclic voltammetry of 1 mM 1,4-btmgb (protonated to 1,4-btmgbH_2^{2+} by solution pH) in water with 100 mM KCl, scan rate 400 mV/s. Varied solution pH with additions of 1 M HCl.

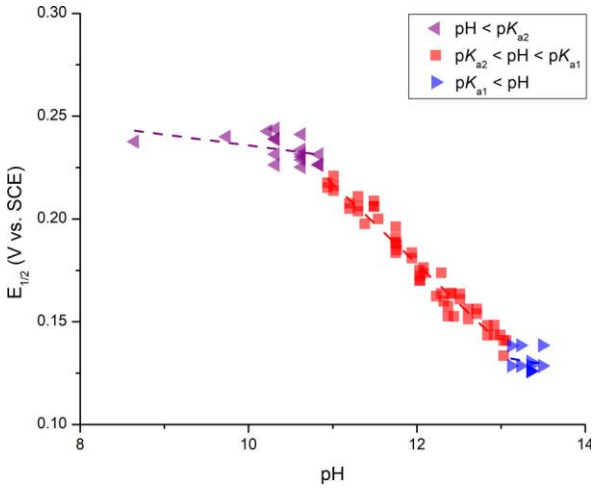

Figure 1.15: pH vs $E_{1/2}$ (V *vs* SCE) from points collected from titrating 1 M acetic acid and 1 M NaOH into 1,4-btmgb in aq. KCl (conc.) solution.

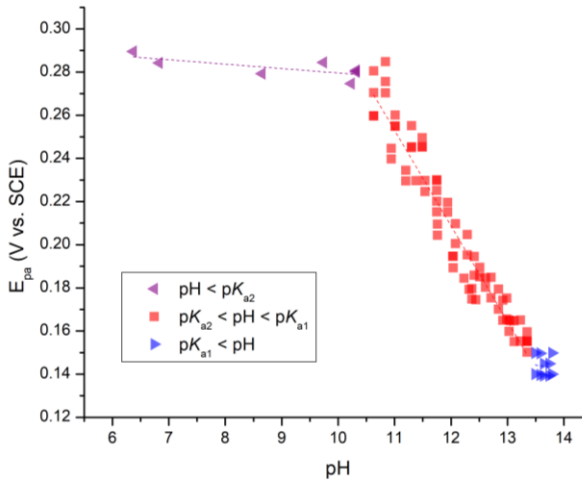

Figure 1.16: pH measurements *vs.* $E_{p,a}$ values from pH 13.79 to 2.52, taken from an initial solution of 1 mM btmgb dissolved in water with 100 mM KCl and titrated with 1 M NaOH and 1 M HCl or 1 M acetic acid. Collective data from varied scan rates of 200 mV, 400 mV, and 700 mV.

-tween the electrochemical potential and the solution pH with 1,4-btmgb was used to determine its pK_a values.[14–16] Cyclic voltammograms of 1,4-btmgb were acquired at pH values between 2.5 and 13.8. From these experiments, a partial Pourbaix diagram (**Figure 1.15**) was constructed by plotting the pH measured to the observed $E_{1/2}$ (or $E_{p,a}$ and $E_{p,c}$, **Figures 1.16–1.17**).[17] The reduction potential remained relatively constant below the pH value of 11. The oxidation potential shifted cathodically as the pH increased from 11 to 13.5 (**Figures 1.15–1.17**). The slope of the shift in $E_{1/2}$ versus pH was observed to be −40.4 mV/pH, indicating a two-electron, one-proton process.[17] Above pH 13.5, there were minimal changes in the redox potential. Further supporting this, with differential-pulse voltammetry (DPV) (**Figure 1.18**) experiments from pH 9.5 to 14.1, the exact breaking points in the pH-dependent and pH-independent regions allowed for the determination of pK_a values. Collectively, these data indicate a pK_{a1} value of approximately 13.5 ([1,4-btmgbH]$^+$) and a pK_{a2} value of 11.0 ([1,4-btmgbH$_2$]$_2^+$). The redox features of 1,4-btmgb are less reversible at

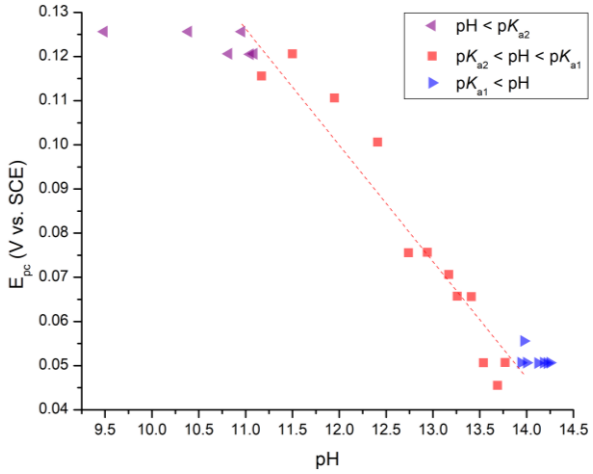

Figure 1.17: pH measurements *vs.* $E_{p,c}$ (from pairing CV with DPV experiments) from pH 14.12 to 9.49, taken from an initial solution of 2 mM btmgb dissolved in water with 200 mM KCl and titrated with 0.1 M, 1 M, or conc. NaOH and 0.1 M or 1 M HCl. CVs were taken with a scan rate of 500 mV/s.

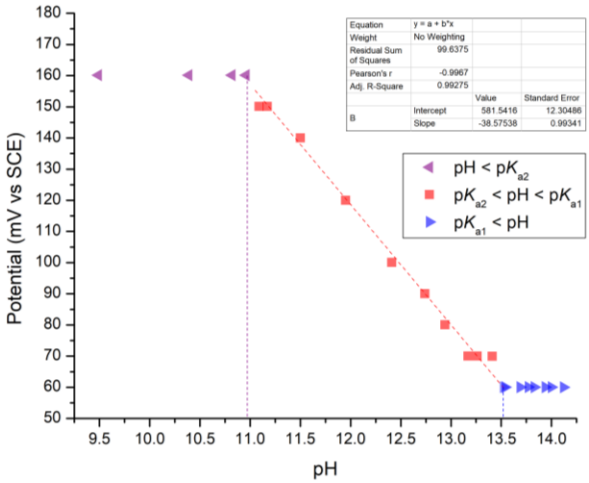

Figure 1.18: pH measurements *vs.* E_p, differential-pulse voltammetry (DPV) data from pH 14.12 to 9.49, taken from an initial solution of 2 mM btmgb dissolved in water with 200 mM KCl and titrated with 0.1 M, 1 M, or conc. NaOH and 0.1 M or 1 M HCl.

both higher and lower pH values. Between pH 11.3−11.9 there were two additional reduction peaks negative of the reversible redox event at $E_{1/2}$ = 0.2 V *vs* saturated calomel electrode (SCE) (pH = 11.75) (**Figure 1.11**, blue trace). The reduction event at 0.0 V is attributed to the reduction of [1,4-btmgbH]$^{3+}$, from the oxidized [1,4-btmgbH]$^{1+}$ that is expected to form at these pH values. The more cathodic reduction event at −0.18 V *vs* SCE increases in current at high pH (11.3 and higher, **Figure 1.11**, green trace) but was not observed when 1,4-btmgb was probed electrochemically in

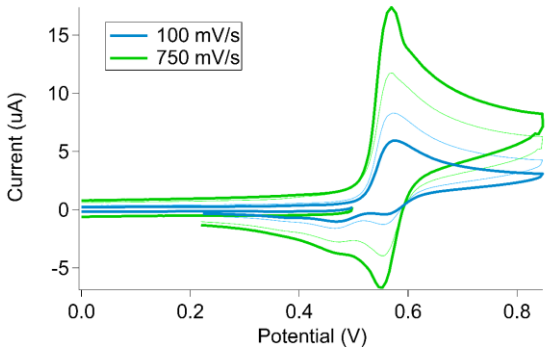

Figure 1.19: Cyclic voltammetry of 1 mM 1,4-btmgb in MeOH with 100 mM NaBr referenced *vs* Ag/Ag$^+$.

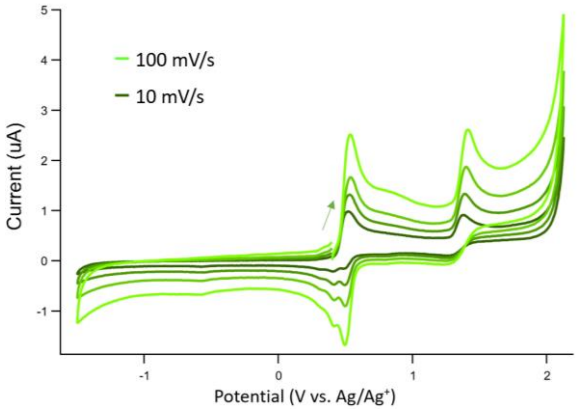

Figure 1.20: Cyclic voltammetry of 1mM 1,4-btmgb in EtOH with 100 mM $NaClO_4$ referenced *vs* Ag/Ag$^+$.

other nonaqueous protic solvents (methanol and ethanol, **Figures 1.19−1.20**). We attribute this reduction to an interaction with water upon oxidation, which is supported by electrolytic studies (*vide infra*).

1.2.5 Controlled Potential Electrolysis and Supporting Experiments

Electrochemically induced pH changes with 1,4-btmgb and [1,4-btmgbH$_2$][Cl]$_2$ were attempted through controlled potential oxidative electrolysis in a divided H-cell. 1,4-btmgb is sufficiently basic to deprotonate water. As a result, the initial pH of the solution was 11.71 (±0.06). Controlled potential electrolysis was carried out at 0.5 V *vs* SCE to fully oxidize the [1,4-btmgbH]$^{1+}$ to [1,4-btmgbH]$^{3+}$ and [1,4-btmgb]$^{2+}$. The final pH was observed to be 9.50 (±0.21).

An aqueous 2 mM solution of protonated [1,4-btmgbH$_2$][Cl]$_2$ was also oxidized. The initial pH was 9.88 and then decreased to 8.72. Upon subsequent reduction, the pH of the solution increased to 9.38 (**Table 1.1**). While both solutions produced a change in pH from electrolysis, the magnitudes were smaller than expected and the solutions could not be restored to the original pH after reduction. The solutions also turned deep red during oxidation, which is further explored in later UV-vis experiments. The color faded in intensity over time but did not completely disappear.

Table 1.1: pH values observed before and after electrolysis of 2 mM solutions of 1,4-btmgb and 1,4-btmgbH$_2^{2+}$[a]

Compound	Initial pH	Post oxidation pH	Post reduction pH
1,4-btmgb	11.71 (±0.06)	9.50 (±0.21)	10.50
1,4-btmgbH$_2^{2+}$	9.88	8.72	9.38

[a]Electrolysis performed stirred in a divided H-cell, with a carbon fabric working electrode and SCE reference electrode on the working side and a glassy carbon electrode on the counter side. Further details of the electrolysis in the methods.

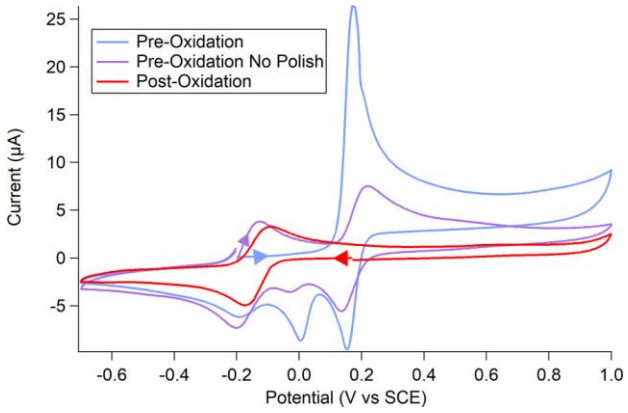

Figure 1.21: 2 mM 1,4-btmgb in 200 mM KCl and water, pre-oxidation scan rates 500 mV/s and post-oxidation scan rate 250 mV/s.

The CVs of the oxidized 1,4-btmgb solution are shown in **Figure 1.21** (red trace). Compared to the trace of the solution before oxidation, a new reductive event appears at −0.18 V *vs* SCE. This feature and the color change indicate the formation of new species after controlled potential oxidative electrolysis. The redox event at −0.18 V *vs* SCE we attribute to an aniline species that is the product of the decomposition of 1,4-btmgb via the loss of a TMG group via base-catalyzed hydrolysis (**Scheme 1.4**). This reduction feature is present only in CVs of 1,4-btmgb in water among the protic solvents surveyed, indicating it is related to the [1,4-btmgb^{2+}] generated in situ interacting with

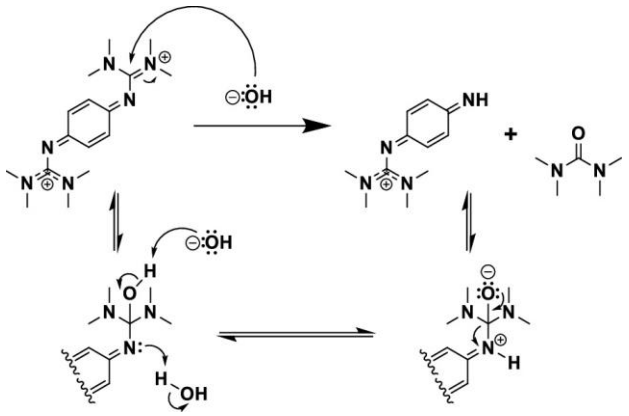

Scheme 1.4: Alkaline hydrolysis of a TMG group on oxidized 1,4 btmgb.

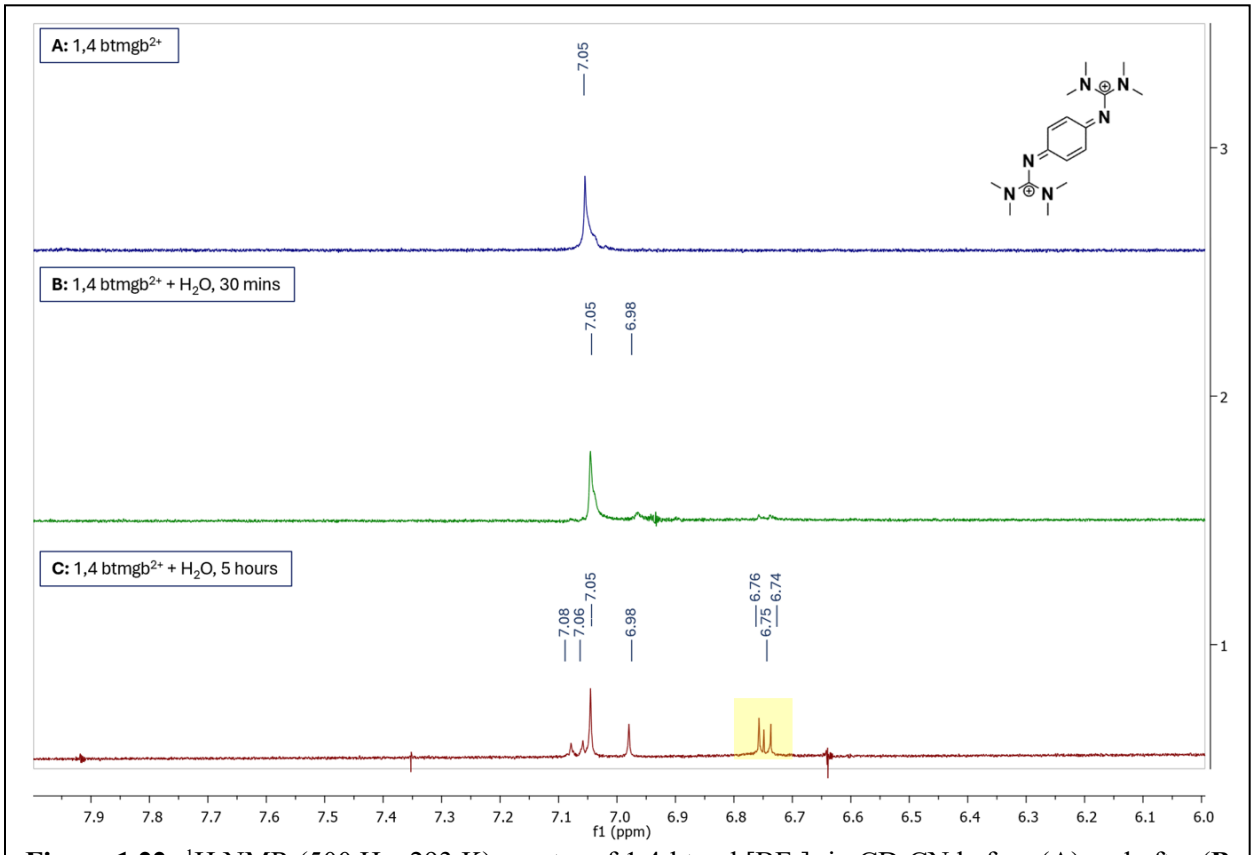

Figure 1.22: ^{1}H NMR (500 Hz, 293 K) spectra of 1,4-btmgb[BF_4]$_2$ in CD_3CN before (**A**) and after (**B** & **C**) water addition, aromatic region.

water/hydroxide. Prior studies have likened the redox behavior of the TMG substituted aniline to that of 1,4-bis(dimethylamino)-benzene where oxidation of this compound results in the Wurster cation and undergoes further decomposition in the solution mixture due to the N−H moiety.[18] There is literature precedence for this route of decomposition to form tetramethyl urea (**Scheme 1.4**).[19–21] ^{1}H NMR experiments were also performed on chemically oxidized [1,4-btmgb^{2+}] in deuterated acetonitrile in the presence of water, showing the decomposition of the parent species 30 minutes after the addition of water. Over the course of 5 hours, additional resonances at around 2.89 ppm and in the aromatic region (6.74−6.76 ppm) increase in intensity (**Figures 1.22–1.23**). The resonance at 2.86 ppm is assigned to the methyl proton peaks of tetramethyl urea, and the

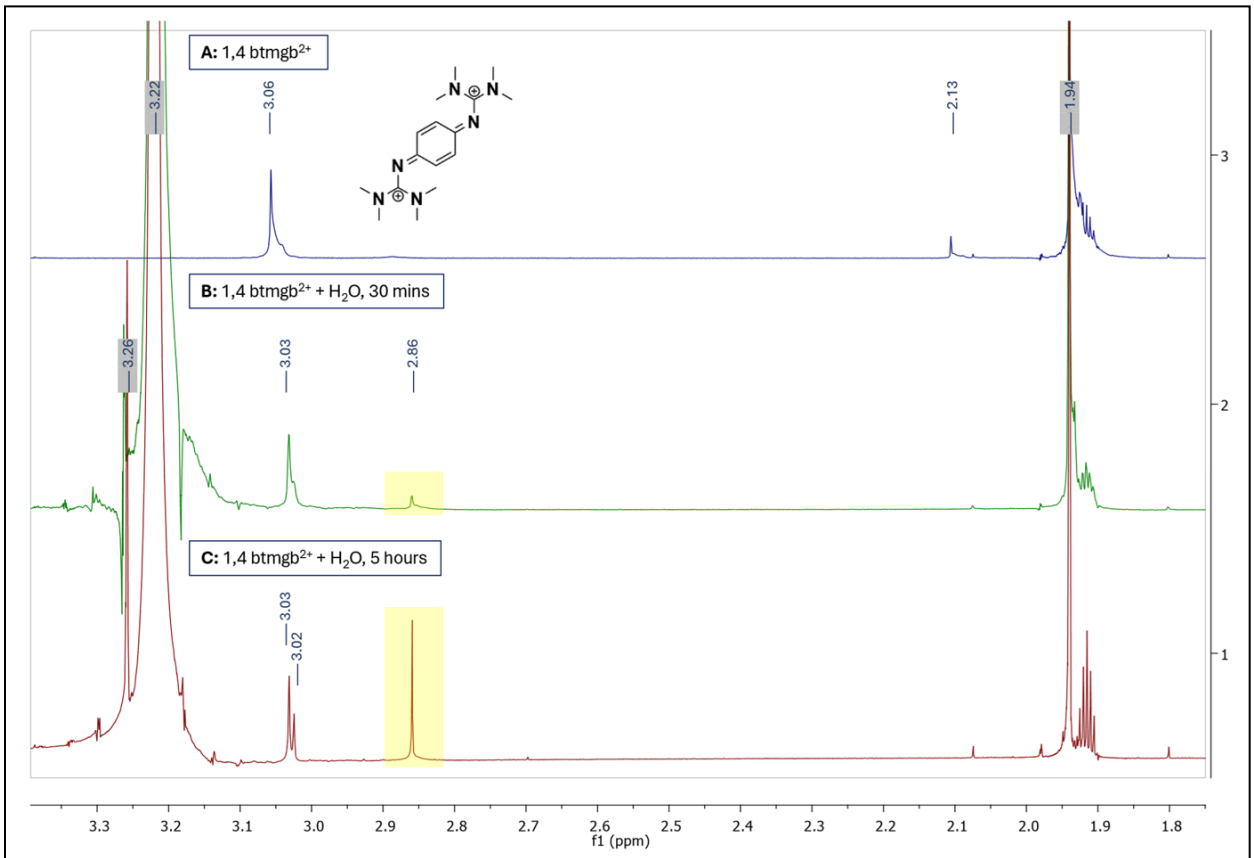

Figure 1.23: ^{1}H NMR (500 Hz, 293 K) spectra of the oxidized species 1,4-btmgb[BF_4]$_2$ in CD_3CN before (**A**) and after (**B** & **C**) water addition, methyl region. The high amounts of water added to this solution result in the residual water peak that is typically at 2.13 ppm (in CD_3CN) with respect to the solvent residual peak to shift downfield to 3.22 ppm due to H-bonding.

resonances between 6.74−6.76 ppm are attributed to the aniline species formed post-hydrolysis (tetramethylguanidino-dimethyl-*p*-phenylenediamine has aromatic resonances at 6.49−6.69 ppm while *p*-phenylenediamine has a resonance at 6.46 ppm in CD_3CN).[18] Altogether, the new resonance peaks in the aromatic region indicate decomposition in the presence of water. Monitoring the reduced species 1,4-btmgb in D_2O at high and low pH *via* ^1H NMR spectroscopy does not show evidence of decomposition over the span of days, indicating it is the oxidized species that is sensitive to deleterious reactions with water.

Further evidence for decomposition with hydroxide upon oxidation is observed in the scan-rate dependent CVs. A new reductive feature appears after oxidation of $[1,4\text{-btmgbH}]^{3+}$ and the $[1,4\text{-btmgb}]^{2+}$ species (**Figure 1.24**). This reduction event at −0.18 V *vs* SCE increases with scan rates 250 mV/s and above and slower for solutions over pH 11.5 (**Figures 1.12 & 1.24**). This reductive feature does not appear if the solution is not first oxidized. In addition to the hydrolysis decomposition pathway in **Scheme 1.4**, we attribute the color change observed during electrolysis to a second decomposition pathway that results in radical formation. Prior studies in

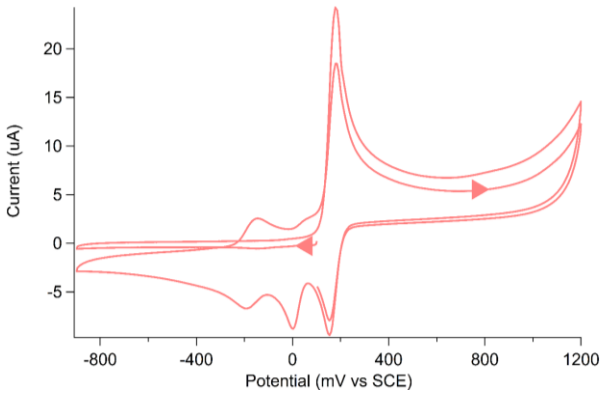

Figure 1.24: Cyclic voltammetry investigating the reduction events at 0 and -0.18 V vs. SCE of 1,4-btmgbH$^+$ in water by scanning reductively first before scanning again after the main redox peak at 0.2 V vs SCE (1,4-btmgb/btmgb^{2+}). 1 mM 1,4-btmgb in water with 100 mM KCl at 250 mV/s, at pH 11.72.

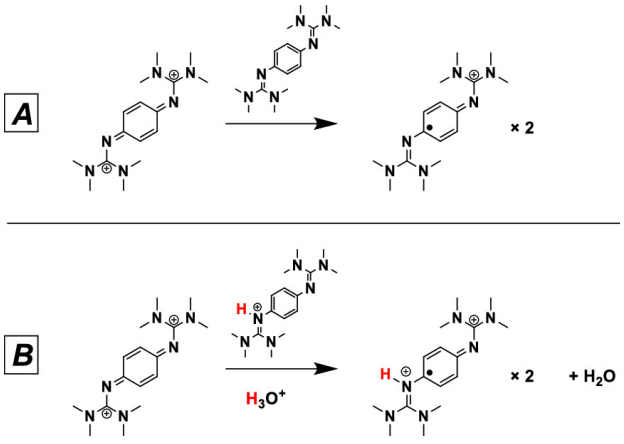

Scheme 1.5: Various Proposed Comproportionation Pathways for $[1,4\text{-btmgb}]^{2+}$ (**A**) Unprotonated and (**B**) between a Reduced Monoprotonated Species $[1,4\text{-btmgbH}]^+$.

acetonitrile conditions have shown that the fully oxidized $[1,4\text{-btmgb}]^{2+}$ can comproportionate with 1,4-btmgb to form $[1,4\text{-btmgb}\cdot]^{1+}$ in solution (**Scheme 1.5**).[22] Water is also known to stabilize this radical formation.[23] To verify the presence of a radical in the solution, electron paramagnetic resonance (EPR) spectra were acquired by using aliquots of the oxidized 2 mM 1,4-btmgb. An EPR signal at $g_{\perp}$ = 2.0066 was present for the solution after controlled potential electrolysis at 0.5 V for 10 min, indicating the formation of an S = 1/2 organic radical species (**Figure 1.25**). Ultraviolet−visible (UV−vis) spectroelectrochemistry (SEC) was used to obtain absorption spectra of the generated oxidized species $[1,4\text{-btmgb}]^{2+}$ (**Figure 1.26**) through controlled potential electrolysis of a 0.1 mM solution of 1,4-btmgb with 100 mM KCl in water at 0.25 V *vs* SCE. $1,4\text{-btmgbH}^{+}$ has absorbances of 235 and 272 nm. Oxidation leads to two new absorbances at 224 and 291 nm, which have higher absorbance. The post-electrolysis solution obtained after oxidation in an H-cell with stirring leads to different absorption spectra than what was observed in the UV−vis SEC experiments (**Figure 1.27**). The absorbances that

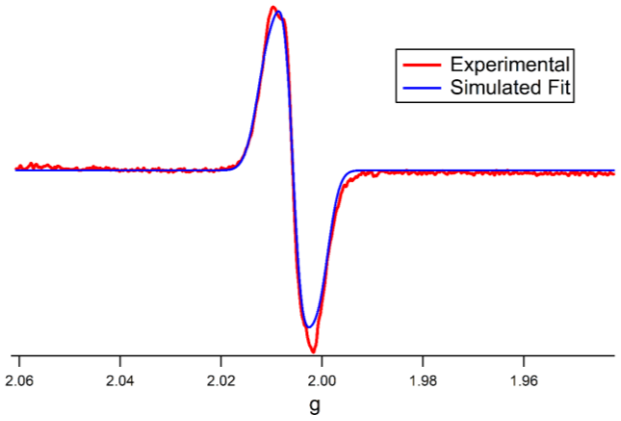

Figure 1.25: EPR spectrum of 2 mM 1,4-btmgb oxidized for 10 mins, measured at 77 K, microwave frequency = 9.43 GHz.

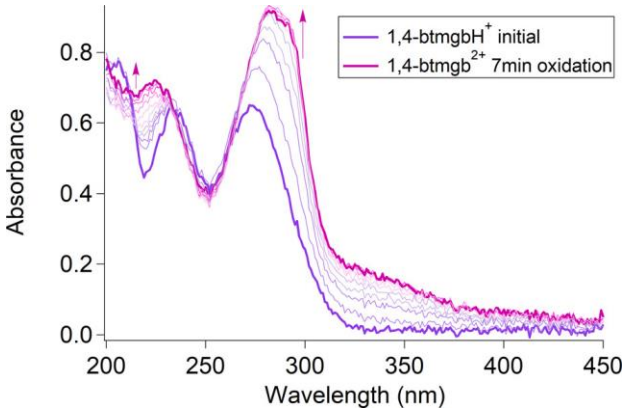

Figure 1.26: UV–visible SEC data of 0.1 mM 1,4-btmgb. Oxidation at 500 mV *vs* Ag^{+}/Ag electrode in unbuffered water with KCl (100 mM) was performed at pH 11.91. Under these conditions, it is expected to protonate once to give $1,4\text{-btmgbH}^{+}$. Purple trace is initial $1,4\text{-btmgbH}^{+}$ and pink trace is oxidized $1,4\text{-btmgb}^{2+}$ at 250 mV vs SCE.

correspond to the oxidized species were not present. We believe that convection increases the rate of comproportionation. After 1 day, the absorbance at 272 nm also decreases in intensity, indicating decomposition. The solubility of 1,4-btmgb was measured in water in the absence and presence of CO_2. Unlike MeCN, it was found that the addition of CO_2 does not diminish the solubility of 1,4-btmgb in water or lead to precipitation, even in saturated solutions. The determined solubility of 1,4-btmgb in water is 97 g/L (0.32 M). Collectively, these decomposition pathways result in smaller than expected pH changes in the controlled potential electrolysis experiments (**Table 1.1**). Additionally, the side reactions hinder the regeneration of 1,4-btmgb and the overall reversibility of an electrochemical cycle.

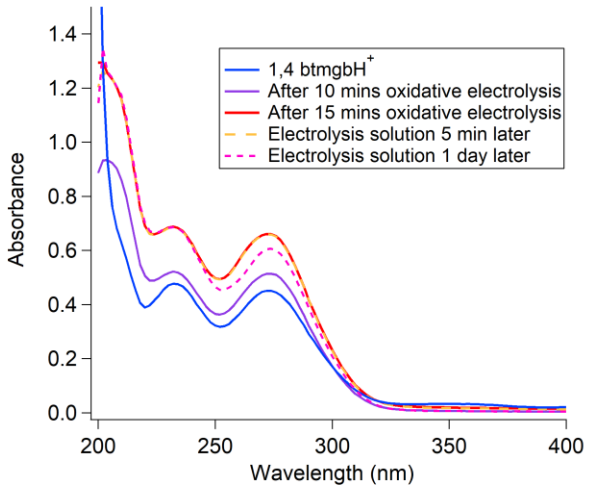

Figure 1.27: UV-Vis spectra before and after controlled oxidative electrolysis of 1 mM 1,4 btmgbH$^+$ in water with 100 mM KCl. Oxidation held at 0.5 V vs. SCE. Sample diluted for UV-Vis measurement.

1.3 Conclusions

A guanidine-functionalized aromatic (GFA) compound, 1,4-btmgb, was examined as a redox-active candidate for CO_2 capture. Reactivity with CO_2 in the presence of trace water forms protonated guanidine and carbonate. In addition, the stability of 1,4-btmgb and the preliminary redox behavior in water indicate that it could potentially mediate a pH swing cycle. The aqueous pK_a values of [1,4-btmgbH$_2$]$^{2+}$ were measured to be 11.0 and 13.5. However, controlled potential electrolysis indicates more complicated reactivity in water with hydrolysis and radical formation

decomposition pathways. The use of GFAs in electrochemical CO_2 capture and concentration will require addressing these decomposition pathways.

1.4 Experimental

General Methods: Synthetic work was carried out in either ambient air or under a dinitrogen (N_2) atmosphere in a glovebox where noted. All solvents and reagents were purchased from commercial vendors and used without further purification unless otherwise noted. Deuterated acetonitrile used for NMR characterization were purchased from Cambridge Isotope Laboratories, Inc., and were degassed via free−pump−thaw and stored over activated 3 Å molecular sieves. Tetrabutylammonium hexafluorophosphate ($TBAPF_6$) was purified via recrystallization from ethanol and dried under a heated (80 °C) vacuum (1×10^{-3} Torr) and stored in a glovebox. Experiments using carbon dioxide (CO_2) atmospheres were performed using ultrahigh purity (99.999%) CO_2, which was additionally passed through a purification column to eliminate residual H_2O, O_2, CO, halocarbons, and sulfur compounds.

Electrochemical Methods: Electrochemical experiments were carried out under an atmosphere of N_2 or CO_2, where indicated. Solutions for electrochemical measurements were recorded in acetonitrile or water using 100 mM $TBAPF_6$ (or $TMAPF_6$) or 100 mM KCl as the supporting electrolytes, respectively. Cyclic voltammetry (CV) was performed with a Pine instrument WaveDriver 10 potentiostat. In organic solvents, ferrocene ($Fe(C_5H_5)_2$) was used as an internal standard and potentials are referenced to the ferrocenium/ferrocene ($Fe(C_5H_5)_2^{+/0}$) couple. In water, a saturated calomel electrode (SCE) or a Ag/AgCl electrode was used as the internal reference electrode. Between CV scan, the working electrode was polished in a figure eight pattern with an alumina slurry (0.05 um) on a microcloth (2.875 in, PSA backed). Controlled potential electrolysis experiments were performed stirred in a custom H-cell with the working and the counter cells

divided by a porous glass frit. In the working compartment, carbon fabric was used as the working electrode and SCE as the reference. A glassy carbon rod was used as the counter electrode on the counter side cell. UV−visible spectroelectrochemistry (UV−vis SEC) was performed using a UV−vis SEC kit from Pine Instruments with a Pt working/counter electrode and Ag wire as a pseudo reference electrode.

Physical Methods: UV−vis absorption spectra were recorded by using a 1 cm quartz cuvette with an Agilent Cary 60 UV−vis spectrophotometer. CO_2 monitoring was performed on a CM-0111 gas sensor kit CM-0111 by CO_2Meter with the software GasLab. A Bruker EMX spectrometer equipped with an ER041XG microwave bridge was used to collect the X-band EPR spectra. Fourier Transform Infrared (FTIR) spectra were collected by using a Thermo Scientific Nicolet iS5 FTIR Spectrometer with iD5 diamond ATR. ^{1}H, $^{13}C\{^{1}H\}$, and $^{19}F\{^{1}H\}$ NMR spectra were recorded with a 500 MHz Bruker or 600 MHz Varian instruments. ^{1}H NMR spectra chemical shifts were reported as δ values in ppm relative to the residual solvent: D_2O (4.79 ppm), MeOD (3.31 ppm), and CD_3CN (1.94 ppm). pH values were collected with a Thermo Scientific Orion Star A216 pH/RDO/DO meter. The instrument was calibrated with Thermo Scientific buffers at pH 4.01, 7.00, and 10.01 each time before use.

X-ray diffraction studies were conducted at the UCI Department of Chemistry X-ray Crystallography Facility on a Bruker SMART APEX II or Bruker X8 Prospector diffractometer. Crystals were mounted in a cryoloop and transferred to a Bruker X8 Prospector (SMART APEX II, Mo Kα, λ = 0.71073 Å) or Bruker X8 Prospector (Cu Kα, λ = 1.5406 Å) diffractometer system.

1,4-Bis(tetramethylguanidino)benzene. Synthesized following previously described prep by Himmel and co-workers.[10] ^{1}H NMR (600 MHz, CD_3OD) δ = 6.63 (s, 4H) 2.72 (br, 24H)

ppm. ^{1}H NMR (600 MHz, D_2O, unbuffered) δ = 6.85 (s, 4H), 2.82 (s, 24H) ppm. $^{13}C\{^{1}H\}$ (151 MHz, D_2O, unbuffered) δ = 161.2, 139.9, 122.5, 39.19 ppm.

1,4-btmgb[BF_4]$_2$. Synthesized following previously described prep by Himmel and co-workers, but using Ag[BF_4] instead of Ag[PF_6].[10] Use in water decomposition experiments in CD_3CN as seen in **Figures 1.22–1.23**.

1,4-btmgbH_2[PF_6]$_2$. In a glovebox, a mixture of 1,4-btmgb (0.018 g, 0.060 mmol) and [NH_4][PF_6] (0.016 g, 0.1 mmol) in dry MeCN (20 mL) was stirred for 45 min while heated at 55 °C. The solvent was removed under reduced pressure, and the resulting solid was redissolved in MeCN, yielding a clear yellow solution. Activated carbon was added, and the solution was left to stir for 15 min before being filtered through glass fiber. Removal of the solvent yielded a white powder that, when recrystallized from Et_2O, formed clear crystals. Yield: 14 mg (41%). ^{1}H NMR (600 MHz, CD_3CN) δ = 7.93 (s, 2H), 7.04 (s, 4H), 2.92 (s, 24H) ppm. (600 MHz, D_2O) δ = 7.11 (s, 4H), 2.97 (s, 24H) $^{13}C\{^{1}H\}$ NMR (151 MHz, CD_3CN) δ = 159.3, 135.6, 123.3, 40.8 ppm. $^{13}C\{^{1}H\}$ (151 MHz, D_2O) δ = 158.6, 134.9, 122.3, 39.6 ppm. UV/vis (CH_3CN): λmax (ε in L·(mol cm)$^{-1}$) = 277 (4.0 × 104), 231 (2.2 × 104) nm. FTIR (ATR)/cm^{-1} ν = 3400 (w), 3328 (w), 2926 (w), 1627 (m), 1563 (w), 1520 (w), 1466 (w), 1420 (m), 1316 (w), 1230 (w), 1165 (w), 1067 (w), 1041 (w), 917 (w), 822 (s), 741 (m), 557 (m). MS (ESI-MS) *m*/*z* calcd $C_{16}H_{29}N_6^+$ [M-H-2(PF_6)]$^+$ 305.25, found *m*/*z* 305.25. (Low-res MS) found *m*/*z* [M-PF_6]$^+$ 451.3, [M-H-2(PF_6)]$^+$ 305.3, and [M/2]2+ 153.2.

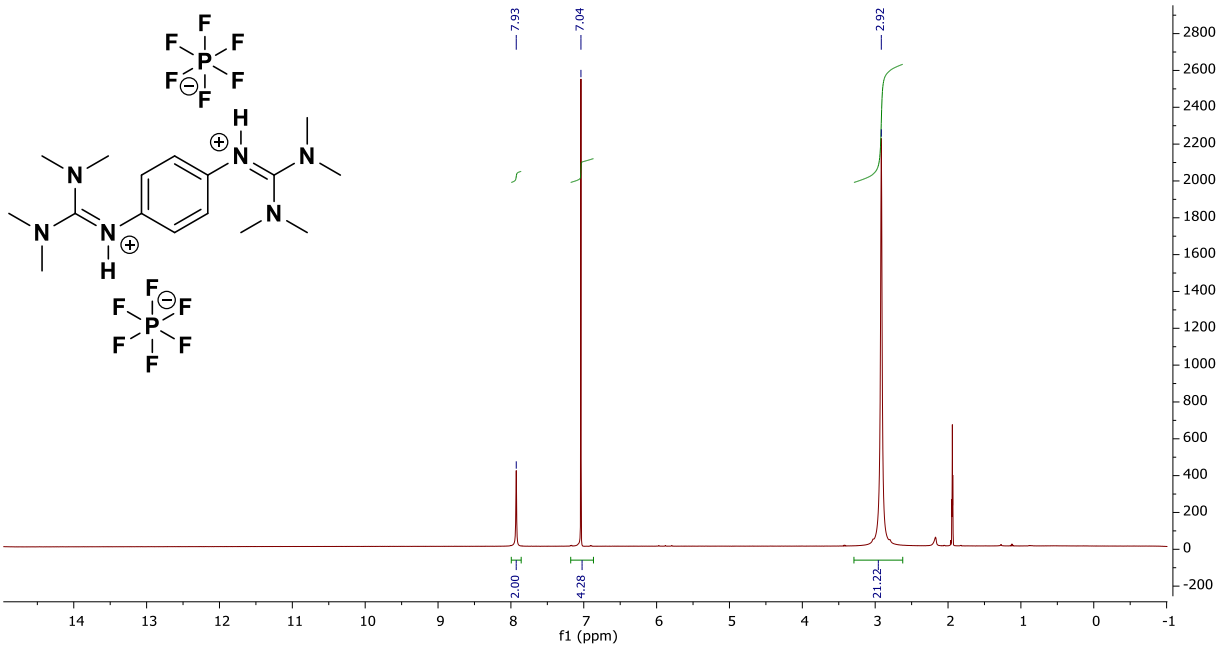

Figure 1.28: ^{1}H NMR of 1,4 btmgb$H_2[PF_6]_2$ in CD_3CN, 600 Hz, 293 K.

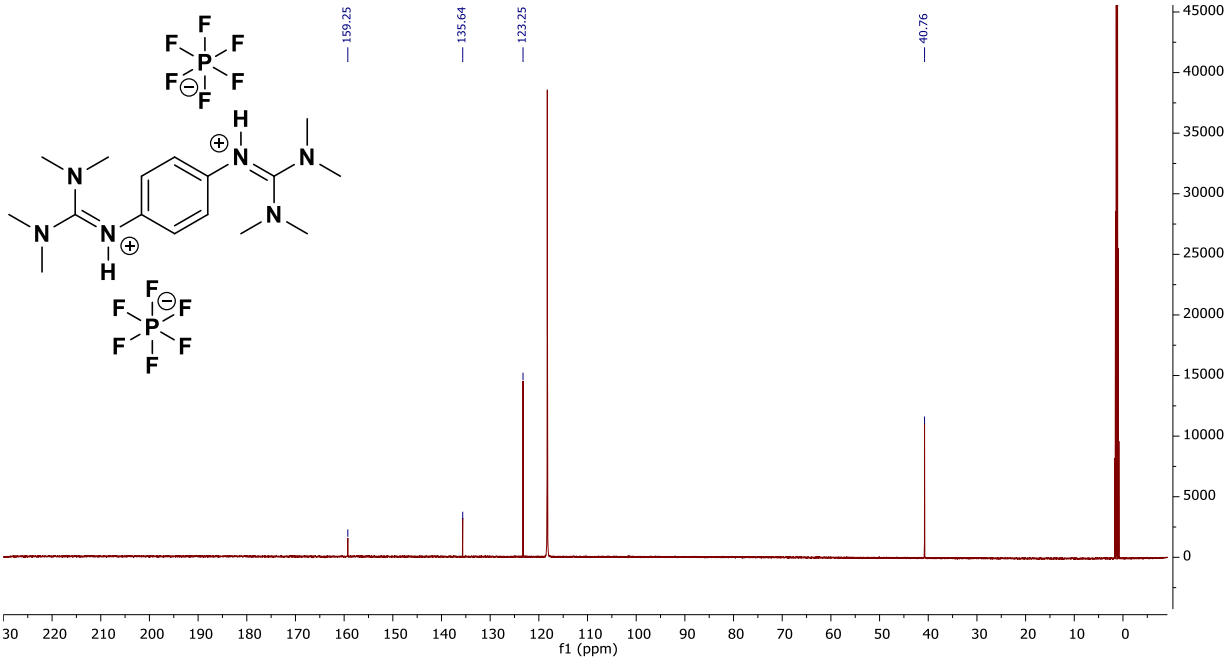

Figure 1.29. $^{13}C\{^{1}H\}$ NMR of 1,4 btmgb$H_2[PF_6]_2$ in CD_3CN, 600 Hz, 293 K.

1,4-btmgbH$_2$[CO$_3$H]$_2$. Preparation varied, but for the general isolation of the compound, the procedure for characterization and experiments is as follows. A solution of 1,4-btmgb (10 mg) in MeCN (5 mL) was sparged with CO_2 for 3 min for CO_2 saturation at room temperature. While the solution was still actively sparged by CO_2, deionized water (0.1 mL) was added to the solution and a cloudy precipitate was observed to form. The solution was dried under a vacuum, yielding a chalky white power. Yield: quantitative. Crystals suitable for X-ray diffraction were grown from dissolved 1,4-btmgb in MeCN and drops of water, under a headspace of CO_2. ^{1}H NMR (600 MHz, CD_3OD) δ = 6.94 (s, 4H), 2.90 (s, 24H) ppm. ^{1}H NMR (600 MHz, D_2O) δ = 7.11 (s, 4H), 2.97 (s, 24H) ppm. ^{13}C{^{1}H} NMR (151 MHz, D_2O) δ: 160.3, 158.6, 134.9, 124.8, 122.3, 39.6 ppm. FTIR (ATR)/cm^{-1} v = 3380 (w), 3010 (w), 2917 (w), 2876 (w), 2802 (w), 2161 (w), 1564 (s), 1461 (s), 1437 (m), 1372 (s), 1268 (m), 1230 (m), 1204 (m), 1132 (s), 1097 (m), 1062 (w), 1016 (s), 922 (w), 841 (s), 751 (m), 685 (m), 638 (w), 578 (w). MS (ESI-MS) *m*/*z* calcd $C_{16}H_{29}N_6^+$ [M-H-2(CO_3H)]$^+$ 305.25, found *m*/*z* 305.25. (low-res MS) found *m*/*z* [M-H-2(CO_3H)]$^+$ 305.3, [M/2]$^{2+}$ 153.2. **For the corresponding spectra, see the lower panel of Figures 1.8–1.9.**

1,4-btmgbH[BF$_4$]. In a glovebox, a mixture of 1,4-btmgb (0.021 g, 0.070 mmol) and [NHBu$_3$][BF$_4$] (0.019 g, 0.070 mmol) in dry MeCN (20 mL) was stirred for 1 h at 55 °C. The solvent was removed under reduced pressure, and the resulting beige solid was recrystallized from MeCN and Et_2O. Yield: 10 mg (50%). ^{1}H NMR (600 MHz, CD_3CN) δ = 7.79 (s, 1H), 6.73 (s, 4H), and 2.76 (s, 24H) ppm. ^{13}C{^{1}H} NMR (151 MHz, CD_3CN) δ = 159.1, 123.1, 122.3, 115.0, 39.4 ppm. ^{19}F{^{1}H} NMR (565 MHz, CD_3CN) δ = 151.8 ppm. FTIR (ATR)/cm^{-1} ν = 3382 (w), 3340 (w), 2932 (w), 2887 (w), 2361 (w), 2163 (w), 1630 (m), 1551 (m), 1493 (m), 1383 (m), 1318 (w), 1231 (w), 1205 (w), 1144 (w), 1049 (s), 1019 (s), 914 (w), 855 (m), 843 (m), 764 (w), 616 (w), 579 (w). MS (ESI-MS) *m*/*z* calcd $C_{16}H_{29}N_6^+$ [MBF_4]$^+$ 305.25, found *m*/*z* 305.25.

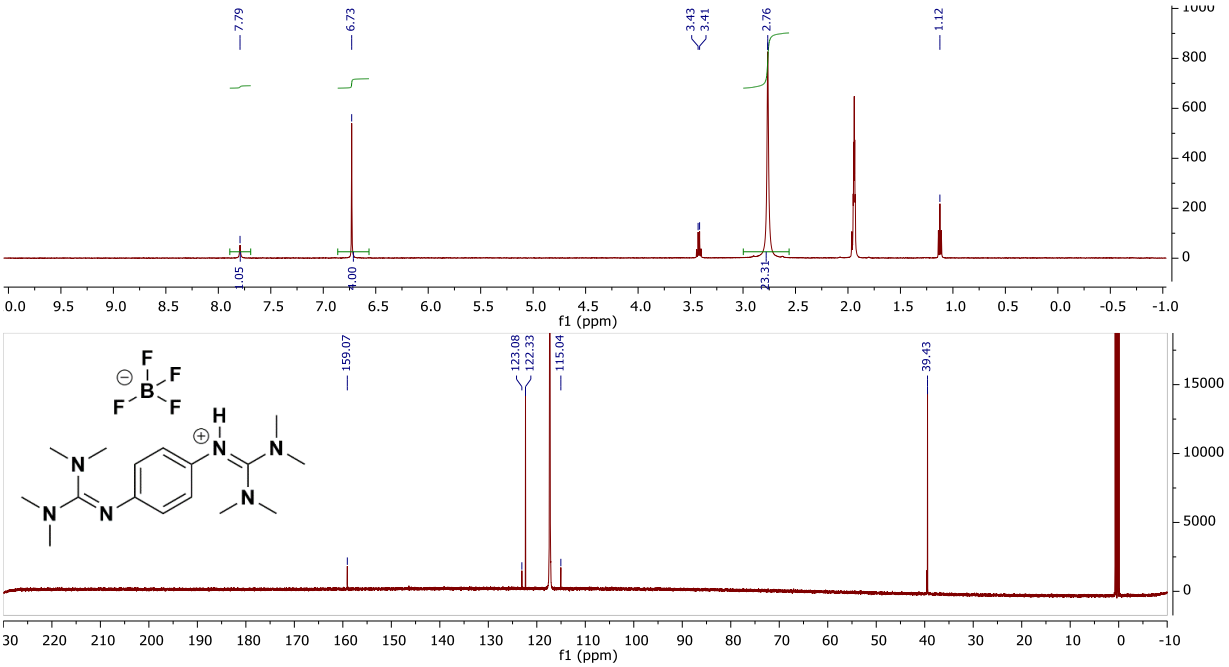

Figure 1.30:. ^{1}H (500 Hz) and $^{13}C\{^{1}H\}$ (151 Hz) NMR **of 1,4 btmgbH[BF_4]** in CD_3CN, 293 K.

1.5 Crystallographic Information

Crystallographic Information for 1,4-btmgbH$_2$[PF$_6$]$_2$

A colorless crystal of approximate dimensions 0.124 x 0.283 x 0.305 mm was mounted on a glass fiber and transferred to a Bruker SMART APEX II diffractometer system. The APEX2[24] program package was used to determine the unit-cell parameters and for data collection (10 sec/frame scan time). The raw frame data was processed using SAINT[25] and SADABS[26] to yield the reflection data file. Subsequent calculations were carried out using the SHELXTL[27] program package. The diffraction symmetry was *2/m* and the systematic absences were consistent with the monoclinic space group $P2_1/c$ that was later determined to be correct.

Refinement Details

The structure was solved by direct methods and refined on F^2 by full-matrix least-squares techniques. The analytical scattering factors[28] for neutral atoms were used throughout the analysis. Hydrogen atoms were located from a difference-Fourier map and refined (x,y,z and U_{iso}). The molecule was located about an inversion center.

Least-squares analysis yielded wR2 = 0.0805 and Goof = 1.025 for 223 variables refined against 3703 data (0.69 Å), R1 = 0.0311 for those 3137 data with $I > 2.0\sigma(I)$.

Crystallographic Information for 1,4-btmgbH[PF_6]

A colorless crystal of approximate dimensions 0.121 x 0.124 x 0.154 mm was mounted in a cryoloop and transferred to a Bruker X8 Prospector diffractometer system. The APEX3[29] program package was used to determine the unit-cell parameters and for data collection (30 sec/frame scan time). The raw frame data was processed using SAINT[25] and SADABS[26] to yield the reflection data file. Subsequent calculations were carried out using the SHELXTL[27] program package. The diffraction symmetry was 2/*m* and the systematic absences were consistent with the monoclinic space group $P2_1/c$ that was later determined to be correct.

Refinement Details

The structure was solved by direct methods and refined on F^2 by full-matrix least-squares techniques. The analytical scattering factors[28] for neutral atoms were used throughout the analysis.

Hydrogen atom H(1) was located from a difference-Fourier map and refined (x,y,z and U_{iso}). The remaining hydrogen atoms were included using a riding model.

Least-squares analysis yielded wR2 = 0.1132 and Goof = 1.027 for 274 variables refined against 3814 data (0.825 Å), R1 = 0.0386 for those 3054 data with I > 2.0σ(I).

Crystallographic Information for 1,4-btmgbH$_2$(HCO$_3^-$)$_2$

A colorless crystal of approximate dimensions 0.082 x 0.201 x 0.228 mm was mounted in a cryoloop and transferred to a Bruker SMART APEX II diffractometer system. The APEX2[24] program package was used to determine the unit-cell parameters and for data collection (90 sec/frame scan time). The raw frame data was processed using SAINT[25] and SADABS[26] to yield the reflection data file. Subsequent calculations were carried out using the SHELXTL[27] program package. The diffraction symmetry was 2/*m* and the systematic absences were consistent with the monoclinic space group $P2_1/n$ that was later determined to be correct.

Refinement Details

The structure was solved by direct methods and refined on F^2 by full-matrix least-squares techniques. The analytical scattering factors[28] for neutral atoms were used throughout the analysis. Hydrogen atoms were located from a difference-Fourier map and refined (x,y,z and U_{iso}). The molecule was located about an inversion center. There were two molecules of bicarbonate anion present.

Least-squares analysis yielded wR2 = 0.1008 and Goof = 1.046 for 200 variables refined against 3242 data (0.70 Å), R1 = 0.0402 for those 2503 data with I > 2.0σ(I).

Crystallographic Information for 1,4-btmgbH$_2$(HCO$_3^-$)$_2$·(H$_2$O)$_2$

A colorless crystal of approximate dimensions 0.097 x 0.139 x 0.192 mm was mounted in a cryoloop and transferred to a Bruker X8 Prospector diffractometer system. The APEX3[29] program

package was used to determine the unit-cell parameters and for data collection (2 sec/frame scan time). The raw frame data was processed using SAINT[25] and SADABS[26] to yield the reflection data file. Subsequent calculations were carried out using the SHELXTL[27] program package. There were no systematic absences nor any diffraction symmetry other than the Friedel condition. The centrosymmetric triclinic space group *P*-1 was assigned and later determined to be correct.

Refinement Details

The structure was solved by direct methods and refined on F^2 by full-matrix least-squares techniques. The analytical scattering factors[28] for neutral atoms were used throughout the analysis. Hydrogen atoms were located from a difference-Fourier map and refined (x,y,z and U_{iso}). The molecule was located about an inversion center. There were two molecules of water present.

Least-squares analysis yielded wR2 = 0.0874 and Goof = 1.094 for 218 variables refined against 2089 data (0.83 Å), R1 = 0.0321 for those 1871 data with $I > 2.0\sigma(I)$.

Table 1.2: Compiled Crystallographic Data

	1,4-btmgbH₂ [PF₆]₂	***1,4-btmgbH [PF₆]***	***1,4-btmgbH₂ (HCO₃⁻)₂***	***1,4-btmgbH₂ (HCO₃⁻)₂·(H₂O)₂***
Empirical formula	$[C_{16}\ H_{30}\ N_6]\ [F_6\ P]_2$	$[C_{16}\ H_{29}\ N_6]\ [PF_6]$	$[C_{16}\ H_{30}\ N_6]$ $[C\ H\ O_3]_2$	$[C_{16}\ H_{30}\ N_6]$ $[C\ H\ O_3]_2\ (H_2\ O)_2$
Formula weight	596.40	450.42	428.49	464.53
Temperature [K]	133(2) K	93(2)	93(2) K	92(2) K
Wavelength	0.71073 Å	1.54178	0.71073 Å	1.54178
Crystal system	Monoclinic	Monoclinic	Monoclinic	Triclinic
Space group (number)	$P2_1/c$	$P2_1/c$	$P2_1/n$	P-1
a [Å]	10.7063(5)	13.5006(10)	9.7836(14)	7.9540(9)
b [Å]	8.9270(4)	11.7654(9)	8.1140(12)	9.1652(11)
c [Å]	12.8565(6)	14.5989(11)	13.4892(19)	9.2032(11)
α [°]	90	90	90	87.747(6)
β [°]	99.4282(8)	116.210(4)	96.738(2)	66.175(5)
γ [°]	90	90	90	69.028(5)
Volume [Å³]	1212.16(10)	2080.5(3)	1063.4(3)	568.71(12)
Z	2	4	2	1
ρ_{calc} *[Mg cm⁻³]*	1.634	1.438	1.338	1.356
μ *[mm⁻¹]*	0.290	1.800	0.101	0.899
F (000)	612	944	460	250
Crystal size [mm³]	0.305 x 0.283 x 0.124	0.154 x 0.127 x 0.118	0.228 x 0.201 x 0.082	0.192 x 0.139 x 0.097
Crystal color	colorless	colorless	colorless	colorless
2θ range [°]	1.928 to 30.990	3.649 to 69.128	2.441 to 30.544	5.208 to 68.832
Index ranges	$-15 \le h \le 15, -12 \le k \le 12, -18 \le l \le 18$	$-15 \le h \le 16, -14 \le k \le 14, -17 \le l \le 17$	$-13 \le h \le 13, -11 \le k \le 11, -19 \le l \le 19$	$-9 \le h \le 9, -11 \le k \le 11, -11 \le l \le 11$
Reflections collected	29110	35044	25041	28347
Independent reflections	3703 [R(int) = 0.0338]	3814 [R(int) = 0.0617]	3242 [R(int) = 0.0527]	2089 [R(int) = 0.0475]
Completeness to θ = 25.242°	100.0%	98.7%	100.0%	99.6%
Data / Restraints / Parameters	3703 / 0 / 223	3814 / 0 / 274	3242 / 0 / 200	2089 / 0 / 218
Goodness-of-fit on F²	1.025	1.027	1.046	1.094
Final R indexes [I≥2σ(I)]	R1 = 0.0311, wR2 = 0.0760	R1 = 0.0386, wR2 = 0.1037	R1 = 0.0402, wR2 = 0.0916	R1 = 0.0321, wR2 = 0.0847
Final R indexes [all data]	R1 = 0.0396, wR2 = 0.0805	R1 = 0.0504, wR2 = 0.1132	R1 = 0.0614, wR2 = 0.1008	R1 = 0.0358, wR2 = 0.0874
Largest peak/hole [eÅ⁻³]	0.426 and -0.336	0.258 and -0.381	0.353 and -0.213	0.244 and -0.202

1.6 References

(1) Barlow, J. M.; Clarke, L. E.; Zhang, Z.; Bím, D.; Ripley, K. M.; Zito, A.; Brushett, F. R.; Alexandrova, A. N.; Yang, J. Y. Molecular Design of Redox Carriers for Electrochemical CO_2 Capture and Concentration. *Chem. Soc. Rev.* **2022**, *51* (20), 8415–8433. https://doi.org/10.1039/D2CS00367H.

(2) Rheinhardt, J. H.; Singh, P.; Tarakeshwar, P.; Buttry, D. A. Electrochemical Capture and Release of Carbon Dioxide. *ACS Energy Lett.* **2017**, *2* (2), 454–461. https://doi.org/10.1021/acsenergylett.6b00608.

(3) Jin, S.; Wu, M.; Gordon, R. G.; Aziz, M. J.; Kwabi, D. G. pH Swing Cycle for CO_2 Capture Electrochemically Driven through Proton-Coupled Electron Transfer. *Energy Environ. Sci.* **2020**, *13* (10), 3706–3722. https://doi.org/10.1039/D0EE01834A.

(4) Puleo, T. R.; Sujansky, S. J.; Wright, S. E.; Bandar, J. S. Organic Superbases in Recent Synthetic Methodology Research. *Chem. – Eur. J.* **2021**, *27* (13), 4216–4229. https://doi.org/10.1002/chem.202003580.

(5) Pereira, F. S.; deAzevedo, E. R.; da Silva, E. F.; Bonagamba, T. J.; da Silva Agostíni, D. L.; Magalhães, A.; Job, A. E.; Pérez González, E. R. Study of the Carbon Dioxide Chemical Fixation—Activation by Guanidines. *Tetrahedron* **2008**, *64* (43), 10097–10106. https://doi.org/10.1016/j.tet.2008.08.008.

(6) Heldebrant, D. J.; Yonker, C. R.; Jessop, P. G.; Phan, L. Organic Liquid CO_2 Capture Agents with High Gravimetric CO2 Capacity. *Energy Environ. Sci.* **2008**, *1* (4), 487–493. https://doi.org/10.1039/B809533G.

(7) Seipp, C. A.; Williams, N. J.; Kidder, M. K.; Custelcean, R. CO_2 Capture from Ambient Air by Crystallization with a Guanidine Sorbent. *Angew. Chem. Int. Ed.* **2017**, *56* (4), 1042–1045. https://doi.org/10.1002/anie.201610916.

(8) Custelcean, R.; Williams, N. J.; Garrabrant, K. A.; Agullo, P.; Brethomé, F. M.; Martin, H. J.; Kidder, M. K. Direct Air Capture of CO_2 with Aqueous Amino Acids and Solid Bis-Iminoguanidines (BIGs). *Ind. Eng. Chem. Res.* **2019**, *58* (51), 23338–23346. https://doi.org/10.1021/acs.iecr.9b04800.

(9) Kasturi, A.; Gabitto, J.; Tsouris, C.; Custelcean, R. Carbon Dioxide Capture with Aqueous Amino Acids: Mechanistic Study of Amino Acid Regeneration by Guanidine Crystallization and Process Intensification. *Sep. Purif. Technol.* **2021**, *271*, 118839. https://doi.org/10.1016/j.seppur.2021.118839.

(10) Hornung, J.; Hübner, O.; Kaifer, E.; Himmel, H.-J. Bent and Twisted: The Electronic Structure of 2-Azapropenylium Ions Obtained by Guanidine Oxidation. *RSC Adv.* **2016**, *6* (45), 39323–39329. https://doi.org/10.1039/C6RA04494H.

(11) Leffek, K. T.; Pruszynski, P.; Thanapaalasingham, K. Basicity of Substituted 2-Phenyl-1,1,3,3- Tetramethylguanidines and Other Bases in Acetonitrile Solvent. *Can. J. Chem.* **1989**, *67* (4), 590–595. https://doi.org/10.1139/v89-089.

(12) Perinu, C.; Arstad, B.; Jens, K.-J. NMR Spectroscopy Applied to Amine–CO_2–H_2O Systems Relevant for Post-Combustion CO2 Capture: A Review. *Int. J. Greenh. Gas Control* **2014**, *20*, 230–243. https://doi.org/10.1016/j.ijggc.2013.10.029.

(13) Surface, J. In Situ High Pressure and Temperature 13C NMR for the Study of Carbonation Reactions of CO2. *Theses Diss. ETDs* **2013**. https://doi.org/10.7936/K7HM56GR.

(14) Harriman, Anthony. Further Comments on the Redox Potentials of Tryptophan and Tyrosine. *J. Phys. Chem.* **1987**, *91* (24), 6102–6104. https://doi.org/10.1021/j100308a011.

(15) Sjödin, M.; Styring, S.; Wolpher, H.; Xu, Y.; Sun, L.; Hammarström, L. Switching the Redox Mechanism: Models for Proton-Coupled Electron Transfer from Tyrosine and Tryptophan. *J. Am. Chem. Soc.* **2005**, *127* (11), 3855–3863. https://doi.org/10.1021/ja044395o.

(16) Tyburski, R.; Liu, T.; Glover, S. D.; Hammarström, L. Proton-Coupled Electron Transfer Guidelines, Fair and Square. *J. Am. Chem. Soc.* **2021**, *143* (2), 560–576. https://doi.org/10.1021/jacs.0c09106.

(17) Zanello, P. *Inorganic Electrochemistry: Theory, Practice and Application*; The Royal Society of Chemistry: Cambridge: University of Siena, Italy, 2003.

(18) Walter, P.; Kaifer, E.; Herrmann, H.; Wadepohl, H.; Hübner, O.; Himmel, H.-J. Redox-Active Guanidines with One or Two Guanidino Groups and Their Integration in Low-Dimensional Perovskite Structures. *Eur. J. Inorg. Chem.* **2019**, *2019* (38), 4147–4160. https://doi.org/10.1002/ejic.201900975.

(19) Homer, R. B.; Alwis, K. W. Kinetics and Mechanism of the Alkaline Hydrolysis of Guanidine, Hexamethylguanidinium Perchlorate, and Tetramethylurea. *J. Chem. Soc. Perkin Trans. 2* **1976**, No. 7, 781–784. https://doi.org/10.1039/P29760000781.

(20) Limatibul, S.; Watson, J. The Mechanism of Acid Hydrolysis of Guanidines. *J. Org. Chem.* **1971**, *36* (24), 3805–3807. https://doi.org/10.1021/jo00823a601.

(21) Lewis, C. A. Jr.; Wolfenden, R. The Nonenzymatic Decomposition of Guanidines and Amidines. *J. Am. Chem. Soc.* **2014**, *136* (1), 130–136. https://doi.org/10.1021/ja411927k.

(22) Wild, U.; Walter, P.; Hübner, O.; Kaifer, E.; Himmel, H.-J. Evaluation of the Synthetic Scope and the Reaction Pathways of Proton-Coupled Electron Transfer with Redox-Active Guanidines in C−H Activation Processes. *Chem. – Eur. J.* **2020**, *26* (69), 16504–16513. https://doi.org/10.1002/chem.202003424.

(23) Yorimitsu, H.; Nakamura, T.; Shinokubo, H.; Oshima, K.; Omoto, K.; Fujimoto, H. Powerful Solvent Effect of Water in Radical Reaction: Triethylborane-Induced Atom-Transfer Radical Cyclization in Water. *J. Am. Chem. Soc.* **2000**, *122* (45), 11041–11047. https://doi.org/10.1021/ja0014281.

(24) APEX2 Version 2014.11-0, Bruker AXS, Inc.; Madison, WI **2014**.

(25) SAINT Version 8.34a, Bruker AXS, Inc.; Madison, WI **2013**.

(26) Sheldrick, G. M. SADABS, Version 2014/5, Bruker AXS, Inc.; Madison, WI **2014**.

(27) Sheldrick, G. M. SHELXTL, Version 2014/7, Bruker AXS, Inc.; Madison, WI **2014**

(28) International Tables for Crystallography 1992, Vol. C., Dordrecht: Kluwer Academic Publishers.

(29) APEX3 Version 2018.1-0, Bruker AXS, Inc.; Madison, WI **2018**.

Chapter 2: Carbon Dioxide Capture *via* a Ruthenium PNP Pincer Complex

2.1: Introduction

As the Carnot limit does not constrain electrochemical reactions, a growing number of electrochemical CO_2 capture and concentration (eCCC) methods have been explored over the last several decades.[1,2] While an expansive library of homogeneous transition metal (TM) catalysts has been investigated for the catalysis of CO_2 to value-added products, to date, there are only a few examples of TM complexes that have been used as redox carriers for eCCC.[2,3] A key study on mononuclear complexes by DuBois et al. discussed in Chapter 0 (**Figure 0.3**) examined the relationship between the distance of a CO_2 binding site on a ligand to the redox-active metal center.[1,4] Despite being unsuccessful in presenting a TM complex that can electrochemically cycle between CO_2 capture and release, the study does highlight the importance of a smaller atom distance of the CO_2 binding site to the transition metal center. The question is now raised: if another TM complex with a one atom or "closer" distance to the binding site were studied, could that compound be successful in electrochemically cycling CO_2? The many potential combinations of transition metal centers and ligand modifications can provide great tunability for possible CO_2 carriers, which has yet to be fully explored. With the scarcity of TM complexes for eCCC there is an untapped opportunity to systematically expand the scope of TM and ligand combinations for eCCC.

In 2012, Milstein and coworkers reported the reversible nature of CO_2 binding to a Ru^{II}-PNP pincer complex.[5] The study details the activation of CO_2 by metal-ligand cooperation (MLC) at

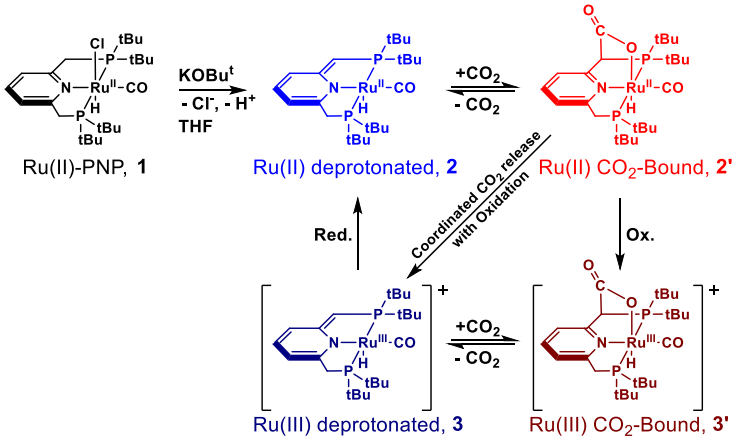

Scheme 2.1: The proposed eCCC cycle for Ru(II)-PNP complex **2**, after deprotonation from **1**.[10]

ambient conditions, with CO_2 binding *via* a Ru–O bond and a C–C bond formed between CO_2 and the deprotonated benzylic arm of the ligand (**Scheme 2.1**, top row). Removal of CO_2 was observed when the bound complex (**2'**) was dissolved in benzene under reduced pressure. Additionally, they reported that when the ^{13}C labeled CO_2 bound complex was exposed to excess unlabeled CO_2 in solution, CO_2 exchange readily occurred, as observed by ^{13}C NMR spectroscopy. Considering the atom distance to the CO_2 binding site as presented by DuBois, the binding of the CO_2 to Ru-PNP *via* MLC could be the key "closer" than one atom distance TM complex, which may facilitate eCCC.

The electrochemical properties of the CO_2-bound and CO_2-unbound species have yet to be studied, but they have the exciting potential to be a springboard for studying a family of TM complexes for eCCC (complete **Scheme 2.1**). Computational results could guide the experimental direction in identifying and designing a TM complex for eCCC. Preliminary calculations of the deprotonated Ru-PNP complex showed promising energy differences between the Ru^{II} CO_2 bound (**2'**) and unbound (**2**) states versus the Ru^{III} CO_2 bound (**3'**) and unbound states (**3**). Expanding the metal centers used and exploring various substitutions on the ligand scaffold would provide information on how to better tune the CO_2 carrier ability of TM complexes.

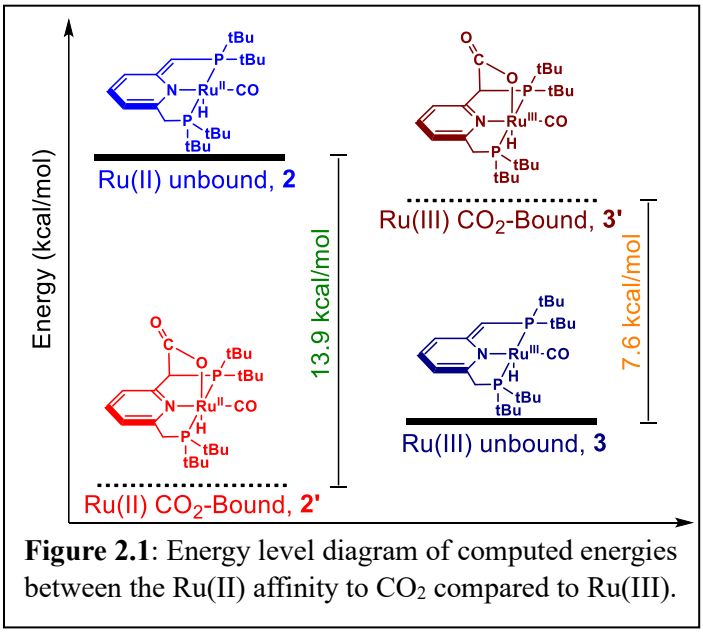

Figure 2.1: Energy level diagram of computed energies between the Ru(II) affinity to CO_2 compared to Ru(III).

2.2: Results (Section 2.2.1 was performed by Dr. Daniel Bim and Dr. Zisheng Zhang, Alexandrova Group, UCLA)

2.2.1: Computational Studies

The Ru^{II}-PNP pincer complex, bound and unbound to CO_2 at varied oxidations, was studied in the low spin state using density functional theory (see details in Experimental **Section 2.5**). From the calculated free energies of each species, the binding energies to CO_2 were found to be -13.9 kcal/mol for the reduced complexes **2** → **2'** and +7.6 kcal/mol for the oxidized complexes **3** → **3'** (**Figure 2.1**). The redox potential for the CO_2 unbound species, **3** → **2**, was calculated to be -0.9 V vs $Fe(C_5H_5)_2^{+/0}$ in THF, using a value $E°_{abs}$ = 5.17 eV for the references of the $Fe(C_5H_5)_2^{+/0}$ redox couple in THF.[6] Following the initial computational findings, the parameters were expanded to study variable substitution around the pincer ligand (**Figure 2.2** and **2.3**) and with different metal centers (**Figure 2.4**).

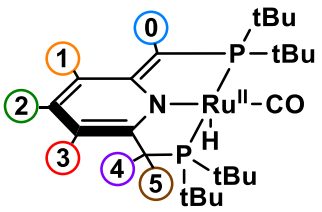

Figure 2.2: The various substitution positions tested around complex **2**.

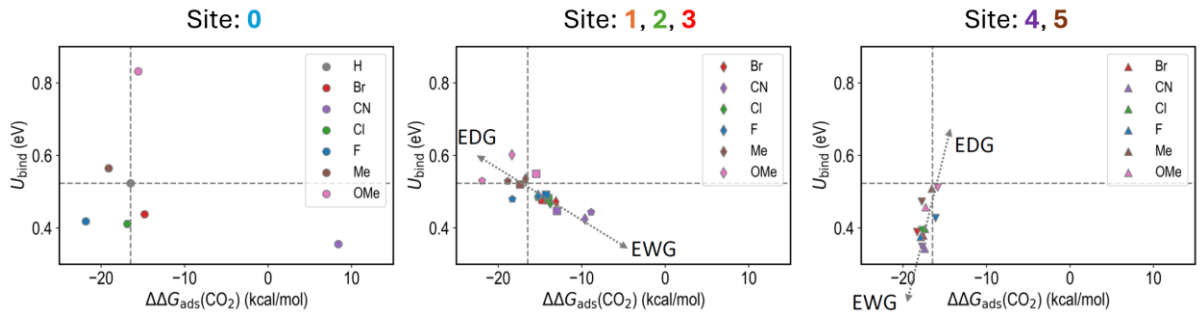

Figure 2.3: The energy relationships of the pincer complex at various sites of substitution.

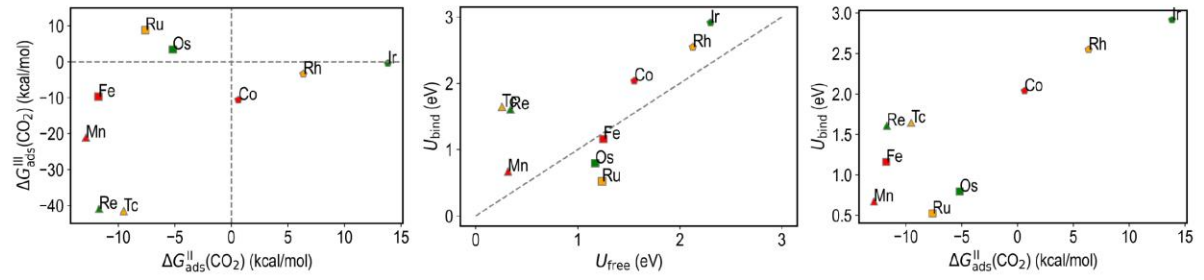

Figure 2.4: The energy relationships of different transition metal centers in the pincer complex.

2.2.2: Experimental Evaluation of the Electrochemical Capture of CO_2 by Ru-PNP

Synthesis of the Ru^{II}-PNP pincer complex [Ru(PNP)tBu)(Cl)(CO)(H)] (**1**), the deprotonated (dearomatized*) [Ru(PNP)tBu*)(CO)(H)] (**2**), and the CO_2 bound [Ru(PNP)tBu-COO)(CO)(H)] (**2'**) were achieved following literature procedures (**Scheme 2.1**).[5]

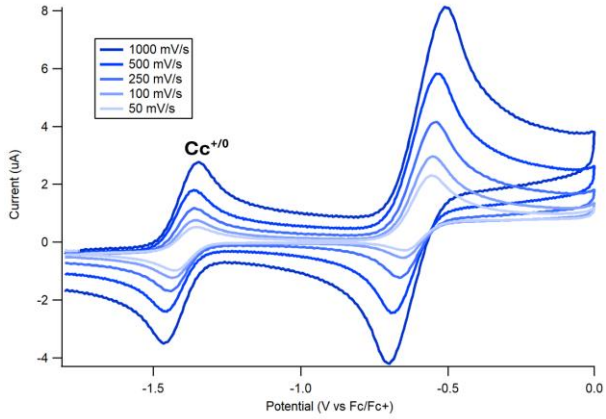

Figure 2.5: CVs of deprotonated Ru-PNP (**3/2**) in THF with 0.1 M $TBAPF_6$ at varied scan rates. See **Table 2.1** for respective i_a/i_c *vs* scan rates.

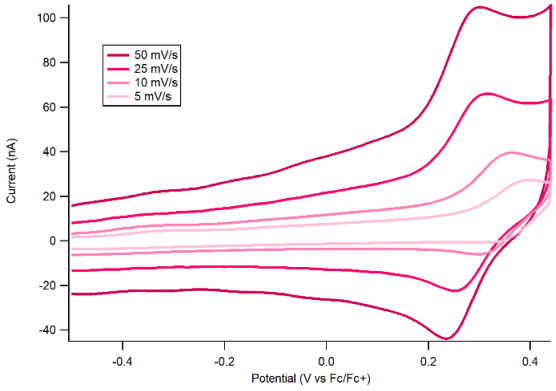

Figure 2.6: CVs of CO_2 bound Ru-PNP (**3'/2'**) in THF with 0.1 M $TBAPF_6$ at varied scan rates. See **Table 2.2** for respective i_a/i_c *vs* scan rates.

Attempts at chemically isolating the oxidized Ru^{III} complex **3** from **2** were unsuccessful. Oxidants $[Fe(C_5H_5)_2][BF_4]$, $AgBF_4$, and $NOBF_4$ were used to no avail, resulting in a decomposed mixed product. Directly metalating the PNP ligand by $Ru^{III}Cl_3(H_2O)_3$ also did not result in the desired oxidized product.

Table 2.1: i_a/i_c vs Scan rates for **3/2**

scan rate (mV/s)	i_c **(µA)**	i_a **(µA)**
1000	7.242	-7.013
500	5.289	-4.533
250	3.905	-1.996
100	2.857	-1.255
50	2.238	-0.960

Table 2.2: i_a/i_c vs Scan rates for **3'/2'**

scan rate (mV/s)	i_c **(nA)**	i_a **(nA)**
50	54.83	-54.66
25	36.67	-32.53
10	24.15	-15.37
5	16.50	-7.547

The electrochemical properties of complexes **2** and **2'** were studied in THF with 100 mM $TBAPF_6$. The deprotonated **2** has an $E_{1/2}$ for the $Ru^{III/II}$ (**3** → **2**) electron couple centered at -0.606 V *vs* $Fe(C_5H_5)_2^{+/0}$ (referenced from $[Co(C_5H_5)_2][PF_6]$ or $Cc^{+/0}$, at -1.4 *vs* $Fe(C_5H_5)_2^{+/0}$). Variable scan rate experiments demonstrate diminished reversibility at scan rates below 250 mV/s with the loss of the return reduction feature (**Figure 2.5**, **Table 2.1**). The CO_2 bound complex **2'** has an anodically shifted $E_{1/2}$ for $Ru^{III/II}$ (**3'** → **2'**) at 0.264 V *vs* $Fe(C_5H_5)_2^{+/0}$. In contrast to the **3/2** couple, the **3'/2'** redox event maintains reversibility at slower scan rates until 10 mV/s (**Figure 2.6**, **Table 2.2**). A wider scan window, as seen in **Figure 2.7**, demonstrates how the **3/2** couple is not shown

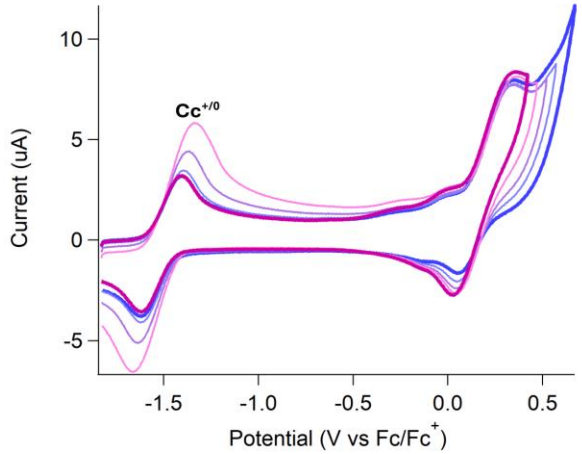

Figure 2.7: Ru-PNP **3** scanned at 1000 mV/s in concentrations of 1 mM in THF with 100 mM $TBAPF_6$, variable window. This illustrates how the anodic window effects the reduction peak.

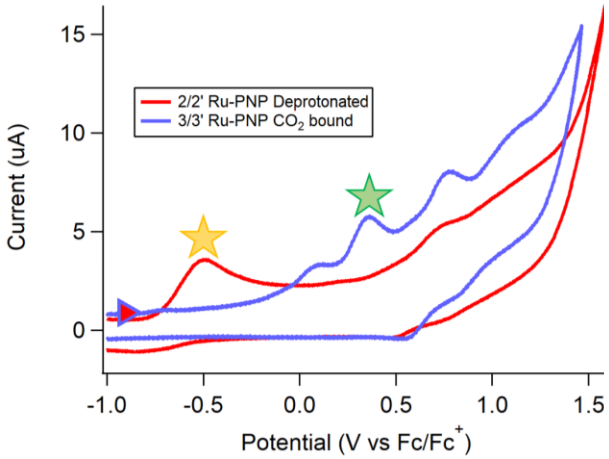

Figure 2.8: Ru-PNP **2** and **3** both at 500 mV/s in conc. of 1 mM in THF with 100 mM $TBAPF_6$. Depending on the anodic window, they lose the return reduction peak. Yellow star is of **2/2'** and green star is of **3/3'** – additional peaks past 500 mV have been assigned as ligand peaks.

to reappear after the oxidation of **2'**. Additional oxidation and reduction peaks between 0.3-0.7 V *vs* $Fe(C_5H_5)_2^{+/0}$ in THF are attributed to ligand-based redox events of the aromatic PNP. After accessing more anodic potentials of the ligand peaks, the observed $Ru^{III/II}$ redox couple loses reversibility due to irreversible changes to the complex (**Figures 2.7** and **2.8**).

In addition to electrochemical studies in THF, CVs were also taken in fluorobenzene to observe if a more nonpolar solvent would affect the redox potentials. In fluorobenzene, the deprotonated (**3/2**) has a $Ru^{III/II}$ couple at $E_{1/2}$ at -0.458 V *vs* $Fe(C_5H_5)_2^{+/0}$. The CO_2 bound (**3'/2'**) $Ru^{III/II}$ redox couple is at 0.336 *vs* $Fe(C_5H_5)_2^{+/0}$.

Experiments to observe CO_2 release from complex **2'** included sparging the solution with argon gas after *in situ* generation of **2'** from **2** by CO_2 sparging. Separate chemical generation of **2'** was also probed. At the slowest CV time scale, the expected unbound couple **3**/**2** is not observed. Controlled oxidative electrolysis of a solution of complex **2'** did not regenerate **2,** but rather decomposed the solution mixture (**Figure 2.9**), explored further in the following experiments.

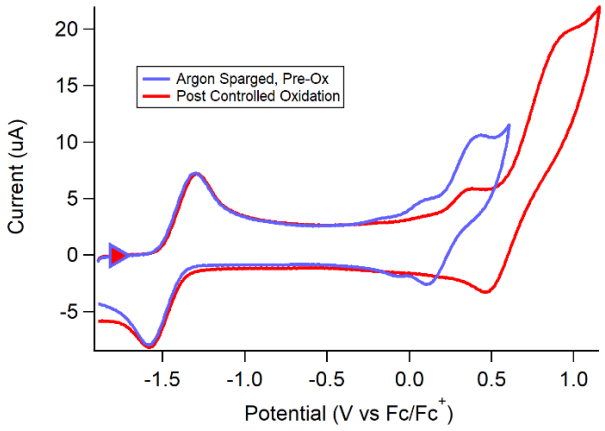

Figure 2.9: CVs of CO_2 bound Ru-PNP (**3/3'**) before and after controlled oxidation.

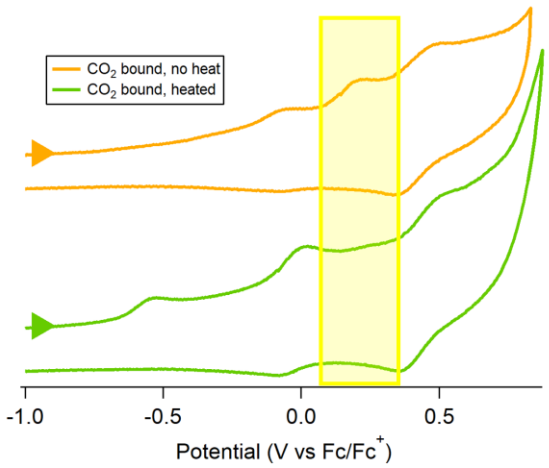

Figure 2.10: Ru-PNP **3** scanned without heating and after heating up to 60 C. 500 mV/s in THF with 100 mM $TBAPF_6$.

To encourage CO_2 release, a solution of **2'** was heated gradually to 60 °C and monitored using cyclic voltammetry. The oxidation feature assigned for **2'** is seen to decrease in intensity over time, while an oxidation feature for the unbound **2** is seen to grow (**Figure 2.10**). The solution changes from yellow to a dull green, corroborating the generation of **2**, which is deep blue. An additional unassigned oxidation peak at 9.5 mV *vs* $Fc^{+/0}$ is present throughout the experiment. Should heating allow for the conversion of **3** to the CO_2-unbound **2**, it does suggest CO_2 release but without electrochemical oxidation of **3**.

Additional experiments with ultraviolet-visible (UV-Vis) spectroscopy were performed to probe the system. Spectroelectrochemical (SEC) UV-Vis experiments of **2** upon oxidation from Ru^{II} to Ru^{III} exhibit the growth of a peak at 275 nm with a concomitant decrease in the peak at 311

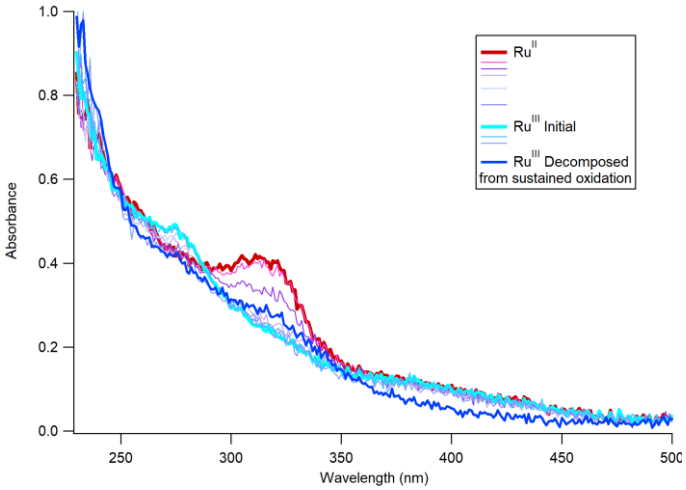

Figure 2.11: SEC UV-Vis experiment of deprotonated Ru^{II} (**2**) being oxidized to Ru^{III} (**3**).

nm (**Figure 2.11**). The addition of CO_2 to **2** to form the CO_2-bound **2'** causes the prominent peak at λ_{max} = 311 nm to diminish but with a broad peak at λ_{max} = 330 to take form (**Figure 2.12**, purple trace). UV-vis spectra were taken before and after controlled oxidation in an H-cell for both **2** and

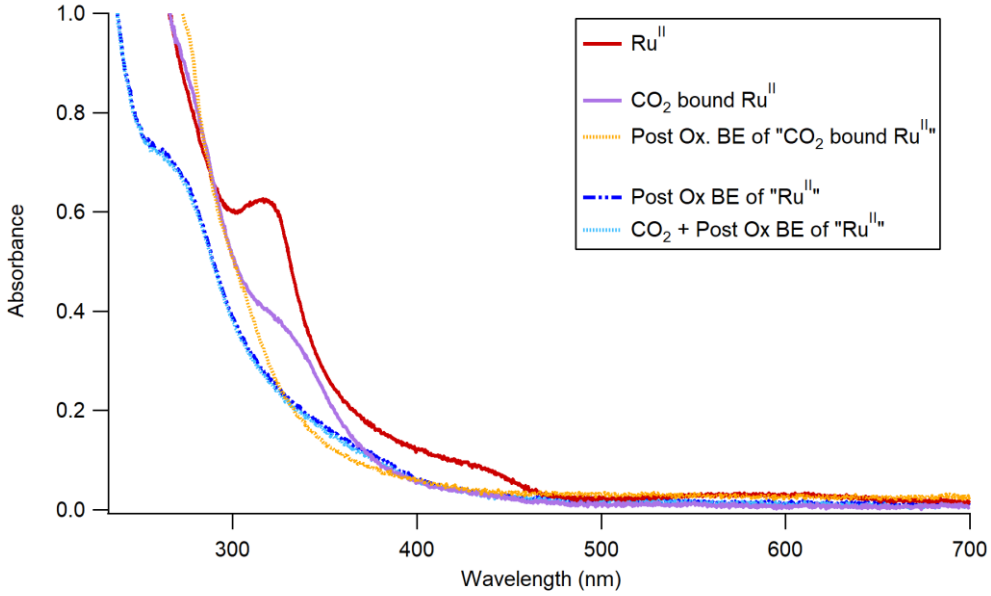

Figure 2.12: UV-Vis spectra of compounds **2** and **2'** before and after controlled oxidation.

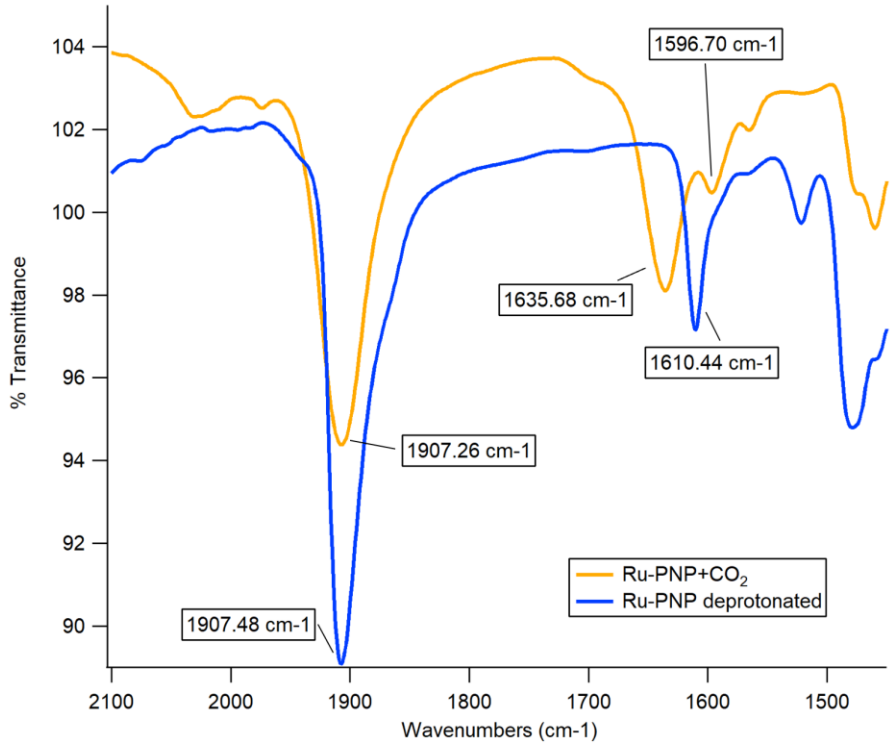

Figure 2.13: IR absorbance spectra of **2** and **2'**.

2' (**Figure 2.12**). The oxidation of **2** (red trace) to **3** (dark blue) follows a similar pattern to that seen in the SEC UV-vis experiment. Oxidation of **2'** (purple trace) results in a different spectrum (yellow trace), indicating a possible loss of CO_2. In addition, as the trace of oxidized **2'** does not match **3**, the resulting spectrum may show a transformation to the potential generation of **3'**. Sparging the solution of the possible oxidized species **3** with CO_2 does not show any change in the spectrum (**Figure 2.12**, light blue trace) which may suggest a lack of CO_2 affinity in the Ru^{III} if the oxidation was successful.

To further probe whether CO_2 is lost upon oxidation, infrared (IR) spectra were taken of **2**, **2'**, and the oxidized solution **3'** (**Figures 2.13, 2.14,** and **2.15**). A diagnostic absorption at around 1635 cm^{-1} for the carboxylate is observed in a solid sample of **2'**, at 1634 cm^{-1} in a solution of **2'** and electrolyte solution, but not in the solution after oxidative electrolysis (**Figure 2.14**). IR spectra

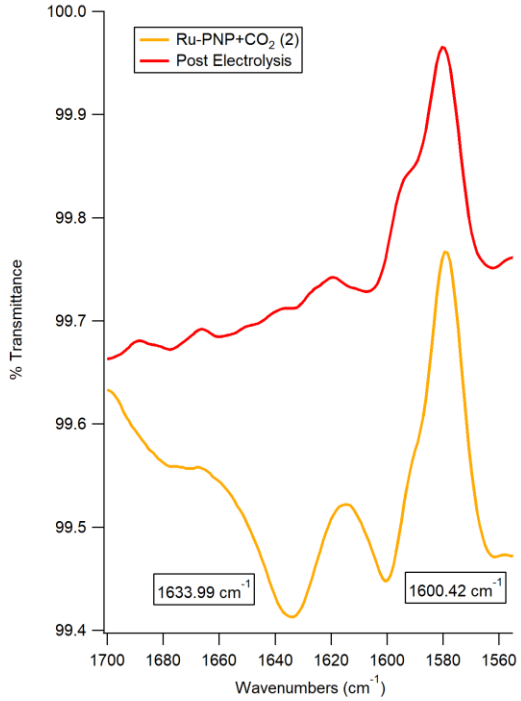

Figure 2.14: FT-IR absorption in the carboxylate region before and after oxidative electrolysis of **2'**.

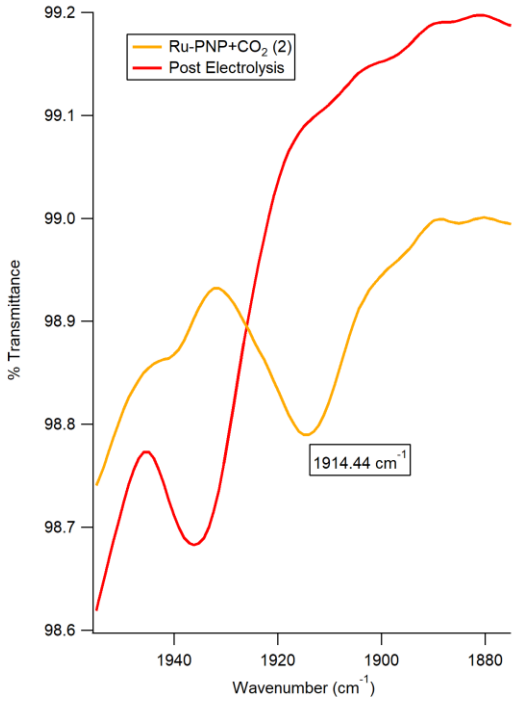

Figure 2.15: FT-IR absorption in the carbonyl region before and after oxidative electrolysis of **2'**. Observed loss of CO ligand.

of **2** and **2'** display strong absorptions at 1907-1914 cm^{-1} indicative of the carbonyl ligand, while the oxidized solution (**3'**) no longer maintains this absorption (**Figure 2.15**). This data suggests CO_2 is released upon oxidation and that this process is concomitant with decomposition of the compound. The decomposition of the oxidized complex is consistent with our unsuccessful efforts to chemically isolate this species.

Other observations made on this system include a color change of compound **2** from its deep blue color to yellow when dissolved in MeCN, potentially indicating coordination of MeCN to the complex. While the $E_{1/2}$ potentials for **3/2** indicate air stability, as they are positive of the O_2/O_2^- couple, the compound displays decomposition in the NMR and by an obvious color change from blue to brown upon exposure to air, potentially due to reactivity of the hydride or water sensitivity. The CO_2-bound complex **2'**, which is a beige solid, was not immediately soluble in pentane. However, it was observed when **2'**, under a nitrogen atmosphere in a glove box, was allowed to sit in pentane over the course of 20 minutes, the complex transformed back to **2** as evidence by the formation of a deep blue solution, indicating CO_2 release.

2.3: Discussion

Ultimately, the isolation of the oxidized Ru^{III} complexes through either chemical or electrochemical generation would help probe the CO_2 affinity. Unfortunately, to the best of the author's knowledge, there is no literature precedence of Ru^{III}PNP complexes. The ligand environment plays a crucial role in the stability of either the Ru^{II} or Ru^{III} metal center, with imidazole-type ligands stabilizing Ru^{III} centers as a π-donor compared to pyridine-type ligands, which stabilize Ru^{II} by being a π-acceptor.[7–10] More acidic environments are known to stabilize Ru^{III} which may be why the $Ru^{III/II}$ (**3'/2'**) couple in the CO_2 sparged THF solution remains more reversible at slower scan rates compared to the $Ru^{III/II}$-dearomatized/unbound (**3/2**).[11–13] These

observed characteristics of Ru^{III} may also explain why attempts to oxidize **2** and isolate **3** have been unsuccessful as **2**, the Ru-PNP catalyst activated form, is relatively basic with a pK_a of 20.2 in THF for the double bonded carbon on the arm of the ligand.[14] Additionally, in THF, the CO_2 bound complex **2'** has been reported to have a ligand pK_a of 24.6, a notable ~4 unit increase as a 6-coordinate complex. The free PNP ligand has pK_a of 28.6, illustrating how the Ru metal center facilitates the acidity of the ligand.[14] The PNP pincer ligand scaffold is also not redox innocent and can be oxidized.[15,16]

The shift of 0.87 V for the $E_{1/2}$ couple between **3/2** and **3'/2'** in THF with CO_2 is consistent with the preliminary computational studies that describe CO_2 binding in this system. From this electrochemical potential shift, an estimation of the CO_2 binding constant can be calculated from the following **Equation 2.1**:

(2.1) $$\Delta E = q\frac{0.0592}{n}\log[CO_2] + \frac{0.0592}{n}\log(K_{CO2})$$

For **2** in THF, the binding constant is found to be $\log K_{CO2} = 15$, (converted to approximately -20.5 kcal/mol). In fluorobenzene, the electrochemical potential shift is 0.79 V, which correlates to a smaller binding constant of about $\log K_{CO2} = 13$ (approximately -17.7 kcal/mol). These values can be compared to the calculated CO_2 binding, **2 → 2',** which has been calculated to be favorable for Ru^{II} by -13.9 kcal/mol. Based on the computational studies, release of CO_2 is expected to also be favorable by -7.6 kcal/mol upon oxidation, or **3' → 3** (**Figure 2.1**).

CO_2 liberation is not observed upon electrochemical oxidation, despite the thermodynamic favorability of CO_2 release. This kinetic inertness is supported by calculations that suggest a large activation energy for CO_2 desorption from the bound Ru^{III} complex. This observation aligns with other literature sources indicating the less reactive nature of Ru^{III} complexes compared to Ru^{II}.[17]

Additionally, the stability of the CO_2 bound complex **2'** is due to the re-aromatization of the complex when CO_2 bound. Regeneration of complex **2** from **3** requires de-aromatization of the system, which is energetically unfavorable. Another reason that **2** is difficult to regenerate is that decomposition is observed throughout the electrochemical experiments.

To address the issues of regenerating **2**, computational findings suggest the addition of an electron-withdrawing group (EWG) to the ligand aromatic ring to encourage de-aromatization (**Figure 2.3**). In general, the electronic effects from the variable substitutions computationally tested around the pincer ligand, found that in the aromatic system (**Figure 2.2**, sites: 1, 2, and 3) a linear trend and shift with both binding energies and redox potentials. At substitution sites 4 and 5, not in the aromatic system, shifts were only seen in the redox potential. At site 0 of CO_2 binding, the direct steric effect of the different substituents breaks the linear scaling relationship. In addition to ruthenium, of the other transition metal complexes computationally surveyed, only osmium shows favorable energetics with a positive ΔG for the CO_2-bound complex in the oxidized Os (III) state (**Figure 2.4**).

2.4: Conclusions

Unfortunately, a Ru-PNP complex known to bind CO_2 *via* MLC could not be driven to electrochemically cycle CO_2 despite promising initial computation results. FT-IR spectra of the oxidized CO_2-bound complex suggest the release of CO_2 and decomposition. With many factors still unknown about this system, future studies will aim for more systematic testing of the parameters of CO_2 binding and release. Future directions will entail characterizing all possible intermediates in the binding and release of CO_2. Of the intermediates of interest, this will include attempting to isolate and study the paramagnetic Ru^{III}-CO_2 bound (**3'**) complex and examining its binding or lack thereof to CO_2. In addition, the experimental exploration of derivative with

different ligand, ligand substitutions, and metal centers can also shed light on the CO_2 binding and release ability by MLC of TM redox carriers. With collaborative efforts with computational chemists, we hope to be able to identify and create a working TM redox carrier for electrochemical CO_2 cycling.

2.5: Experimental

Computational Methods: All of the calculations were carried out using the Turbomole 6.6 program.[18] The structures were optimized using the TPSS functional[19], the hybrid basis set (def2-TZVP for the Ru and all of the ligating atoms; def2-SVP for the rest of the system)[20], and the zero-damping dispersion correction (D3)[21]. The effect of solvation on geometry optimizations was included by employing the implicit conductor-like screening model (COSMO)[22] with a dielectric constant of $\varepsilon = 4$. The calculations were accelerated by resolution-of-identity approximation (RI).[23] The variations in the ligand substitution and metal centers used the following theoretical method details. Geometry and frequency: B3LYP-D3(BJ)/def2-SVP, solvation-free energy: uESE, electronic energy where hybrid GGA: PBE0-D4/def2-TZVPP, hybrid meta-GGA: ωB97M-V/def2-TZVPP, and double hybrid: PWPB95/def2-TZVPP.

Synthesis and Materials

General Methods: Synthetic work was carried out under a dinitrogen (N_2) atmosphere with standard Schlenk techniques or in a glovebox where noted. All solvents and reagents were purchased from commercial vendors and used without further purification unless otherwise noted. Deuterated tetrahydrofuran (THF) and dimethyl sulfoxide (DMSO) used for NMR characterization were purchased from Cambridge Isotope Laboratories, Inc., and were degassed via free−pump−thaw and stored over activated 3 Å molecular sieves. Tetrabutylammonium

hexafluorophosphate ($TBAPF_6$) was purified via recrystallization from ethanol and dried under a heated (80 °C) vacuum (1×10^{-3} Torr) and stored in a glovebox. Experiments using carbon dioxide (CO_2) atmospheres were performed using ultrahigh purity (99.999%) CO_2, which was additionally passed through a purification column to eliminate residual H_2O, O_2, CO, halocarbons, and sulfur compounds.

The following compounds were synthesized in accordance with preparation found in the referenced literature. Ru(PNP)tBu)(Cl)(CO)(H) (**1**)[5], Ru(PNP)tBu*)(CO)(H) (**2**)[6], Ru(PNP)tBu-COO)(CO)(H) (**3**)[6]

Electrochemical Methods: Electrochemical experiments were carried out under an atmosphere of N_2 or CO_2, where indicated. Solutions for electrochemical measurements were recorded in THF or fluorobenzene using 100 mM $TBAPF_6$ or 100 mM KCl as the supporting electrolytes, respectively. Cyclic voltammetry (CV) was performed with a Pine instrument WaveDriver 10 potentiostat. When specified, cobaltocenium hexafluorophosphate or ferrocene was used as an internal standard, and potentials were referenced to the ferrocenium/ferrocene ($Fe(C_5H_5)_2^{+/0}$) couple. Between CV scan, the working electrode was polished in a figure eight pattern with an alumina slurry (0.05 um) on a microcloth (2.875 in, PSA backed). Controlled potential electrolysis experiments were performed stirred in a custom H-cell with the working and the counter cells divided by a porous glass frit. In the working compartment, carbon fabric was used as the working electrode and SCE as the reference. A glassy carbon rod was used as the counter electrode on the counter side cell. UV−visible spectroelectrochemistry (UV−vis SEC) was performed using a UV−vis SEC kit from Pine Instruments with a Pt working/counter electrode and Ag wire as a pseudo reference electrode.

Physical Methods: Ultraviolet-visible (UV–vis) spectra were collected in a 10 mm or 1 mm pathlength quartz cuvette, using an Agilent Technologies Cary 60 UV–vis spectrometer. UV-visible spectroelectrochemistry experiments were conducted in a commercially available UV-vis spectroelectrochemistry kit from Pine Instrument with Pt working/counter electrode and Ag wire as a pseudo reference electrode. CO_2 monitoring was performed on a CM-0111 gas sensor kit CM-0111 by CO_2Meter with the software GasLab. Fourier Transform Infrared (FTIR) spectra were collected by using a Thermo Scientific Nicolet iS5 FTIR Spectrometer with iD5 diamond ATR. ^{1}H, and $^{13}C\{^{1}H\}$ NMR spectra were recorded at 500 MHz on Bruker or 600 MHz Varian instruments. ^{1}H NMR spectra chemical shifts are reported as δ values in ppm relative to residual protio solvent.

2.6 References

(1) Dubois, D. L.; Miedaner, A.; Bell, W.; Smart, J. C. Electrochemical concentration of carbon dioxide. In *Electrochemical and Electrocatalytic Reactions of Carbon Dioxide*; Elsevier, 1993; pp 94–117. https://doi.org/10.1016/B978-0-444-88316-2.50008-5.

(2) Zito, A.; Clarke, L.; Barlow, J.; Bim, D.; Zhang, Z.; Ripley, K.; Li, C.; Kummeth, A.; Leonard, M.; Alexandrova, A.; Brushett, F.; Yang, J. Electrochemical Carbon Dioxide Capture and Concentration. *Chem Rev* **2022**.

(3) Rheinhardt, J. H.; Singh, P.; Tarakeshwar, P.; Buttry, D. A. Electrochemical Capture and Release of Carbon Dioxide. *ACS Energy Lett.* **2017**, *2* (2), 454–461. https://doi.org/10.1021/acsenergylett.6b00608.

(4) Appel, A. M.; Newell, R.; DuBois, D. L.; Rakowski DuBois, M. Concentration of Carbon Dioxide by Electrochemically Modulated Complexation with a Binuclear Copper Complex. *Inorg. Chem.* **2005**, *44* (9), 3046–3056. https://doi.org/10.1021/ic050023k.

(5) Vogt, M.; Gargir, M.; Iron, M. A.; Diskin-Posner, Y.; Ben-David, Y.; Milstein, D. A New Mode of Activation of CO2 by Metal-Ligand Cooperation with Reversible C–C and M–O Bond Formation at Ambient Temperature. *Chem. - Eur. J.* **2012**, *18* (30), 9194–9197. https://doi.org/10.1002/chem.201201730.

(6) Romańczyk, P. P.; Rotko, G.; Kurek, S. S. The Redox Potential of the Phenyl Radical/Anion Couple and the Effect Thereon of the Lithium Cation: A Computational Study. *Electrochem. Commun.* **2014**, *48*, 21–23. https://doi.org/10.1016/j.elecom.2014.08.003.

(7) Gütlich, P.; Garcia, Y.; Goodwin, H. A. Spin Crossover Phenomena in Fe(II) Complexes. *Chem. Soc. Rev.* **2000**, *29* (6), 419–427. https://doi.org/10.1039/B003504L.

(8) Jabłońska-Wawrzycka, A.; Rogala, P.; Michałkiewicz, S.; Hodorowicz, M.; Barszcz, B. Ruthenium Complexes in Different Oxidation States: Synthesis, Crystal Structure, Spectra and Redox Properties. *Dalton Trans.* **2013**, *42* (17), 6092–6101. https://doi.org/10.1039/C3DT32214A.

(9) Browne, W. R.; Hage, R.; Vos, J. G. Tuning Interaction in Dinuclear Ruthenium Complexes: HOMO versus LUMO Mediated Superexchange through Azole and Azine Bridges. *Coord. Chem. Rev.* **2006**, *250* (13), 1653–1668. https://doi.org/10.1016/j.ccr.2005.12.008.

(10) Chowdhury, N. S.; Seth, D. K.; Drew, M. G. B.; Bhattacharya, S. Ruthenium Mediated C–H Activation of Benzaldehyde Thiosemicarbazones: Synthesis, Structure and, Spectral and

Electrochemical Properties of the Resulting Complexes. *Inorganica Chim. Acta* **2011**, *372* (1), 183–190. https://doi.org/10.1016/j.ica.2011.02.008.

(11) Bardwell, D. A.; Black, D.; Jeffery, J. C.; Schatz, E.; Ward, M. D. Co-Ordination Chemistry of Mixed Pyridine–Phenol Ligands; Electrochemical, Electron Paramagnetic Resonance and Structural Studies on Monounclear Ruthenium(III) and Chromium(III) Complexes. *J. Chem. Soc. Dalton Trans.* **1993**, No. 15, 2321–2327. https://doi.org/10.1039/DT9930002321.

(12) Bhattacharya, S.; Boone, S. R.; Fox, G. A.; Pierpont, C. G. Periodic Trends in Charge Distribution for Transition-Metal Complexes Containing Catecholate and Semiquinone Ligands. Synthetic, Physical, and Stereodynamic Properties of the Tris(3,5-Di-Tert-Butylquinone) Complexes of Ruthenium and Osmium. *J. Am. Chem. Soc.* **1990**, *112* (3), 1088–1096. https://doi.org/10.1021/ja00159a031.

(13) Pramanik, N. C.; Bhattacharya, S. Chemistry of 2-(Arylazo)Phenolate Complexes of Ruthenium. Synthesis, Characterization and Redox Properties. *Polyhedron* **1997**, *16* (17), 3047–3053. https://doi.org/10.1016/S0277-5387(97)00028-4.

(14) Mathis, C. L.; Geary, J.; Ardon, Y.; Reese, M. S.; Philliber, M. A.; VanderLinden, R. T.; Saouma, C. T. Thermodynamic Analysis of Metal–Ligand Cooperativity of PNP Ru Complexes: Implications for CO_2 Hydrogenation to Methanol and Catalyst Inhibition. *J. Am. Chem. Soc.* **2019**, *141* (36), 14317–14328. https://doi.org/10.1021/jacs.9b06760.

(15) Ingleson, M. J.; Pink, M.; Fan, H.; Caulton, K. G. Redox Chemistry of the Triplet Complex (PNP)CoI. *J. Am. Chem. Soc.* **2008**, *130* (13), 4262–4276. https://doi.org/10.1021/ja074378+.

(16) Adhikari, D.; Mossin, S.; Basuli, F.; Huffman, J. C.; Szilagyi, R. K.; Meyer, K.; Mindiola, D. J. Structural, Spectroscopic, and Theoretical Elucidation of a Redox-Active Pincer-Type Ancillary Applied in Catalysis. *J. Am. Chem. Soc.* **2008**, *130* (11), 3676–3682. https://doi.org/10.1021/ja7108486.

(17) Delferro, M.; Marchiò, L.; Tegoni, M.; Tardito, S.; Franchi-Gazzola, R.; Lanfranchi, M. Synthesis, Structural Characterisation and Solution Chemistry of Ruthenium(III) Triazole-Thiadiazine Complexes. *Dalton Trans.* **2009**, No. 19, 3766–3773. https://doi.org/10.1039/B823271G.

(18) Ahlrichs, R.; Bär, M.; Häser, M.; Horn, H.; Kölmel, C. Electronic Structure Calculations on Workstation Computers: The Program System Turbomole. *Chem. Phys. Lett.* **1989**, *162* (3), 165–169. https://doi.org/10.1016/0009-2614(89)85118-8.

(19) Tao, J.; Perdew, J. P.; Staroverov, V. N.; Scuseria, G. E. Climbing the Density Functional Ladder: Nonempirical Meta--Generalized Gradient Approximation Designed for Molecules and Solids. *Phys. Rev. Lett.* **2003**, *91* (14), 146401. https://doi.org/10.1103/PhysRevLett.91.146401.

(20) Weigend, F.; Ahlrichs, R. Balanced Basis Sets of Split Valence, Triple Zeta Valence and Quadruple Zeta Valence Quality for H to Rn: Design and Assessment of Accuracy. *Phys. Chem. Chem. Phys.* **2005**, *7* (18), 3297–3305. https://doi.org/10.1039/B508541A.

(21) Grimme, S.; Antony, J.; Ehrlich, S.; Krieg, H. A Consistent and Accurate Ab Initio Parametrization of Density Functional Dispersion Correction (DFT-D) for the 94 Elements H-Pu. *J. Chem. Phys.* **2010**, *132* (15), 154104. https://doi.org/10.1063/1.3382344.

(22) Klamt, A.; Schüürmann, G. COSMO: A New Approach to Dielectric Screening in Solvents with Explicit Expressions for the Screening Energy and Its Gradient. *J. Chem. Soc. Perkin Trans. 2* **1993**, No. 5, 799–805. https://doi.org/10.1039/P29930000799.

(23) Eichkorn, K.; Treutler, O.; Öhm, H.; Häser, M.; Ahlrichs, R. Auxiliary Basis Sets to Approximate Coulomb Potentials. *Chem. Phys. Lett.* **1995**, *240* (4), 283–290. https://doi.org/10.1016/0009-2614(95)00621-A.

Chapter 3: Heterocyclic Carbenes for CO_2 Capture: Experimental Data for *N*-Heterocyclic Carbenes in Support of a Computational Study

3.1 Introduction

A challenge towards achieving direct air capture (DAC) is the low concentration of CO_2 found in atmospheric mixes (0.04%). This low concentration of CO_2 requires capture molecules with high CO_2 binding affinity and selectivity. Amines are currently the most widely used molecules in DAC methods, with extensive experimental and theoretical research already being undertaken on their use as a CO_2 capture agent.[1,2] Primary and secondary amines react with CO_2 in a 2:1 stoichiometry to yield a carbamate salt. However, this stoichiometry limits their efficiency in absorbing CO_2. The high basicity of amines ($pK_{a2} > 20$) means that their corresponding amide is generally not the most suitable for aqueous CO_2 capture (pK_a of water = 15.7).[3] Where the pK_{a2} discussed here is the second deprotonation of ammonium for primary and secondary amines ($R_1R_2NH \rightarrow R_1R_2N^-$), as opposed to pK_{a1} ($R_1R_2NH_2^+ \rightarrow R_1R_2NH$). Given the very high concentration of H_2O in the air, it would be beneficial that CO_2 capture molecules are stable in aqueous and oxidizing environments.

The issue herein is that CO_2 reacts as a Lewis acid, with the same mechanism as the binding of a proton. The challenge is tuning the Brønsted basicity of a molecule against protonation while maintaining sufficient Lewis base character for CO_2 affinity in aqueous solutions. Alexandrova, Yang, and coworkers previously investigated alkoxide and phenoxide molecules, another class of CO_2 sorbents, that would retain their CO_2 binding affinity while not being protonated by water.[3] They employed an inverse molecular design technique, working backwards to identify various alkoxides and phenoxides that are sufficiently acidic and remain deprotonated in water while maintaining an affinity for CO_2. In addition, they found that different mechanisms were favored for CO_2 and proton binding to phenoxide sorbents when bulky substituents are present; CO_2 binding favors the second highest occupied molecular orbital (HOMO-1) to minimize steric clash.

Their work indicates that CO_2 and proton affinity can be tuned separately and highlights the potential for uncovering molecules that can act as CO_2 sorbents in aqueous environments.

This work begins with a computational examination of a library of carbenes to scope potential candidates for aqueous CO_2 capture. Carbenes are organic molecules featuring a lone pair localized on a carbon atom, in this case, in the singlet ground state. Extensive computational and experimental research has already been undertaken on the ability of various carbenes as CO_2 capture molecules, particularly *N*-heterocyclic carbenes (NHCs), the most widely available heterocyclic carbene.[4–6] Our goal in this work is to assess the electronic and steric influence of substituents on carbenes in their ability to participate in CO_2 capture (**Figure 3.1**). Gibbs free energy calculations were performed using an implicit solvent model to assess CO_2 binding affinity and pK_a's of carbenes in water to find water-stable carbenes that retain CO_2 affinity.

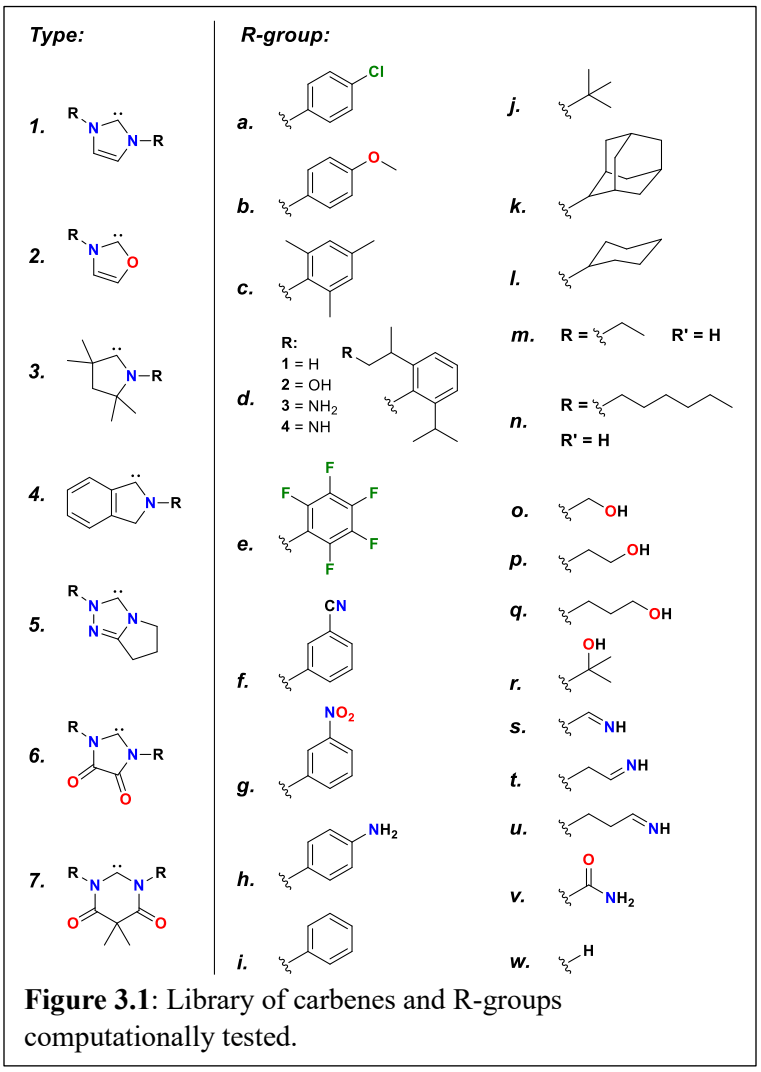

Figure 3.1: Library of carbenes and R-groups computationally tested.

While identifying water-stable carbenes is an attractive goal, it was also understood that the very alkaline nature of carbenes would mean that most carbenes would be prone to protonation

in water and, hence, not suitable for aqueous DAC. Another goal then emerged to study the more basic carbenes in organic solvents, dimethyl sulfoxide (DMSO) and acetonitrile (MeCN), to further expand the library of data in these solvents. Ji and coworkers have performed a comprehensive study into the relationship between CO_2 binding energies and pK_a values in DMSO, finding that the linear relationship between CO_2 binding and proton affinity holds in most cases, with more basic carbenes acting best as CO_2 absorbents.[7] Studies of carbenes in non-aqueous solvents could open the door to using some carbene molecules in non-aqueous CO_2 capture systems, with ionic liquids appearing to be a promising area of research.[8–12] Furthermore, in non-aqueous solvents, the potential to capture CO_2 and then perform an electrochemical conversion has been explored to circumvent the issue of protonation in water. Several recent publications have shown promising results in using organic solvents such as DMSO in direct CO_2 capture and electrochemical conversion.[13,14] Computational results in nonaqueous solvents found in this study were validated experimentally by monitoring the carboxylate formation among synthetically accessible *N*-heterocyclic carbenes.

3.2 Results and Discussion

(Sections 3.2.1 and 3.2.2 are unpublished work performed by Samuel Greenbank under the supervision of Professor Anastasia Alexandrova)

3.2.1 Computational Examination of Carbenes in Water

A library of carbene molecules was tested for CO_2 binding energy and pK_a (**Figure 3.1**). The carbenes tested included previously mentioned *N*-heterocyclic carbenes (NHCs, Type **1**), oxazolylidines (OXCs, Type **2**), cyclic alkyl amino carbenes (CAACs, Type **3**), cyclic amino aryl carbenes (CAArCs, Type **4**), 1,2,4-triazol-5-ylidenes (TAZCs, Type **5**), 5-membered

diamidocarbenes (5-DACs, Type **6**), and 6-membered diamidocarbenes (6-DACs, Type **7**). A selection of R groups were tested, including substituted phenyl rings containing electron-withdrawing and donating groups and a range of hydrogen bond donating groups. When CO_2 binds to a carbene, it forms a charged carboxylate product, which carries a delocalized negative charge that is concentrated on the two oxygen atoms (**Figure 3.2**). The computational values for the pK_a in water, and later for other solvents, is calculated using the dielectric constant of the solvents. This explains the computational values higher than 14 of the computed carbenes in water. We also considered hydrogen bonding interactions to stabilize the carboxylate formed upon CO_2 binding. Yang and coworkers previously demonstrated how additions of alcohols were found to shift the trends for CO_2 binding observed in a quinone system.[15] Therefore, it was hypothesized that hydrogen bond donors near this negatively charged carboxylate group would stabilize and aid in CO_2 binding.

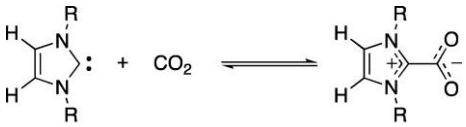

Figure 3.2: Addition of CO_2 to a carbene (NHC) to give a carboxylate.

All carbenes bind CO_2 primarily through a σ-bonding mechanism between the HOMO of the carbene and the LUMO of the CO_2. This was confirmed using localized bonding orbital and Mayer bond order analysis. This localized orbital with the highest Mayer bond order involved in binding to CO_2, in the case of NHC **1W**, can be seen in **Figure 3.3**. With no R-groups present, CO_2 lies parallel to the heterocyclic ring, as seen by the potential energy scan (PES) for molecule **1W** in **Figure 3.4**. However, R-groups on either side of the carbene can cause the CO_2 to bind at intermediate angles.

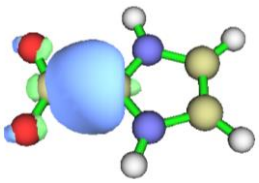

Figure 3.3: Primary σ-bonding orbital involved in CO_2 binding to a carbene.

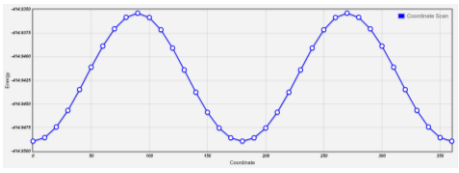

Figure 3.4: Potential energy scan (PES) of NHC **1W**, showing the preferred CO_2 binding of 0°.

How the various steric and electronic effects combine to produce the intermediate binding angles seen is not yet fully understood.[16] All carbenes studied generally follow the expected linear relationship between CO_2 binding and pK_a when tested in water (**Figure 3.5**).

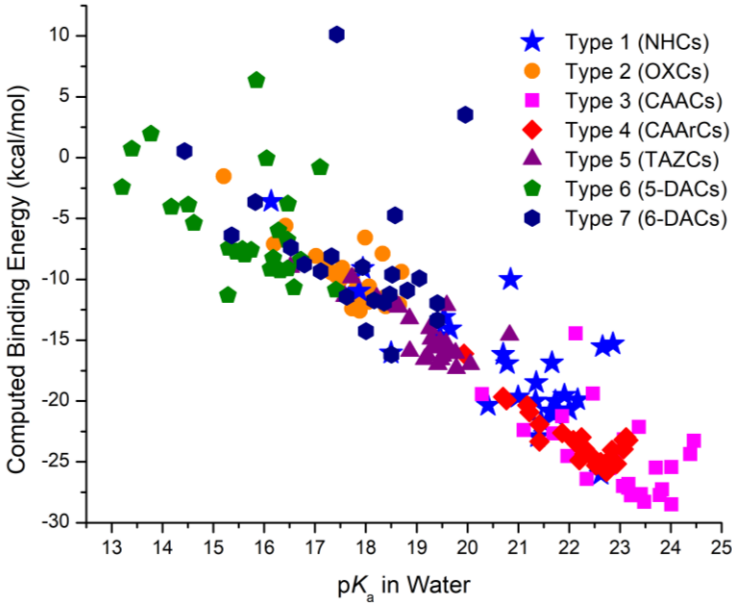

Figure 3.5: Graph of pK_a vs. CO_2 binding energy for all molecules tested in water.

Among the substituents tested for each carbene group, substituents that strayed farther above the trendline could be attributed to being bulky in nature, which caused the CO_2 to bind closer to a perpendicular angle. These groups include *t*-butyl (**J**), adamantyl (**K**), and *t*-butyl alcohol (**S**). The R-groups of carbenes that lie below the trend line generally possess hydrogen bond donor groups. These groups include diisopropyl benzene substituted with an -OH or -NH_2 groups (**D2**, **D3**), methanol (**O**), and ethanol

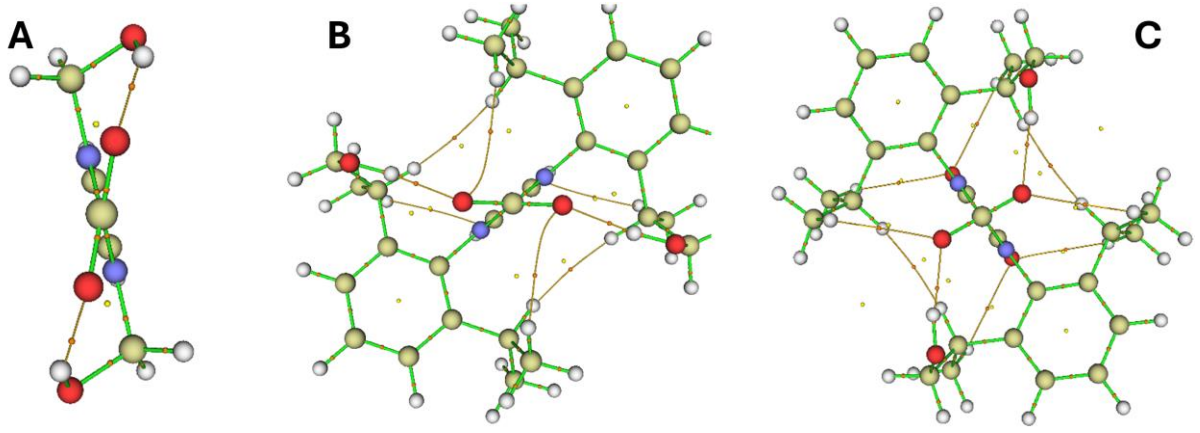

Figure 3.6: QTAIM displaying the hydrogen bonding interactions of molecules; (**A**) **1O**, (**B**) **1D2**, (**C**) **6D2**.

(**P**) substituents. Quantum theory of atoms in a molecule (QTAIM) analysis of these molecules confirmed the presence of hydrogen bonds between the R-groups and bound CO_2 (**Figure 3.6)**.

Of the carbene types tested, the only ones to have variations at pK_a values lower than water (pK_{aw} = 15.7, the rational value described by Brønsted) were diamidocarbenes with ring sizes of 5 (5-DACs, Type **6**) and 6 (6-DACs, Type **7**). Diamidocarbenes feature two carbonyl groups in the carbene ring framework, which are electron-withdrawing. Therefore, 5- and 6-DACs possess a lower electron density at the carbene carbon, making them less susceptible to protonation.[17,18] The decreased electron density at the carbene carbon will also cause a marked effect on CO_2 binding through the same mechanism as proton binding. **Figure 3.7** shows the 5-DACs (Type 6) R-groups with a pK_a lower than water. The majority are phenyl derivatives, often containing electron-withdrawing groups. This decreases the Lewis basicity at the carbene carbon, which scales with the decreased pK_a observed.

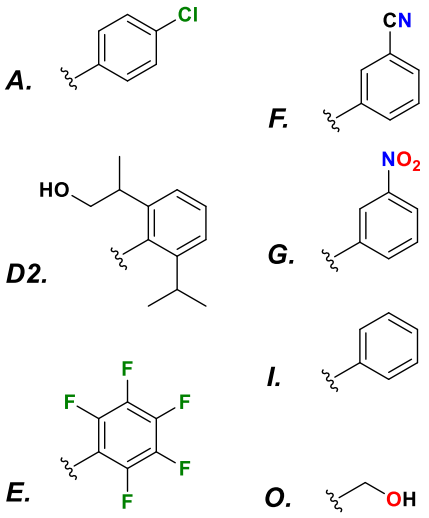

Figure 3.7: R-groups for 5-DACs (Type **6**) found to have a pK_a lower than that of water, whilst maintaining CO_2 binding affinity.

3.2.2 Computational Examination of Carbenes in Non-Aqueous Solvents

Due to the basic nature of carbenes, most are not suitable for aqueous CO_2 capture systems. Therefore, we tested the most basic carbene families in aprotic organic solvents DMSO and MeCN. The families tested were NHCs (Type **1**), OXCs (Type **2**), CAACs (Type **3**), and CAArCs (Type **4**). The carbenes tested showed generally weaker CO_2 binding in the organic solvents. This can be attributed to the fact that when CO_2 binds, a zwitterionic carboxylate intermediate is formed. These are less stable in aprotic solvents of lower polarity than water hence the free energy of CO_2 binding

is favored. Research from Denning and Falvey details how a more polar environment will lead to a shorter and stronger carbene–CO_2 bond, and they suggest that lowering the polarity of the solvent will reduce the effect of electrostatic forces on the bond distance.[16]

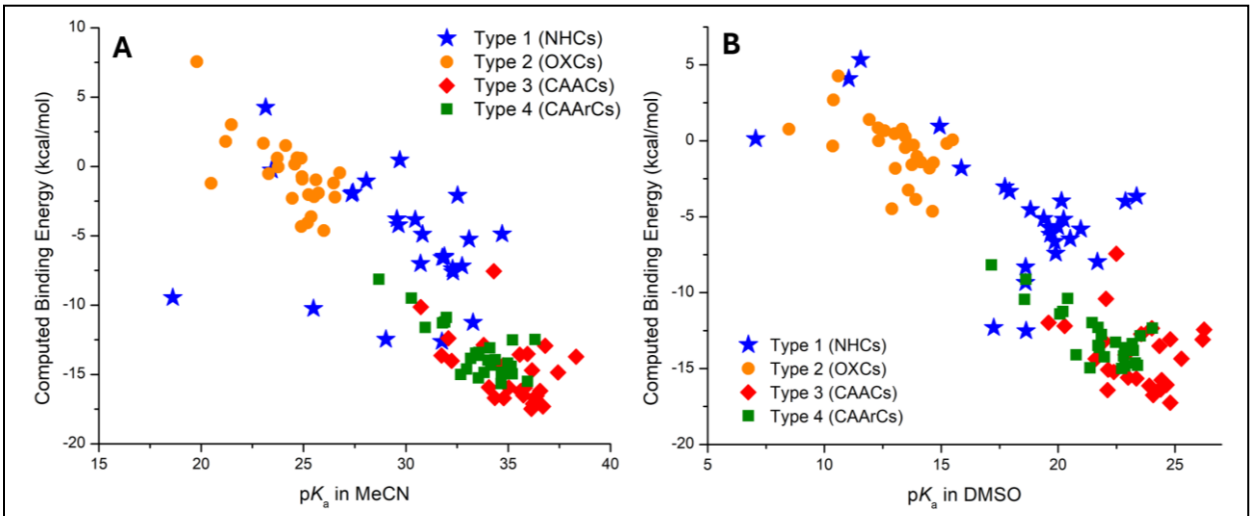

Figure 3.8: **A:** Graph of pK_a vs. CO_2 binding energy for all carbenes tested in MeCN; **B:** Graph of pK_a vs. CO_2 binding energy for all carbenes tested in DMSO

In MeCN and DMSO, the same linear trend between CO_2 binding and pK_a, as seen in water, develops again. This trend does not appear as strong, and this should be read with caution for two reasons: 1. A smaller pool of carbenes was tested; 2. While pK_a calculations for water were calculated based on experimental data for carbenes in water, the lack of available data on carbenes in DMSO and MeCN meant that pK_a calculations for these solvents were done using a range of generic organic acids and bases. Nonetheless, the general trend can still be seen, and the expected results for each NHC family based on the nucleophilicity of the carbene carbon are indeed observed.

While CO_2 binding energies do not vary much between the two solvents, the graphs in **Figure 3.8** elucidate a lower pK_a of the carbenes tested in MeCN compared to DMSO and water. This can be accredited to the difference in proton solvation-free energies for the various solvents. The proton solvation-free energies for water, DMSO, and MeCN are -266.4, -266.5, and -255.1

kcal/mol.[19] Hence, in MeCN, where proton solvation energy is highest, the proton stays bound to the carbene, leading to the higher basicity exhibited by the carbenes in acetonitrile.

A similar trend to that seen in water regarding hydrogen bonding R-groups is displayed in DMSO and MeCN. The R-groups featuring hydrogen bond donors, including **D2**, **D3**, **O**, **P**, **Q**, and **T**, diverge below the trendline the most and have the lowest CO_2 binding energies relative to pK_a. They appear to diverge more in DMSO and MeCN than in water, suggesting a more pronounced hydrogen bonding, which is expected in a less polar environment (**Figures 3.7** *vs* **Figure 3.8**).[20] This is quantified in **Table 3.1**, where the strength of hydrogen bonds found between the bound CO_2 and R-groups by QTAIM analysis is calculated using the empirically derived formula presented by Emamian and coworkers.[21]

Table 3.1: Table of hydrogen bond strengths between CO_2 and R-groups in **(a) 1D2** and **(b) 1O.**

(a) Type **1D2**	
Solvent	**Hydrogen Bond Strength (kcal/mol)**
Water	*-70.196*
MeCN	*-73.096*
DMSO	*-70.620*
(b) Type **1O**	
Solvent	**Hydrogen Bond Strength (kcal/mol)**
Water	*-77.826*
MeCN	*-94.344*
DMSO	*-97.390*

3.2.3 Experimental Examination of NHCs in Non-Aqueous Solvents

To experimentally study CO_2 binding in NHCs, the isolation of the reactive carbene species first had to be obtained (**Scheme 3.1**). Experimental attempts to determine CO_2 binding were performed with **1C** (R = mesityl) in DMSO. Two methods were tested to assess CO_2 binding. The

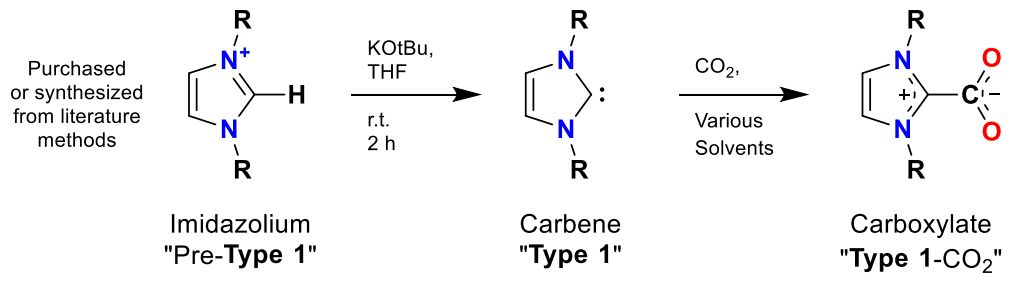

Scheme 3.1: Naming convention used and general synthesis between the imidazolium (pre-**Type 1**), NHC (**Type 1**), and imidazolium carboxylate (**Type 1**-CO_2). See section **3.4 Experimental** for details.

first method involved using a gas syringe to inject mole equivalents of gaseous CO_2 into a 10 mM solution of **1C** in deuterated DMSO to monitor CO_2 binding *via* ^{1}H NMR spectroscopy. Significant shifts in the ^{1}H NMR spectra were not observed until approximately 2 equivalents of CO_2 gas were added (**Figure 3.9**). The second method involved sparging the carbene solution with a gas mixture of CO_2 at different ratios with N_2 and various lengths of time and then monitoring the conversion of **1C** in MeCN and DMSO via ^{1}H NMR and UV-Vis spectroscopy (**Figures 3.10–3.13**). This

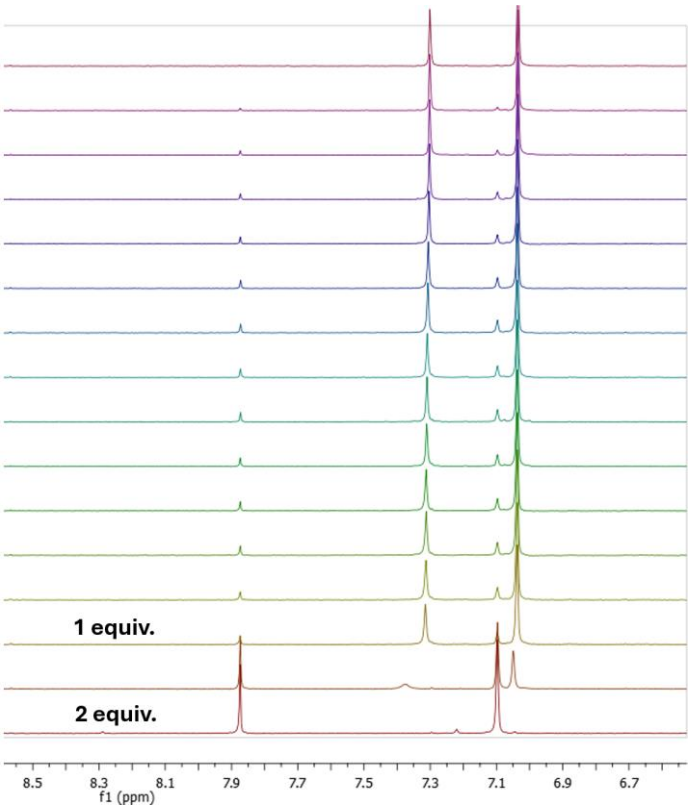

Figure 3.9: ^{1}H NMR spectra showing the progression of carboxylate formation after additions of CO_2 titrated into a NMR tube containing a 10 mM solution of **1C** in DMSO-d_6.

method determines the percentage of CO_2, which would not fully convert the carbene to carboxylate at the point of equilibrium. This observed gas ratio of CO_2 to N_2 could then be converted to a logK_{CO2}.

Lower concentrations of CO_2 in N_2 are slower to react with the carbene to form the carboxylate. Ratios of 1% CO_2 (observed with ^{1}H NMR, **Figures 3.10–3.11**) down to 0.01%

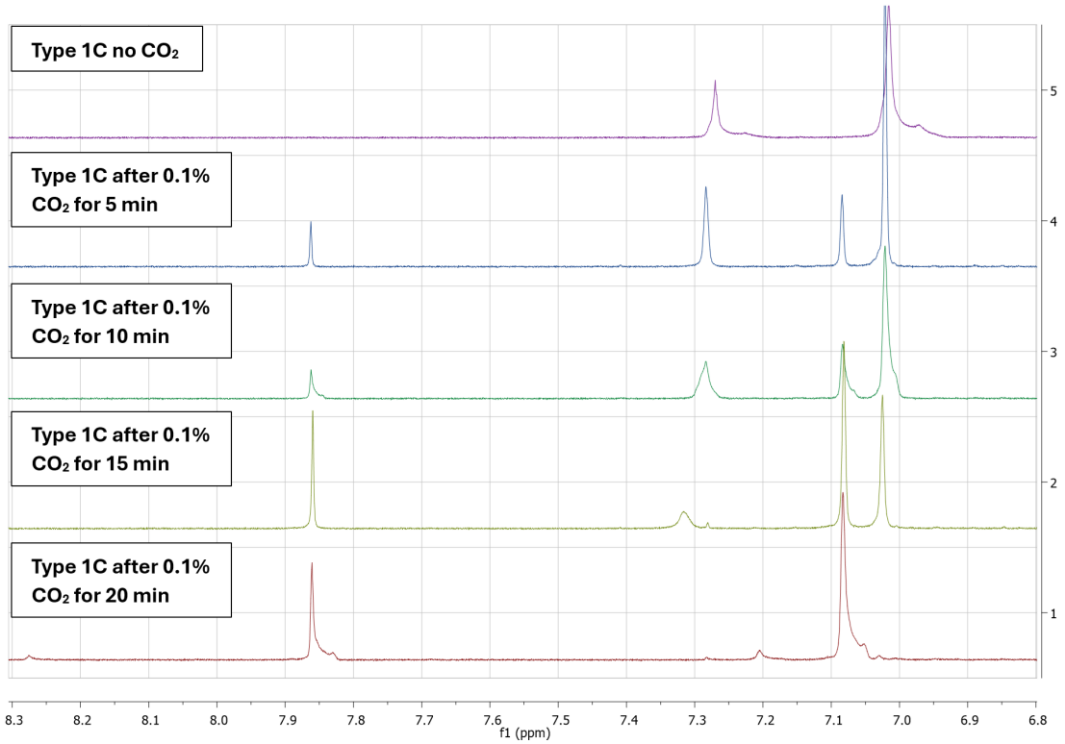

Figure 3.10: ^{1}H NMR spectra in DMSO-d_6 of 10 mM **1C**, taken at 5-minute intervals after sparging 0.1 % CO_2 in N_2 into the solution Complete conversion was observed after 20 minutes.

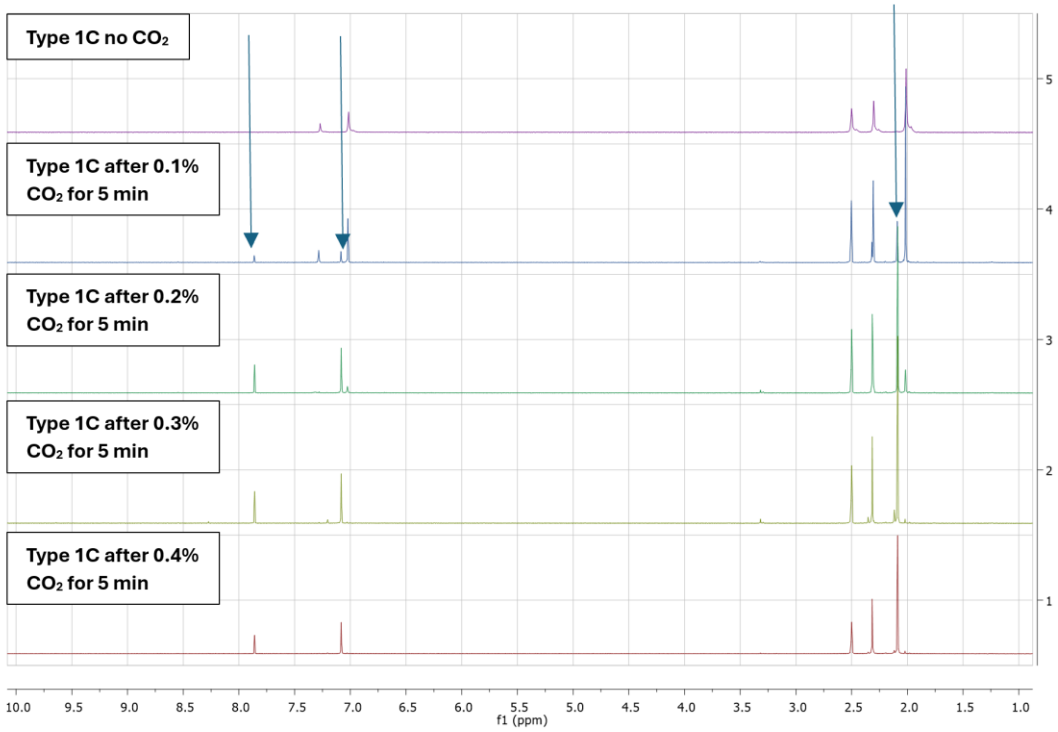

Figure 3.11: ^{1}H NMR spectra in DMSO-d_6 of 10 mM **1C** with increasing percentages of CO_2 after 5 minutes from addition. Arrows highlight the beginning of carboxylate formation.

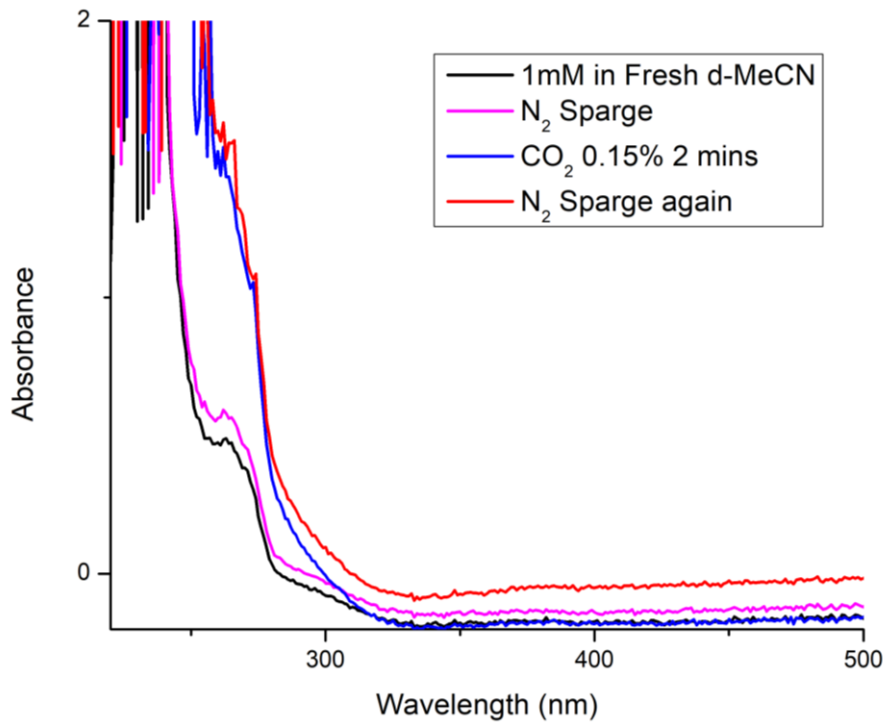

Figure 3.12: 1 mM of **1C** sparged with N_2, 0.15% CO_2 then N_2 again demonstrating irreversible binding of CO_2 in the observed increase absorbance of features between 230-280 nm.

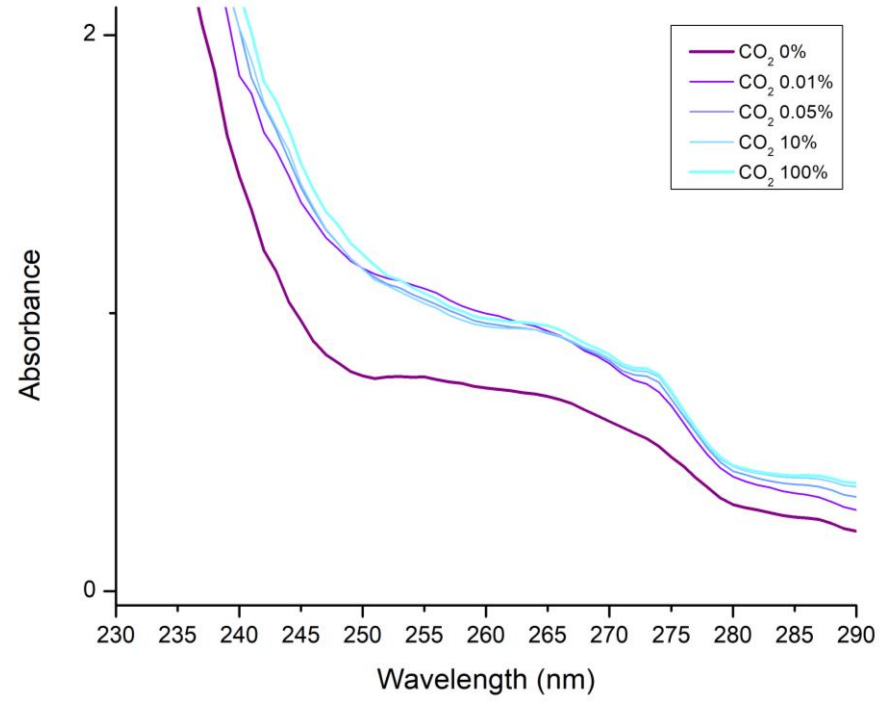

Figure 3.13: 1 mM solution of **1C** in the 250-280 nm region demonstrating that binding occurs at CO_2 concentrations as low as 0.01%.

(monitored by UV-Vis, **Figures 3.12–3.13**) could easily react to **1C** to form the carboxylate. This indicates ease in capturing CO_2 at DAC levels of 0.04% CO_2 and is in good agreement with the computation binding energy of -6.463 kcal/mol (DMSO) and -8.534 kcal/mol (MeCN). These values are compared to sources indicating that the minimum work energy to separate CO_2 *via* DAC methods is ΔG = 21 kJ/mol (5.0 kcal/mol), or the compound should have a logK_{CO2} above 5.0 (ΔG = -6.8 kcal/mol) in DMSO and 5.5 (ΔG = -7.5 kcal/mol) in MeCN.[15,22]

The corroboration of the experimental observation of CO_2 binding to the computational data was promising. However, the difficulties monitoring the experimental binding energies for these reactive molecules brought us to shift our sights toward isolating and characterizing a subset of NHC carboxylates. The characterization data obtained from these NHC carboxylates were compared with the computational data to identify potential patterns and relationships.

Synthetically accessible and commercially available NHCs, experimentally were converted to their carboxylate form and studied through ^{13}C NMR spectroscopy. A moderate correlation was found between the chemical shift of the carboxylate carbon (red carbon in **Figure 3.14**) and the calculated binding energy in DMSO-d_6 (**Figure 3.15, A**). A weaker correlation was also observed in MeCN (**Figure 3.15, B**), with the difference in trend attributed to a weaker solvent interaction of MeCN to the NHCs.[23,24]

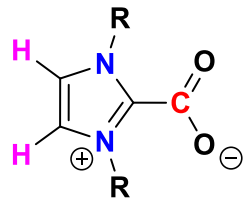

Figure 3.14: Sites of NMR data collection, the carboxylate carbon (red) and the imidazolium backbone protons (pink).

Interestingly, NHCs with electron-donating alkyl groups *t*-butyl (**J**) and adamantyl (**K**), which would typically be more shielded and upfield, were found to be the more deshielded NHC carboxylates of the ^{13}C NMR spectra for both solvents. There were difficulties in dissolving the carboxylated **1K** in sufficient quantities for ^{13}C NMR spectroscopy in CD_3CN. Still, it can be

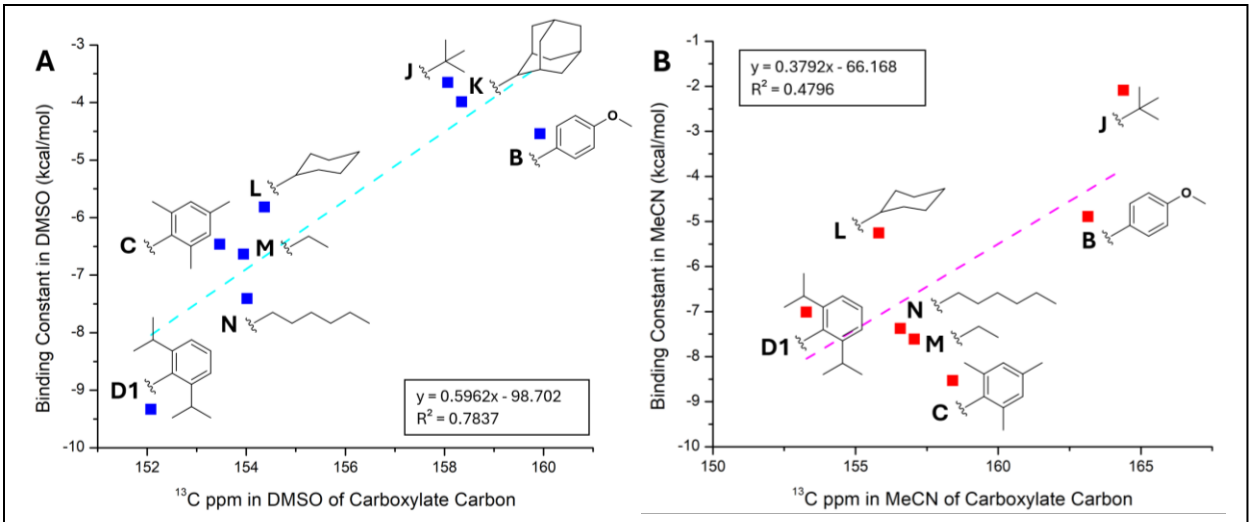

Figure 3.15: ^{13}C NMR chemical shift of the carboxylate carbon vs. CO_2 binding energies. **A:** DMSO; **B:** MeCN.

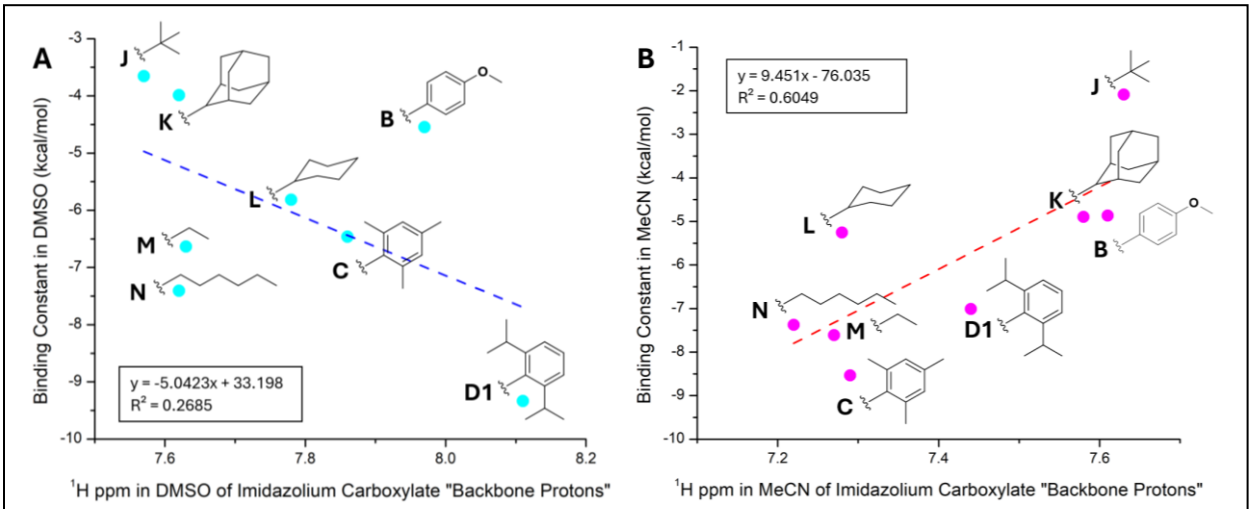

Figure 3.16: ^{1}H NMR chemical shift values of the imidazolium backbone protons vs. CO_2 binding energies. **A:** DMSO; **B:** MeCN.

interpolated that the compound would be downfield, close to **1J**, as seen in the ^{1}H NMR in CD_3CN (**Figure 3.16, B**) and ^{13}C NMR in DMSO-d_6 (**Figure 3.15, A**). As ^{13}C NMR chemical shifts tend to be less impacted by solvent effects and the electronic effects of the functional groups, this observation supports how the bulky and rigid geometry of the R-groups affect the more downfield shift of the carboxylate resonance. These would be the R-groups that contribute to rotating the torsion angle of the carboxylate closer to a perpendicular angle from the plane of the carbene. The carboxylate is pushed out of alignment from the rest of the molecule into a less favorable angle,

resulting in the pi orbitals ceasing to be conjugated with the electron-donating effects of the aromatic imidazolium body, thus more deshielded. Looking at the proton resonances on the imidazolium ring (pink hydrogens in **Figure 3.14**) of the carboxylates, the ^{1}H NMR spectra in DMSO-d_6 (**Figure 3.16, A**) display more of the typically expected trends. The **J** and **K** type (bulky alkyl) R-groups interact with DMSO in such a way that they appear upfield along with the other alkyl groups (**L**, **M**, **N**). This effect can be attributed to a stronger interaction of the solvent DMSO-d_6 to the solute, being the carboxylate species, and ^{1}H NMR spectra being more sensitive to solvent interaction compared to ^{13}C NMR. In comparison, acetonitrile has less solvent interaction with the solute, even in more sensitive ^{1}H NMR spectra.[23,24] Accordingly, the ^{1}H NMR spectra in CD_3CN show a modest trend more similar to what is observed in ^{13}C NMR spectra (**Figure 3.15 B** compared to **3.16 A** and **3.16 B**).

On the other hand, comparing the aromatic R-groups methoxyphenyl (**B**), mesityl (**C**), and diisopropylphenyl (**D1**) displays a pattern in the ^{13}C NMR spectra, where the bulkier aromatic groups (**C** and **D1**) tend toward being shifted more upfield and shielded (**Figures 3.15 A** and **3.15 B**). This trend may be seen as contradictory when considering general substituent bulkiness from the reported values for the percent buried volume ($\%V_{bur}$) in gold(I) NHC complexes. Nonaromatic bulky *t*-butyl groups (**J**) has a $\%V_{bur}$ of 39.6%, adamantyl (**K**) at 39.8%, compared to the mesityl groups (**C**) of 36.5% and diisopropylphenyl group (**D**) of 45.4%.[25,26] However, once it is considered how aryl groups can produce an electron-donating effect on the imidazolium body and, thus, on the carboxylate, effectively shielding the compound and pushing it more upfield, as seen with **1C** and **1D**. This effect leaves **1B**, which is not as bulky as either **1J** or **1K** (assuming it is less bulky than **1C**) and should be electron donating in nature by aryl groups with contributing

methoxy in the para position. However, the **1B** carboxylate carbon is downfield close in value to **1J** and **1K**, yet also on trend with its lower binding energy value.

It is important to consider that these reported $\%V_{bur}$ values describe the NHC ligand as it coordinates to a gold(I) metal center and are taken from the X-ray data of the corresponding crystal structures. Thus, there are limitations, especially considering how the NHC carboxylates will exist in different conformations when dissolved freely in solution.[25] Considering the anionic carboxylate group that has a preference to orient itself parallel to the imidazolium molecule, the variation in the steric bulkiness of R-groups (cyclohexyl **L**, %Vbur = 27.5 vs. adamantyl **K**, %Vbur = 39.8) would contribute to pushing it more perpendicular to the imidazolium and thus more downfield when observed by ^{13}C NMR spectra. Perhaps the variability of the bulkiness allowed by the rotation of the aryl groups can explain how diisopropylphenyl (**D1**) is the bulkiest when observed by $\%V_{bur}$ but more shielding in nature, as seen in NMR spectra and promotes a stronger CO_2 binding energy. Compounds **1C** and **1D1**, due to the steric bulk in the ortho positions, would rotate in such a manner about the imidazolium body that allows the carboxylate to still align itself more parallel to the imidazolium. In comparison, groups **J** and **K** are isotropically bulky. Finally, considering **1B**, with the less bulky para-methoxyphenyl groups, the molecule is possibly more inclined to orient the R-groups parallel to the imidazolium to maximize resonance with the aryl groups. In doing so, this would push the carboxylate more perpendicular, thus explaining the downfield shift observed in the ^{13}C NMR spectra. A summary of the variants of **Type 1** studied are listed in **Table 3.2**.

In synthesizing the NHCs through carboxylation for study, **1J** (R = *t*-butyl) proved to be one of the more challenging carbenes to react with CO_2. Residual moisture from the direct streams of CO_2 injected into the carbene samples was found to easily protonate **1J**, while all other NHCs

Table 3.2: Summary of Data for Type 1 compounds experimentally studied.

Type R =	DMSO Calc. p*K*co2	DMSO Calc. p*Ka*	DMSO-d6 C^{13} Carboxylate	DMSO-d6 ^{1}H Carboxylate	MeCN Calc. p*K*co2	MeCN Calc. p*Ka*	MeCN-d3 C^{13} Carboxylate	MeCN-*d3* ^{1}H Carboxylate	%Vbur ref (25,26)	Observed Binding CO_2 %
T1B = methoxy-phenyl	-4.546	18.816	160.42 ppm	7.97 ppm	-4.895	30.811	163.15 ppm	7.58 ppm		
T1C = mesityl	-6.463	20.519	152.89 ppm	7.86 ppm	-8.534	29.699	158.41 ppm	7.30 ppm	36.5%	0.01% (MeCN) 0.1% (DMSO
T1D = diisopropylphenyl	-9.335	18.606	152.57 ppm	8.11 ppm	-7.012	30.718	153.28 ppm	7.44 ppm	45.4%	
T1E = pentafluorophenyl	+0.131	7.055	*did not isolate*		+0.266	23.447	*did not isolate*			
T1J = tert-butyl	-3.655	23.361	158.56 ppm	7.57 ppm	-2.090	32.526	164.39 ppm	7.63 ppm	39.6%	
T1K = adamantyl	-3.989	22.886	158.84 ppm	7.62 ppm	-4.866	34.704	**N/A**	7.61 ppm	39.8%	
T1L = cyclohexyl	-5.818	20.969	154.86 ppm	7.78 ppm	-5.257	33.089	155.82 ppm	7.28 ppm	27.5%	
T1M = ethyl	-6.636	19.857	154.43 ppm	7.63 ppm	-7.613	32.303	157.06 ppm	7.27 ppm		
T1N = hexyl	-7.408	19.903	154.51 ppm	7.62 ppm	-7.376	32.281	156.57 ppm	7.22 ppm		
T1Q = propanol	-5.179	20.237	*did not isolate*		-6.572	31.779	*did not isolate*			

did not have this issue. Ultimately, successful carboxylation of **1J** was obtained by indirectly exposing a concentrated solution of **1J** in THF to a dilute headspace of CO_2, which was CO_2 gas sparged to the general glove box atmosphere, allowing drier conditions for **1J** carboxylate to precipitate out. It was also observed that **1J** decomposed to the protonated imidazolium over 2-3 days of storage in a N_2 atmosphere glove box. This sensitivity to protonation aligns with the above trend nature of group **J** with a weaker CO_2 binding energy but higher pK_a computed. All the other carboxylated NHCs, when stored in less rigidly dry conditions (ambient, out of the glove box), were also prone to convert to the protonated imidazolium as well.

Additional experiments were attempted on other functionalized NHCs. While obtaining analytically pure characterization data of the carboxylate form of these compounds was unsuccessful, they did provide enlightening observations. As the R-group **Q** (propanol) has been

observed computationally to contribute to off-trend behavior, the imidazolium precursor for **1Q** was a target that was successfully synthesized. However, direct deprotonation to the carbene proved difficult due to potential intramolecular protonation from the propanol groups. To bypass isolating the carbene intermediate, an attempt to carboxylate **1Q** by simultaneously exposing a solution of the imidazolium (pre-**1Q**) with a strong base in THF resulted in a striking color change observed, where the original brown-colored oil turned into a clear solution which, when washed and dried down, resulted in a clear, viscous gel-like substance which was no longer soluble in DMSO as pre-**1Q**. ^{1}H NMR spectra of the resulting product from CO_2 exposure showed the

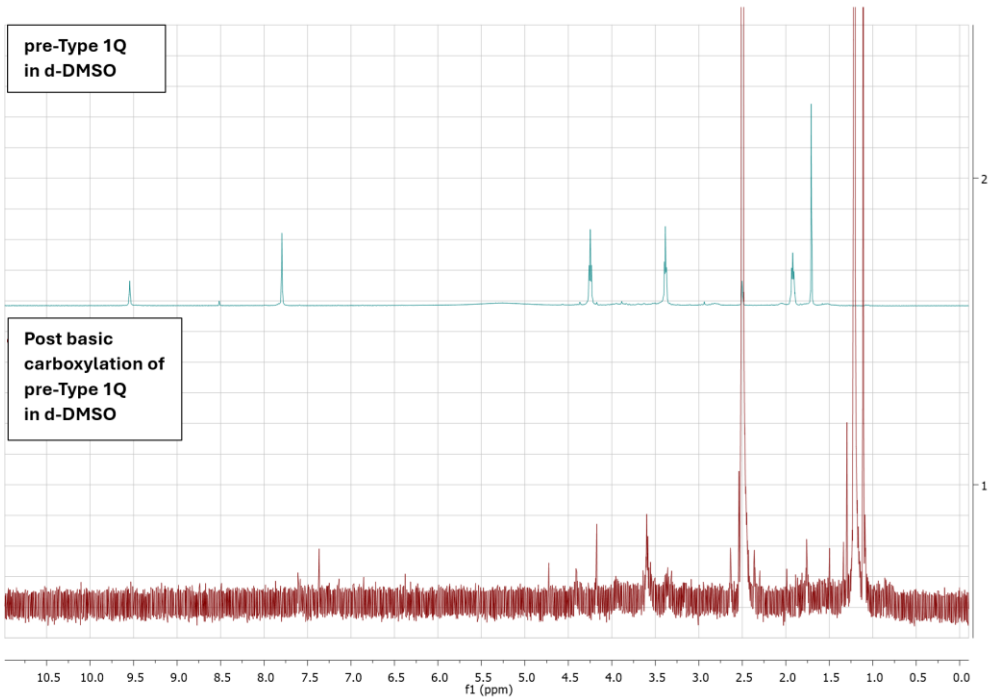

Figure 3.17: ^{1}H NMR spectra for **1Q** in DMSO-d_6; the synthesized pre-**1Q** (top) and the product post basic carboxylation (bottom).

disappearance of the imidazolium pre-**1Q** but no diagnostic peaks, indicating carboxylate production and with many resonances in the alkyl region (**Figure 3.17**).

There was interest in studying **1E**, an NHC on the weaker end in the range for CO_2 binding (0.131 kcal/mol in DMSO and -0.266 in MeCN). However, attempts to synthesize the imidazolium

(pre-**1E)** from the modified one-pot method for synthesizing pre-**1B** yielded 2,4,6,8-tetraazabicyclo-[3.3.0]octane (**Figure 3.18**). The synthetic route toward 2,4,6,8-tetraazabicyclo-[3.3.0]octane is similar to imidazolium, being a condensation from formaldehyde, glyoxal, and an amine.[27] However the electron withdrawing nature of the pentafluoroaniline may have directed the reaction to proceed to the 2,4,6,8-tetraazabicyclooctane rather than the desired imidazolium.[28] An ideal reaction pH has also been reported for the formation of the 2,4,6,8-tetraazabicyclooctane; given the more acidic nature of pentafluoroaniline compared to 4-methoxyaniline, the conditions of the reaction solution may be a factor.[27] This synthesis is the first reported for a pentafluoroaniline derivative 2,4,6,8-tetraazabicyclo-octane, with crystallography data confirming the structure now reported. While not a carbene, N-C-N systems, as seen in 2,4,6,8-tetraazabicyclooctanes are of interest for studying the anomeric effects, structure, reactivity, and conformation behaviors.[27,29–32]

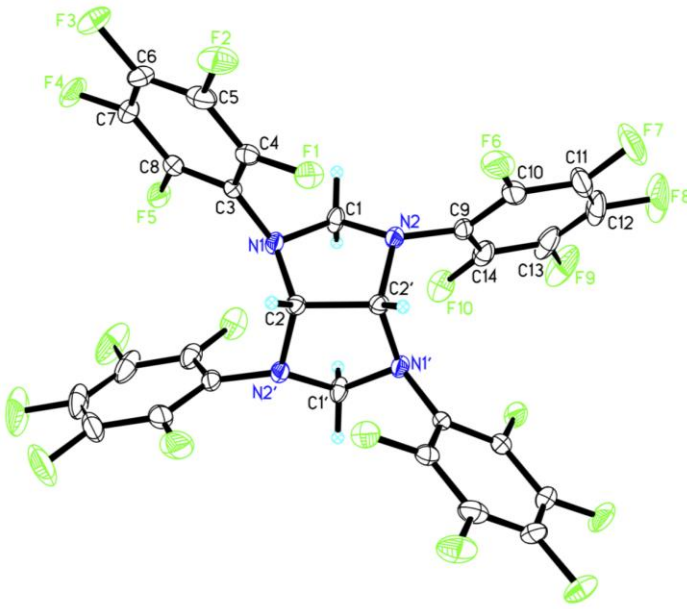

Figure 3.18: ORTEP structure of 2,4,6,8-tetrakis(pentafluorophenyl)-2,4,6,8-tetraazabicyclo-[3.3.0]octane, isolated *in lieu* of Type **1E**.

3.3 Conclusions

We have computed the CO_2 binding energies and pK_a values in H_2O, DMSO, and MeCN for a library of heterocyclic carbene molecules featuring R-groups of varied steric and electronic properties. All molecules were first calculated in water before the most basic ones were calculated

in organic solvents DMSO and MeCN. Experimental data was collected on select NHCs in DMSO and MeCN to corroborate the computational data.

Computational results found several 5-membered diamidocarbenes (5-DACs) were found to have sufficiently low pK_a values that would disfavor protonation in water and be able to participate in CO_2 binding. These include carbene featuring mainly aromatic R-groups with electron-withdrawing properties, as well as R-groups containing hydrogen bond donors (**Figure 4B**). The linear trend expected between pK_a and CO_2 binding affinity was generally seen in all carbene families in water. Carbenes featuring R-groups containing hydrogen bond donors, such as -OH and -NH_2, were found to deviate the most from this trend, appearing below the trendline indicating a stronger CO_2 affinity to pK_a. Bulky alkyl groups *t*-butyl (**J**) and adamantyl (**K**) were seen above the trendline demonstrating sensitivity to protonation over CO_2 affinity. A similar trend between pK_a and CO_2 binding affinity also seen for carbenes tested in DMSO and MeCN. The CO_2 binding energies were generally lower in these solvents due to the lack of stabilization of the zwitterionic product by the solvent. The order of carbene acidity in the solvents tested was generally seen to be $pK_{a,DMSO} > pK_{a,water} > pK_{a,MeCN}$, and this was attributed to the relative proton solvation energies in each solvent.

An observed trend between ^{1}H and ^{13}C NMR spectra of select carboxylated NHCs found that the characteristics of R-groups that contribute to the shifts upfield, more electron-donating, aligned with having a more negative binding energy for CO_2. Exceptions to the trend from bulky alkyl groups **J** and **K** seem to fall along the trend in how they affect the molecule's geometry and, thus, the weaker binding affinity to CO_2. The bulkiness of aryl groups, on the other hand, seemed to promote CO_2 binding. Additionally, the conversion to the carboxylate product was demonstrated with compound **1C** at low concentrations of CO_2 within the DAC capture range.

This research informs future investigations into the use of carbenes as direct CO_2 capture molecules. While carbenes may not be suitable for aqueous capture on a large scale, they may prove to be efficient capture molecules in other systems, such as ionic liquids.

3.4 Experimental

Computational Methods

Geometry optimization and frequency calculations were performed using Gaussian 16 software.[33] Density functional theory was used for all calculations, utilizing a B3LYP functional and def2TZVP basis set. Optimization calculations were performed with a D3 correction to better account for dispersion interactions. Frequency calculations were done to obtain frequency values for each optimized geometry and ensure no imaginary wavenumbers were present. The vast majority of molecules optimized to ground states; however, some retained small imaginary frequencies, < 20 cm^{-1}, despite being tried at several different geometries and using the VTight option for optimization. These molecules have been marked clearly in the supporting data and have not been considered during analysis. In this case, the implicit SMD model was used to account for the solvent, water.

The Gibbs free energy of CO_2 binding calculations was calculated using equation 1. Optimization and frequency calculations were simultaneously carried out using the SMD implicit solvent model. The sum of the electronic and thermal energies was obtained from the output file and used for the calculation.

The pK_a values were obtained using equations 2.1, 2.2, and 2.3. The first three terms of the Gibbs free energy equation (Eel + δGRRHO + δGsolv) were obtained from the sum of the electronic and thermal free energies in the output file of the opt freq calculations. The $\delta G1^{atm \rightarrow 1M}$ term is the

needed free energy to increase concentration from the gas phase to 1 M solution. This is a constant value set at 1.89 kcal mol^{-1}.

The Gibbs free energy of the NHC precursor and protonated NHC were calculated accordingly. The Gibbs free energy of a proton cannot be calculated through quantum mechanical methods, so it was calculated using thermodynamics and the Sackur Tetrode equation. Values of of $H^{o}_{(g)}[H^{+}]$ = 5/2RT kcal mol^{-1} and $S^{o}_{(g)}[H^{+}]$ = 26.5 cal mol^{-1} K^{-1} were obtained. The Gibbs free energy of deprotonation was then calculated. The pK_a values could then be calculated. Linear fitting based on experimental data was used to provide an equation that could be used to calculate theoretical pK_a values. For water, experimental data for NHCs was used.[34] For DMSO and MeCN, a lack of experimental data for carbenes in these solvents meant that pK_a data for generic organic acids had to be used instead.[35,36]

MultiWFN software was utilized for all molecular analysis, including QTAIM analysis, molecular orbital analysis, charge decomposition analysis, and Mayer bond order analysis.[37] Avogadro software was used to build all molecules in order to obtain Cartesian coordinates, view optimized structures, and check imaginary frequencies.[38]

Synthetic Methods

General Method: Synthetic work was carried out in either ambient air or under a dinitrogen (N_2) atmosphere in a glovebox where noted. All solvents and reagents were purchased from commercial vendors and used without further purification unless otherwise noted. Deuterated solvents used for NMR characterization were purchased from Cambridge Isotope Laboratories, Inc., and were degassed via free−pump−thaw and stored over activated 3 Å molecular sieves in an N_2 atmosphere glovebox. Tetrabutylammonium hexafluorophosphate ($TBAPF_6$) was purified via recrystallization

from ethanol, which was then dried under a heated (80 °C) vacuum (1×10^{-3} Torr) and stored in a glovebox. Experiments using carbon dioxide (CO_2) atmosphere were performed using ultrahigh purity (99.999%) CO_2, which was additionally passed through a purification column to eliminate residual H_2O, O_2, CO, halocarbons, and sulfur compounds.

1,3-bis(4-methoxyphenyl)imidazolium (**pre-Type 1B**) followed procedures by Wan et al.[39]

For **1,3-dicyclohexylimidazolium** (**pre-Type 1L**) and **1,3-diethylimidazolium** (**pre-Type 1M**), procedures by Barnett et al.[40]

For **1,3-dihexylimidazolium** (**pre-Type 1N**) and **1,3-di(3-hydroxypropyl)imidazolium** (**pre-Type 1Q**), modifications of procedures with imidazole and corresponding amines from Esposito et al.[41]

Other imidazolium (carbene precursors) were purchased from sellers and used without further purification which are: **1,3-bis(4-chlorophenyl)imidazolium** (**pre-Type 1A**), **1,3-di-tert-butylimidazolium** (**pre-Type 1J**) and **1,3-bis(1-adamantyl)imidazolium** (**pre-Type 1K**).

Deprotonation of the imidazolium precursor to the active carbene form was performed in a glove box under a dry nitrogen atmosphere. A standard procedure was used for the deprotonation step, closely following the method provided by Desens and Werner.[42]

General Deprotonation Method: Select imidazolium (2 mmol) was dissolved in THF (10 mL) and potassium or sodium *tert*-butoxide (2.25 mmol) was added to the solution. The reaction mixture was allowed to stir at room temperature for 2 hours before being dried down in vacuo.

The dry residue was extracted with hot toluene (2 × 3 mL, 60 °C) and filtered through Celite. The filtered product was isolated by removing toluene under reduced pressure.

In certain cases, the carbene commercially available and purchased directly and used without further purification. This included 1,3-bis(mesityl)imidazole-2-ylidene (**Type 1C**) and 1,3-bis(2,6-diisopropylphenyl)imidazole-2-ylidene (**Type 1D1**).

The carboxylation of the carbene to the carboxylate was similar among all the studied carbenes with the exception of **Type 1J**. The carboxylation method is described in the following.

General Carboxylation Method: In a N_2 glovebox environment, choice carbene is dissolved in THF and introduced to a stream of CO_2. The solution was sparged until precipitation had occurred and stopped. Unlike the rest of the carbenes, **Type 1J** (R = *t*-butyl) appeared sensitive to protonation and was more successful for carboxylation when an open vial of a solution of **Type 1J** in THF was exposed to the glove box atmosphere which had amounts of CO_2 in the air.

Physical Methods: CO_2 monitoring was performed on a CM-0111 gas sensor kit CM-0111 by CO2Meter with the software GasLab. ^{1}H and ^{13}C {1H} NMR and spectra were recorded at 500 MHz on Bruker and 600 MHz Varian instruments. ^{1}H NMR spectra chemical shifts were reported as δ values in ppm relative to residual protio solvent: D_2O (4.79 ppm), MeOD (3.31 ppm), CD_3CN (1.94 ppm) DMSO-d_6 (2.50 ppm). ^{13}C NMR spectra chemical shifts were reported as δ values in ppm relative to residual solvent: CD_3CN (118.26, 1.31 ppm) and DMSO-d_6 (39.52 ppm).

X-ray diffraction studies were conducted at the UCI Department of Chemistry X-ray Crystallography Facility on a Bruker SMART APEX II or Bruker X8 Prospector diffractometer.

Crystals were mounted in a cryoloop and transferred to a Bruker X8 Prospector (SMART APEX II) diffractometer system. The APEX3[43] (APEX2[44]) program package was used to determine the unit-cell parameters and for data collection (2 sec/frame scan time). The raw frame data was processed using SAINT[45] and SADABS[46] to yield the reflection data file. Subsequent calculations were carried out using the SHELXTL[47] program package. There were no systematic absences nor any diffraction symmetry other than the Friedel condition.

The structure was solved by direct methods and refined on F^2 by full-matrix least-squares techniques. The analytical scattering factors[48] for neutral atoms were used throughout the analysis. Hydrogen atoms were located from a difference-Fourier map and refined (x,y,z and U_{iso}). The molecule was located about an inversion center.

Characterization Data for Imidazoliums:

1,3-bis(4-methoxyphenyl)imidazolium (pre-**Type 1B**): ^{1}H NMR (498 MHz, **$CDCl_3$**) δ 10.14 (s, 1H), 8.45 (s, 2H), 7.82 (d, *J* = 7.8 Hz, 4H), 7.23 (d, *J* = 7.9 Hz, 4H), 3.86 (s, 6H).

1,3-dicyclohexylimidazolium (**pre-Type 1L**): ^{1}H NMR (498 MHz, **DMSO**) δ 9.42 (s, 1H), 7.93 (s, 2H), 4.28 (s, 2H), 2.07 (d, *J* = 10.6 Hz, 4H), 1.84 (d, *J* = 12.4 Hz, 4H), 1.68 (s, 6H), 1.38 (d, *J* = 12.2 Hz, 4H), 1.20 (d, *J* = 13.0 Hz, 2H).

1,3-diethylimidazolium (**pre-Type 1M**): ^{1}H NMR (498 MHz, **DMSO**) δ 9.33 (s, 1H), 7.84 (s, 2H), 4.20 (d, *J* = 7.3 Hz, 4H), 1.42 (s, 6H).

1,3-dihexylimidazolium (**pre-Type 1N**): ^{1}H NMR (600 MHz, **CD_3CN**) δ 8.49 (s, 1H), 7.38 (d, *J* = 1.5 Hz, 2H), 4.11 (s, 4H), 1.82 (s, 4H), 1.29 (d, *J* = 15.8 Hz, 12H), 0.89 (s, 6H).

1,3-di(3-hydroxypropyl)imidazolium [$CH_3COO]^-$ (**pre-Type 1Q**): ^{1}H NMR (498 MHz, **D_2O**) δ 8.85 (s, 1H), 7.54 (s, 2H), 4.32 (t, 4H), 3.64 (t, 4H), 2.12 (p, 4H), ^{1}H NMR (498 MHz, **DMSO**) δ 9.54 (s, 1H), 7.79 (s, 2H), 5.33 (br, 2H), 4.25 (t, *J* = 6.7 Hz, 4H), 1.99 – 1.87 (m, 4H), 1.71 (d, *J* = 0.9 Hz, 4H).

Characterization Data for Ylidenes:

1,3-bis(4-methoxyphenyl)imidazole-2-ylidene (**Type 1B**): ^{1}H NMR (600 MHz, **DMSO**) δ 7.89 (s, 2H), 7.79 (d, J = 9.1 Hz, 4H), 7.04 (d, J = 8.8 Hz, 4H), 3.80 (s, 6H).

1,3-di-tert-butylimidazole-2-ylidene (**Type 1J**): ^{1}H NMR (498 MHz, **DMSO**) δ 7.24 (s, 2H), 1.49 (s, 18H).

1,3-bis(1-adamantyl)imidazole-2-ylidene (**Type 1K**): ^{1}H NMR (498 MHz, **DMSO**) δ 7.19 (s, 2H), 2.12 (s, 6H), 2.05 (s, 12H), 1.69 (s, 12H).

1,3-dicyclohexylimidazole-2-ylidene (**Type 1L**): ^{1}H NMR (498 MHz, **DMSO**) δ 7.09 (d, *J* = 37.7 Hz, 2H), 3.93 (t, *J* = 11.7 Hz, 2H), 1.88 (d, *J* = 11.4 Hz, 4H), 1.78 (d, *J* = 13.1 Hz, 4H), 1.69 – 1.57 (m, 6H), 1.35 (q, *J* = 12.8 Hz, 4H), 1.18 (dd, *J* = 25.6, 12.9 Hz, 2H).

1,3-diethylimidazole-2-ylidene (**Type 1M**): ^{1}H NMR (498 MHz, **DMSO**) δ 7.06 (s, 2H), 3.91 (q, *J* = 7.3 Hz, 4H), 1.29 (t, *J* = 7.3 Hz, 6H).

1,3-dihexylimidazole-2-ylidene (**Type 1N**): ^{1}H NMR (498 MHz, DMSO) δ 7.11 (s, 2H), 3.90 (t, *J* = 7.1 Hz, 4H), 1.73 – 1.62 (m, 4H), 1.24 (s, 12H), 0.85 (d, *J* = 6.3 Hz, 6H).

Characterization Data for Imidazolium Carboxylates:

1,3-bis(4-methoxyphenyl)imidazolium-carboxylate (**Type 1B-CO_2**): ^{1}H NMR (600 MHz, **DMSO**) δ 7.97 (s, 2H), 7.63 (d, *J* = 9.0 Hz, 2H), 7.13 (d, *J* = 9.0 Hz, 4H), 3.85 (d, *J* = 22.0 Hz, 6H), ^{1}H NMR (600 MHz, **CD_3CN**) δ 7.58 (s, 2H), 7.09 (s, 2H), 6.91 (ddd, *J* = 91.8, 58.1, 21.9 Hz, 4H), 3.86 (s, 6H), ^{13}C NMR (151 MHz, **DMSO**) δ 159.93 (s), 128.38 (s), 125.79 (s), 120.93 (s), 114.67 (s), 55.66 (s), ^{13}C NMR (151 MHz, **CD_3CN**) δ 163.15 (s), 159.59 (s), 126.94 (s), 122.83 (s), 115.44 (s), 66.22 (s).

1,3-bis(mesityl)imidazolium-carboxylate (**Type 1C-CO_2**): ^{1}H NMR (499 MHz, **DMSO**) δ 7.86 (s, 2H), 7.08 (s, 4H), 2.32 (s, 4H), 2.09 (s, 18H), ^{1}H NMR (600 MHz, **CD_3CN**) δ 7.32 (s, 2H), 7.08 (s, 4H), 2.35 (s, 4H), 2.14 (s, 18H). ^{13}C NMR (151 MHz, **DMSO**) δ 152.98 (s), 146.39 (s) 139.58 (s), 134.69 (s), 131.91 (s), 128.81 (s), 121.68 (s), 16.87 (s), ^{13}C NMR (151 MHz, **CD_3CN**) δ 158.41 (s), 144.83 (s), 141.33 (s), 136.95 (s), 122.35 (s), 21.11 (s), 17.57 (s).

1,3-bis(2,6-diisopropylphenyl)imidazolium-carboxylate (**Type 1D-CO_2**): ^{1}H NMR (600 MHz, **CD_3CN**) δ 7.53 (t, *J* = 7.8 Hz, 2H), 7.44 (s, 2H), 7.37 (d, *J* = 7.7 Hz, 4H), 2.60 – 2.49 (m, 4H), 1.23 (dd, *J* = 27.9, 6.9 Hz, 24H),^{13}C NMR (151 MHz, **DMSO**) δ 152.08 (s), 147.00 (s), 144.84 (s), 131.95 (s), 130.47 (s), 123.87 (s), 123.21 (s), 28.62 (s), 24.11 (s), 22.92 (s), ^{13}C NMR (151 MHz, **CD_3CN**) δ 153.28 (s), 148.37 (s), 146.21 (s), 131.59 (s), 125.00 (s), 123.82 (s), 29.88 (s), 24.39 (s), 23.51 (s).

1,3-di-tert-butylimidazolium-carboxylate (**Type 1J-CO_2**): ^{1}H NMR (600 MHz, **DMSO**) δ 7.57 (s, 2H), 1.63 (s, 18H), ^{1}H NMR (600 MHz, **CD_3CN**) δ 7.63 (s, 2H), 1.63 (s, 18H), ^{13}C NMR (151 MHz, **DMSO**) δ 158.07 (s), 145.71 (s), 116.61 (s), 60.93 (s), 29.07 (s), ^{13}C NMR (151 MHz, **CD_3CN**) δ 164.39 (s), 120.87 (d, *J* = 20.0 Hz), 60.96 (d, *J* = 1.9 Hz), 29.70 (s).

1,3-bis(1-adamantyl)imidazolium-carboxylate (**Type 1K-CO_2**): ^{1}H NMR (600 MHz, **DMSO**) δ 7.64 (s, 2H), 2.29 (d, *J* = 2.6 Hz, 12H), 2.14 (s, 6H), 1.65 (s, 12H), ^{1}H NMR (600 MHz, **CD_3CN**) δ 7.61 (s, 2H), 2.26 (s, 6H), 2.16 (d, *J* = 2.6 Hz, 12H), 1.78 (dd, *J* = 26.4, 12.5 Hz, 12H), ^{13}C NMR (151 MHz, **DMSO**) δ 158.35 (s), 145.52 (s), 115.85 (s), 61.78 (s), 34.99 (s), 29.25 (s).

1,3-dicyclohexylimidazolium-carboxylate (**Type 1L-CO_2**): ^{1}H NMR (498 MHz, **DMSO**) δ 7.78 (s, 2H), 4.84 (s, 2H), 1.92 (d, *J* = 10.8 Hz, 4H), 1.82 (d, *J* = 12.9 Hz, 4H), 1.72 – 1.58 (m, 6H), 1.34 (q, *J* = 12.8 Hz, 4H), 1.25 – 1.13 (m, 2H), ^{1}H NMR (600 MHz, **CD_3CN**) δ 7.28 (s, 2H), 5.01 (tt, *J* = 12.0, 3.7 Hz, 2H), 2.04 (d, *J* = 11.1 Hz, 4H), 1.86 (d, *J* = 13.9 Hz, 4H), 1.74 – 1.60 (m, 6H), 1.48 – 1.38 (m, 4H), 1.29 – 1.19 (m, 2H), ^{13}C NMR (151 MHz, **DMSO**) δ 154.37 (s), 142.95 (s), 117.63 (s), 57.19 (s), 32.37 (s), 24.93 (s), 24.43 (s), ^{13}C NMR (151 MHz, **CD_3CN**) δ 155.82 (s), 144.62 (s), 58.82 (s), 33.85 (s), 26.06 (s), 25.63 (s).

1,3-diethylimidazolium-carboxylate (**Type 1M-CO_2**): ^{1}H NMR (498 MHz, **DMSO**) δ 7.63 (s, 2H), 4.43 (q, *J* = 7.3 Hz, 4H), 1.34 (t, *J* = 7.2 Hz, 6H), ^{1}H NMR (600 MHz, **CD_3CN**) δ 7.27 (s, 2H), 4.49 (d, *J* = 7.2 Hz, 4H), 1.39 (s, 6H), ^{13}C NMR (151 MHz, **DMSO**) δ 153.95 (s), 141.77 (s), 124.20 (s), 122.11 (s), 120.59 (s), 66.92 (s), 64.91 (s), 43.93 (s), 31.30 (s), 15.84 (s), ^{13}C NMR (151 MHz, **CD_3CN**) δ 157.06 (s) 141.83 (s), 121.79 (s), 45.82 (s), 16.19 (s).

1,3-dihexylimidazolium-carboxylate (**Type 1N-CO_2**): ^{1}H NMR (600 MHz, **DMSO**) δ 7.62 (s, 2H), 4.41 (t, *J* = 7.3 Hz, 4H), 1.76 – 1.66 (m, 4H), 1.23 (dq, *J* = 13.1, 8.6 Hz, 12H), 0.83 (s, 6H), ^{1}H NMR (600 MHz, **CD_3CN**) δ 7.22 (s, 2H), 4.46 (t, *J* = 7.3 Hz, 4H), 1.81 – 1.72 (m, 4H), 1.28 (s, 12H), 0.87 (t, *J* = 5.4 Hz, 6H), ^{13}C NMR (151 MHz, **DMSO**) δ 154.02 (s), 142.23 (s), 120.94 (s), 48.45 (s), 30.61 (s), 29.95 (s), 25.28 (s), 21.89 (s), 13.79 (s), ^{13}C NMR (151 MHz, **CD_3CN**) δ 156.57 (s), 142.81 (s), 123.36 (s), 121.94 (s), 50.53 (s), 50.30 (s), 31.88 (s), 31.68 (s), 31.19 (s), 30.39 (s), 26.57 (s), 26.30 (s), 23.08 (d, *J* = 10.1 Hz), 14.16 (d, *J* = 6.6 Hz).

Characterization for Other Molecules:

2,4,6,8-tetrakis(pentafluorophenyl)-2,4,6,8-tetraazabicyclo-[3.3.0]octane: ^{1}H NMR (600 MHz, **DMSO**) δ 6.05 (s, 2H), 5.17 (s, 2H), 4.63 (s, 2H), ^{19}F NMR (565 MHz, **DMSO**) δ -148.97 (d, F8), -161.65 (t, J = 23.1 Hz, F4), -163.58 (t, J = 22.1 Hz, F4).

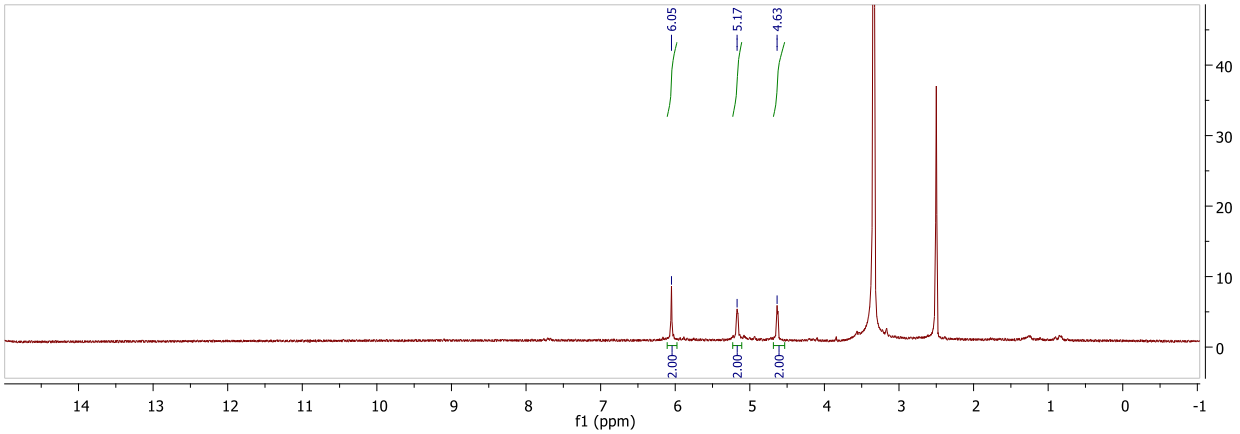

Figure 3.19: ^{1}H NMR of **2,4,6,8-tetrakis(pentafluorophenyl)-2,4,6,8-tetraazabicyclo-[3.3.0]octane** in DMSO-d_6, 600 MHz, 293 K.

3.5 References

(1) Dutcher, B.; Fan, M.; Russell, A. G. Amine-Based CO_2 Capture Technology Development from the Beginning of 2013—A Review. *ACS Appl. Mater. Interfaces* **2015**, *7* (4), 2137–2148. https://doi.org/10.1021/am507465f.

(2) Yang, X.; Rees, R. J.; Conway, W.; Puxty, G.; Yang, Q.; Winkler, D. A. Computational Modeling and Simulation of CO_2 Capture by Aqueous Amines. *Chem. Rev.* **2017**, *117* (14), 9524–9593. https://doi.org/10.1021/acs.chemrev.6b00662.

(3) Zhang, Z.; Kummeth, A. L.; Yang, J. Y.; Alexandrova, A. N. Inverse Molecular Design of Alkoxides and Phenoxides for Aqueous Direct Air Capture of CO_2. *Proc. Natl. Acad. Sci.* **2022**, *119* (25), e2123496119. https://doi.org/10.1073/pnas.2123496119.

(4) Del Bene, J. E.; Alkorta, I.; Elguero, J. Carbon–Carbon Bonding between Nitrogen Heterocyclic Carbenes and CO_2. *J. Phys. Chem. A* **2017**, *121* (42), 8136–8146. https://doi.org/10.1021/acs.jpca.7b08393.

(5) Yang, L.; Wang, H. Recent Advances in Carbon Dioxide Capture, Fixation, and Activation by Using N-Heterocyclic Carbenes. *ChemSusChem* **2014**, *7* (4), 962–998. https://doi.org/10.1002/cssc.201301131.

(6) Stiernet, P.; Pang, B.; Taton, D.; Yuan, J. The Promise of *N*-Heterocyclic Carbenes to Capture and Valorize Carbon Dioxide. *Sustain. Chem. Clim. Action* **2023**, *2*, 100018. https://doi.org/10.1016/j.scca.2023.100018.

(7) Wang, Z.; Xue, X.-S.; Fu, Y.; Ji, P. Comprehensive Basicity Scales for N-Heterocyclic Carbenes in DMSO: Implications on the Stabilities of N-Heterocyclic Carbene and CO2 Adducts. *Chem. – Asian J.* **2020**, *15* (1), 169–181. https://doi.org/10.1002/asia.201901418.

(8) Thomas, M.; Brehm, M.; Hollóczki, O.; Kirchner, B. How Can a Carbene Be Active in an Ionic Liquid? *Chem. – Eur. J.* **2014**, *20* (6), 1622–1629. https://doi.org/10.1002/chem.201303329.

(9) Faisal Elmobarak, W.; Almomani, F.; Tawalbeh, M.; Al-Othman, A.; Martis, R.; Rasool, K. Current Status of CO_2 Capture with Ionic Liquids: Development and Progress. *Fuel* **2023**, *344*, 128102. https://doi.org/10.1016/j.fuel.2023.128102.

(10) Seo, S.; DeSilva, M. A.; Brennecke, J. F. Physical Properties and CO_2 Reaction Pathway of 1-Ethyl-3-Methylimidazolium Ionic Liquids with Aprotic Heterocyclic Anions. *J. Phys. Chem. B* **2014**, *118* (51), 14870–14879. https://doi.org/10.1021/jp509583c.

(11) Xiao, M.; Liu, H.; Gao, H.; Olson, W.; Liang, Z. CO_2 Capture with Hybrid Absorbents of Low Viscosity Imidazolium-Based Ionic Liquids and Amine. *Appl. Energy* **2019**, *235*, 311–319. https://doi.org/10.1016/j.apenergy.2018.10.103.

(12) Feroci, M.; Chiarotto, I.; Forte, G.; Vecchio Ciprioti, S.; Inesi, A. Stability and CO_2 Capture Ability of Electrogenerated N-Heterocyclic Carbene in Parent 1-Butyl-3-Methylimidazoliun Ionic Liquid (BMIm-X): The Role of X−. *ChemElectroChem* **2014**, *1* (8), 1407–1414. https://doi.org/10.1002/celc.201300269.

(13) Gomes, R. J.; Birch, C.; Cencer, M. M.; Li, C.; Son, S.-B.; Bloom, I. D.; Assary, R. S.; Amanchukwu, C. V. Probing Electrolyte Influence on CO_2 Reduction in Aprotic Solvents. *J. Phys. Chem. C* **2022**, *126* (32), 13595–13606. https://doi.org/10.1021/acs.jpcc.2c03321.

(14) Liu, F.; Shen, Y.; Shen, L.; Sun, C.; Chen, L.; Wang, Q.; Li, S.; Li, W. Novel Amino-Functionalized Ionic Liquid/Organic Solvent with Low Viscosity for CO_2 Capture. *Environ. Sci. Technol.* **2020**, *54* (6), 3520–3529. https://doi.org/10.1021/acs.est.9b06717.

(15) Barlow, J. M.; Yang, J. Y. Oxygen-Stable Electrochemical CO_2 Capture and Concentration with Quinones Using Alcohol Additives. *J. Am. Chem. Soc.* **2022**, *144* (31), 14161–14169. https://doi.org/10.1021/jacs.2c04044.

(16) Denning, D. M.; Falvey, D. E. *Substituent and Solvent Effects on the Stability of N-Heterocyclic Carbene Complexes with CO_2*. ACS Publications. https://doi.org/10.1021/acs.joc.6b02755.

(17) Moerdyk, J. P.; Schilter, D.; Bielawski, C. W. N,N′-Diamidocarbenes: Isolable Divalent Carbons with Bona Fide Carbene Reactivity. *Acc. Chem. Res.* **2016**, *49* (8), 1458–1468. https://doi.org/10.1021/acs.accounts.6b00080.

(18) Hudnall, T. W.; Bielawski, C. W. An N,N′-Diamidocarbene: Studies in C−H Insertion, Reversible Carbonylation, and Transition-Metal Coordination Chemistry. *J. Am. Chem. Soc.* **2009**, *131* (44), 16039–16041. https://doi.org/10.1021/ja907481w.

(19) Rossini, E.; Knapp, E.-W. Proton Solvation in Protic and Aprotic Solvents. *J. Comput. Chem.* **2016**, *37* (12), 1082–1091. https://doi.org/10.1002/jcc.24297.

(20) Meredith, N. Y.; Borsley, S.; Smolyar, I. V.; Nichol, G. S.; Baker, C. M.; Ling, K. B.; Cockroft, S. L. Dissecting Solvent Effects on Hydrogen Bonding. *Angew. Chem. Int. Ed.* **2022**, *61* (30), e202206604. https://doi.org/10.1002/anie.202206604.

(21) Emamian, S.; Lu, T.; Kruse, H.; Emamian, H. Exploring Nature and Predicting Strength of Hydrogen Bonds: A Correlation Analysis Between Atoms-in-Molecules Descriptors, Binding Energies, and Energy Components of Symmetry-Adapted Perturbation Theory. *J. Comput. Chem.* **2019**, *40* (32), 2868–2881. https://doi.org/10.1002/jcc.26068.

(22) *Direct Air Capture of CO_2 with Chemicals*. https://www.aps.org/publications/reports/direct-air-capture-co2 (accessed 2024-08-24).

(23) Gottlieb, H. E.; Graczyk-Millbrandt, G.; Inglis, G. G. A.; Nudelman, A.; Perez, D.; Qian, Y.; Shuster, L. E.; Sneddon, H. F.; Upton, R. J. Development of GSK's NMR Guides – a Tool to Encourage the Use of More Sustainable Solvents. *Green Chem.* **2016**, *18* (13), 3867–3878. https://doi.org/10.1039/C6GC00446F.

(24) Ai, W.-T.; Su, W.-K.; Su, F. Solvents Influence ^{1}H NMR Chemical Shifts and Complete ^{1}H and ^{13}C NMR Spectral Assignments for Florfenicol. *Pharm. Fronts* **2023**, *05*, e288–e296. https://doi.org/10.1055/s-0043-1777285.

(25) Gómez-Suárez, A.; Nelson, D. J.; Nolan, S. P. Quantifying and Understanding the Steric Properties of N-Heterocyclic Carbenes. *Chem. Commun.* **2017**, *53* (18), 2650–2660. https://doi.org/10.1039/C7CC00255F.

(26) Hopkinson, M. N.; Glorius, F. An Overview of NHCs. In *N-Heterocyclic Carbenes in Organocatalysis*; John Wiley & Sons, Ltd, 2018; pp 1–35. https://doi.org/10.1002/9783527809042.ch1.

(27) Kakanejadifard, A.; Farnia, S. M. F. Synthesis and X-Ray Structural Determination of New Aniline Derivatives of 2,4,6,8-Tetraazabicyclo[3.3.0]Octanes; Anomeric Effect in N-C-N Moiety

and Implications of Solvent Polarity on 1H-NMR Patterns. *Tetrahedron* **1997**, *53* (7), 2551–2556. https://doi.org/10.1016/S0040-4020(96)01143-X.

(28) Ghandi, M.; Salimi, F.; Olyaei, A. Novel Reaction of N,N'-Bisarylmethanediamines with Formaldehyde. Synthesis of Some New 1,3,5-Triaryl-1,3,5-Hexahydrotriazines. *Molecules* **2006**, *11* (7), 556–563. https://doi.org/10.3390/11070556.

(29) Senderowitz, H.; Aped, P.; Fuchs, B. Computation of N-C-N Systems: Theory vs. Experiment. *Tetrahedron* **1992**, *48* (6), 1131–1144. https://doi.org/10.1016/S0040-4020(01)88209-0.

(30) Aped, P.; Schleifer, L.; Fuchs, B.; Wolfe, S. Probing the Anomeric Effect. The Diaminomethylene Group: Calculations of N–C–N-Containing Molecular Systems1. *J. Comput. Chem.* **1989**, *10* (2), 265–283. https://doi.org/10.1002/jcc.540100210.

(31) Rivera, A.; Sadat-Bernal, J.; Ríos-Motta, J.; Dušek, M.; Palatinus, L. Synthesis and Structural Studies of a New Class of Quaternary Ammonium Salts, Which Are Derivatives of Cage Adamanzane Type Aminal 1, 3, 6, 8-Tetraazatricyclo[4.3.1.13,8]Undecane (TATU). *Chem. Cent. J.* **2011**, *5* (1), 55. https://doi.org/10.1186/1752-153X-5-55.

(32) Singh, A.; Ganguly, B. Probing the Influence of Solvent Effects on the Conformational Behavior of 1,3-Diazacyclohexane Systems. *J. Phys. Chem. A* **2007**, *111* (39), 9884–9889. https://doi.org/10.1021/jp074146x.

(33) Frisch, M. J.; Trucks, G. W.; Schlegel, H. B.; Scuseria, G. E.; Robb, M. A.; Cheeseman, J. R.; Scalmani, G.; Barone, V.; Petersson, G. A.; Nakatsuji, H.; Li, X.; Caricato, M.; Marenich, A. V.; Bloino, J.; Janesko, B. G.; Gomperts, R.; Mennucci, B.; Hratchian, H. P.; Ortiz, J. V.; Izmaylov, A. F.; Sonnenberg, J. L.; Williams-Young, D.; Ding, F.; Lipparini, F.; Egidi, F.; Goings, J.; Peng,

B.; Petrone, A.; Henderson, T.; Ranasinghe, D.; Zakrzewki, V. G.; Gao, J.; Rega, N.; Zheng, G.; Liang, W.; Hada, M.; Ehara, M.; Toyota, K.; Fukuda, R.; Hasegawa, J.; Ishida, M.; Nakajima, T.; Honda, Y.; Kitao, O.; Nakai, H.; Vreven, T.; Throssell, K.; Montgomery, J. A. Jr.; Peralta, J. E.; Ogliaro, F.; Bearpark, M. J.; Heyd, J. J.; Brothers, E. N.; Kudin, K. N.; Staroverov, V.; Keith, T. A.; Kobayashi, R.; Normand, J.; Raghavachari, K.; Rendell, A. P.; Burant, J. C.; Iyengar, S. S.; Tomasi, J.; Cossi, M.; Millam, J. M.; Klene, M.; Adamo, C.; Cammi, R.; Ochterski, J. W.; Martin, R. L.; Morokuma, K.; Farkas, O.; Foresman, J. B.; Fox, D. J. Gaussian 16, Revision C.01, 2016. https://gaussian.com/citation/ (accessed 2024-08-20).

(34) Higgins, E. M.; Sherwood, J. A.; Lindsay, A. G.; Armstrong, J.; Massey, R. S.; Alder, R. W.; O'Donoghue, A. C. pKas of the Conjugate Acids of N-Heterocyclic Carbenes in Water. *Chem. Commun.* **2011**, *47* (5), 1559–1561. https://doi.org/10.1039/C0CC03367G.

(35) Kütt, A.; Tshepelevitsh, S.; Saame, J.; Lõkov, M.; Kaljurand, I.; Selberg, S.; Leito, I. Strengths of Acids in Acetonitrile. *Eur. J. Org. Chem.* **2021**, *2021* (9), 1407–1419. https://doi.org/10.1002/ejoc.202001649.

(36) Reich, H.; Bordwell. pKa Values in DMSO Compilation. https://organicchemistrydata.org/hansreich/resources/pka/pka_data/pka-compilation-reich-bordwell.pdf.

(37) Lu, T.; Chen, F. Multiwfn: A Multifunctional Wavefunction Analyzer. *J. Comput. Chem.* **2012**, *33* (5), 580–592. https://doi.org/10.1002/jcc.22885.

(38) Hanwell, M. D.; Curtis, D. E.; Lonie, D. C.; Vandermeersch, T.; Zurek, E.; Hutchison, G. R. Avogadro: An Advanced Semantic Chemical Editor, Visualization, and Analysis Platform. *J. Cheminformatics* **2012**, *4* (1), 17. https://doi.org/10.1186/1758-2946-4-17.

(39) Wan, Y.; Zhang, W.-L.; Cui, H.; Zhang, L.-Z.; Zhou, Q.-J.; Zou, H.; Wang, Y.-J.; Ge, W.-H.; Fang, Y.; Zhou, S.-L.; Wu, H. Silica Sulfuric Acid-Catalyzed One-Pot Synthesis of 1,3-Diarylimidazolium Tetrafluoroborate. *Asian J. Chem.* **2015**, *27* (8), 3107–3110. https://doi.org/10.14233/ajchem.2015.18954.

(40) Barnett, C.; Cole, M. L.; Harper, J. B. Steric Properties of N-Heterocyclic Carbenes Affect the Performance of Electronic Probes. *Eur. J. Inorg. Chem.* **2021**, *2021* (47), 4954–4958. https://doi.org/10.1002/ejic.202100796.

(41) Esposito, D.; Kirchhecker, S.; Antonietti, M. A Sustainable Route towards Imidazolium Building Blocks Based on Biomass Molecules. *Chem. – Eur. J.* **2013**, *19* (45), 15097–15100. https://doi.org/10.1002/chem.201302806.

(42) Desens, W.; Werner, T. Convergent Activation Concept for CO_2 Fixation in Carbonates. *Adv. Synth. Catal.* **2016**, *358* (4), 622–630. https://doi.org/10.1002/adsc.201500941.

(43) APEX2 Version 2014.11-0, Bruker AXS, Inc.; Madison, WI **2014**.

(44) APEX3 Version 2018.1-0, Bruker AXS, Inc.; Madison, WI **2018**.

(45) SAINT Version 8.34a, Bruker AXS, Inc.; Madison, WI **2013**.

(46) Sheldrick, G. M. SADABS, Version 2014/5, Bruker AXS, Inc.; Madison, WI **2014**.

(47) Sheldrick, G. M. SHELXTL, Version 2014/7, Bruker AXS, Inc.; Madison, WI **2014**

(48) International Tables for Crystallography 1992, Vol. C., Dordrecht: Kluwer Academic Publishers.